UNIVERSITY OF SOUTHAMPTON

FACULTY OF NATURAL AND ENVIRONMENTAL SCIENCES

School of Ocean and Earth Science

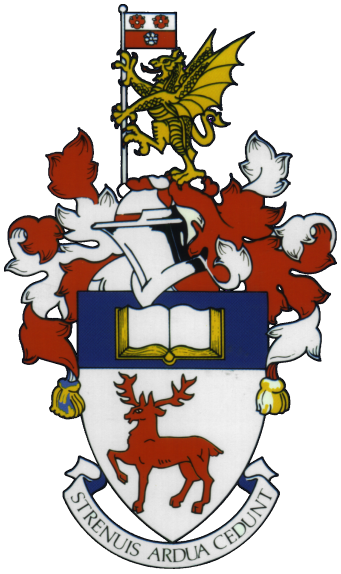

UNDERSTANDING THE DYNAMICS OF SUBMARINE DENSITY FLOWS THROUGH DIRECT OBSERVATIONS FROM MODERN SYSTEMS

by

Maria Azpiroz

Thesis for the degree of Doctor of Philosophy

June 2018

UNIVERSITY OF SOUTHAMPTON

ABSTRACT

FACULTY OF NATURAL AND ENVIRONMENTAL SCIENCES

School of Ocean and Earth Science

Thesis for the degree of Doctor of Philosophy

UNDERSTANDING THE DYNAMICS OF SUBMARINE DENSITY FLOWS THROUGH DIRECT OBSERVATIONS FROM MODERN SYSTEMS

Maria Azpiroz

Submarine density flows are the volumetrically most important process for transporting sediment across our planet and form the largest sediment accumulations on Earth. Current models for turbidity currents are largely based on experimental and numerical models, and inferences from deposits in the geological record. This thesis provides a new understanding of the structure of submarine density flows through the analysis of direct measurements of submarine density currents near the seafloor. This is achieved by the analysis of datasets of density flows collected in two submarine channel systems: Congo Submarine Canyon and a channel on the Black Sea Shelf. The analysis of new measurements of submarine density flows suggests a new structure for submarine density flows that contrasts with previous models. The new structure shows that the flow front is the fastest part of the flow that outruns the rest of the flow. The difference in velocities between the front and end of the flow results in a flow stretching. This model contrasts with previous field observations of submarine flows collected in coarser sediment submarine channel systems. This thesis also analyses the cross-stream evolution of submarine density flows through meandering submarine channel systems. This new model studies the

evolution of the flow processes around meanders, and suggests different scenarios of the flow structure based on the dominant process. This document links the evolving structure of the flow around bends with the sediment distribution of the submarine channel systems, and reconciles discrepancies among earlier models. This thesis provides a better understanding of the complexity of the system formed by submarine density flows and the interaction of these flows with seafloor sediment and channel morphology.

Table of Contents

Table of Tables

Table of Figures

Academic Thesis: Declaration Of Authorship

I, Maria Azpiroz declare that this thesis entitled '**Understanding the dynamics of submarine density flows through direct observations from modern systems**' and the work presented in it are my own, and has been generated by me as the result of my own original research.

I confirm that:

1. This work was done wholly or mainly while in candidature for a research degree at this University;
2. Where any part of this thesis has previously been submitted for a degree or any other qualification at this University or any other institution, this has been clearly stated;
3. Where I have consulted the published work of others, this is always clearly attributed;
4. Where I have quoted from the work of others, the source is always given. With the exception of such quotations, this thesis is entirely my own work;
5. I have acknowledged all main sources of help;
6. Where the thesis is based on work done by myself jointly with others, I have made clear exactly what was done by others and what I have contributed myself;
7. Parts of this work have been published as:

   Azpiroz-Zabala, M., Cartigny, M.J.B., Talling, P.J., Parsons, D.R., Sumner, E.J., Clare, M.A., Simmons, S.M., Cooper, C. and Pope, E.L. (2017). Newly recognized turbidity current structure can explain prolonged flushing of submarine canyons. Sci. Adv. 3, e1700200 (2017).

   Azpiroz-Zabala, M., Cartigny, M. J. B., Sumner, E. J., Clare, M. A., Talling, P. J., Parsons, D. R., & Cooper, C. (2017). A general model for the helical structure of geophysical flows in channel bends. Geophysical Research Letters, 44, 11,932–11,941. https://doi.org/10.1002/2017GL075721.

Signed: .....

Date: .....

Acknowledgements

Probably this is the most difficult section of my thesis…. So many people to name, so many moments to recall, so many … Here I go!

First of all I would like to thank my supervisors Esther Sumner, Matthieu Cartigny, Pete Talling and Mike Clare for their infinite patience, support, encouragement, guidance both in professional and personal respects. Esther has been simply great. Great as scientist and as human: always present and listening, available to discuss, inspiring, concise and direct going far far far beyond the original plan. Matthieu has been brilliant. I have loved our scientific discussions, his ultra quick mind always switching on lights when my mind felt obscured, his smart views and challenging ideas. Pete has been more than generous, offering me the opportunity of developing this thesis in the first place, of gaining training for my professional career, of carrying out incredibly inspiring field work and of giving feedback on manuscripts in the shortest times ever. And Mike has been more than a colleague, a clear mind with a smile on his face always, with real focus, and the right words at the right moment. And for all of you, thanks for learning my Spanglish so quickly! I would like also to thank Mark Vardy for being a fantastic panel chair, closely following my scientific career and offering me endless support and advice, also NERC and GSNOCS for funding this studentship and for the opportunity to study here. Thanks also to all co-authors for all the stimulating discussions and sharing of knowledge. Also, I would like to thank Charlie Thompson and Jaco Baas for examining my thesis and providing helpful comments in a great discussion to improve this work.

I would like to thank my NOC sedimentology group mates Age, Alessandro, Daniela, Ed, James, Jamie, Jenny, Josh, Lewis, Maarten, Millie, Sophie, Will, Zoe for our great science discussion during our informal meetings (at NOC or over a beer). Thanks to my office mates, to my corridor (or should I call it plate at NOC?) mates, canteen mates, house mates… Thanks to everyone who spent 5 minutes (or 5 months!) speaking, laughing, eating, drinking, dancing with me. Spending that time with all of you is exactly what I needed to be where I am now!

And finally thanks to all my families, although thanks is a word that cannot express what I feel. Thanks to those who believed in me, those who did not, those who supported me, those who comforted me, those who made me laugh, who made me love, who made me sing and made me cry. Thanks to those I found

on the way and to those who left on the way. Thanks to all of you. Could I name all of you? Here? Resulta dificil escribir todos vuestros nombres aqui. Imposible. Se tambien que no hace falta que lo haga, vosotros sabeis quienes sois.

Chapter 1:

Introduction

1.1 Rationale

The aim of this work is to better understand the dynamic interaction between density flows and the seafloor based on direct observations in modern submarine channel systems.

Submarine density flows are flows driven downslope by their density excess in relation to the ambient water. This study focuses on two types of submarine density flows: (1) turbidity currents, which are submarine density flows where the excess in density is caused by suspended sediment; and (2) saline flows, which are submarine density flows where the excess in density is caused by a higher salinity. Submarine density flows, in particular turbidity currents, have formed the largest sediment accumulations on Earth, termed submarine fans (Normark, 1970; Savoye et al., 2009; Shepard, 1933). Only river systems carry similar volumes of sediment, although a single submarine density flow can sometimes transport more sediment than the annual global flux from all rivers combined (Milliman and Syvitski, 1992; Talling et al., 2007).

Submarine channel systems serve as conduits for submarine density flows moving from shallow waters towards the deep-sea. Most of the longest submarine channel systems worldwide have a meandering planform (Normark and Carlson, 2003) that suggests that bends may enhance distances over which sediment is transported (Pirmez and Imran, 2003; Straub et al., 2008). Meanders might influence the submarine density flow structure and, consequently, the sediment transport capability of these flows. Understanding the dynamics of submarine density flows, particularly as they travel around bends, is key to evaluating the sediment transport and deposition, which ultimately determines the evolution of

channel systems.

Submarine density flows are difficult to monitor directly. They occur in relatively inaccessible locations, their occurrence is often unpredictable, and they frequently damage measuring instruments placed in their path due to their energy (Inman et al., 1976; Sumner et Paull, 2014). This paucity of direct observations has meant that previous models for submarine density flows were based mainly on results of laboratory-scale experiments (Baas et al., 2005; Kneller et al., 1999; Kuenen, 1937, Middleton, 1966), numerical modeling (Cantero et al., 2012; Meiburg and Kneller, 2010; Parker et al., 1986), measurements of rivers (Kuenen, 1952; Parker, 1982; Parker et al., 1986), or inferences made from their deposits (Bouma, 1962; Kuenen and Migliorini, 1950; Sumner et al., 2012). The conclusions from these studies do not always agree with one another, or with the rare observations of natural submarine density flows. There are apparent similarities between rivers and meandering submarine channels (Shepard, 1933; Talling et al., 2007). However, the flows within these two systems, rivers and submarine density flows, differ in several ways. The density difference between the flow and the ambient fluid in which they occur is different: rivers occur in air, and river water is thousands of times denser than air; whereas, submarine density flows occur in seawater, and the density of both submarine density flow and ambient seawater have the same order of magnitude. This difference leads to different density and velocity profiles of both fluvial and oceanic flows that affect flow behaviour (Stacey and Bowen, 1988). The contrast between direct observations, experimental studies and numerical models of submarine density flows could result from scaling issues (Peakall et al., 1996) and simplifying assumptions (Meiburg and Kneller, 2010). The study of submarine density flows from their deposits can only provide hypotheses (Sumner et al., 2012). To make a step change in understanding of submarine density flows, there is a need to measure key parameters within full-scale events (Talling et al., 2015). Advances in acoustic technology and in mooring design are now enabling direct observations of those flows in their submarine environment.

These observations of natural submarine density flows are enabling reconciliation of discrepancies among previous models. Additionally, the observations can quantify the amounts of sediment, organic carbon, nutrients, and fresh-water flushed into the deep ocean. A better understanding of the flow dynamics will eventually pave the way to predicting the evolution of submarine channels on long time-scales.

1.1.1 Aim of the thesis

The overall aim of this thesis is to understand the dynamics of submarine density currents through the analysis of field measurements collected in the last decade. The datasets that I used to achieve this aim constitute the most extensive and highest-resolution acoustic measurements of submarine density currents ever obtained worldwide. In particular, I analysed three datasets for this thesis: (1) a 4-month long dataset collected in 2010 by an Acoustic Doppler Current profiler (ADCP) in the Congo Canyon; (2) a 2-month long dataset collected in 2013 by two ADCPs deployed ~22 km apart in the Congo Canyon; and (3) an acoustic dataset collected in 2013 by an ADCP installed on an Autonomous Underwater Vehicle (AUV) in combination with a large dataset of conductivity, depth and temperature (CTD) measurements at the entrance to the Black Sea.

The velocity, density and sediment concentration results extracted from these datasets address the following specific research questions:

1. Can the sediment type within submarine sediment density flows control the duration of the flows?
2. How do density stratification and flow acceleration processes combine to influence suspend sediment transport in the meanders of long submarine canyon systems?
3. How accurately do different analysis frames of reference of the flow structure of submarine density flows reflect the sediment distribution observed in meandering submarine channel systems?

1.1.2 Structure of the thesis

This section details the rationale of each chapter and how they link together.

The core of this thesis is presented as three science chapters that have been produced independently as scientific journal papers. All chapters concern an enhanced understanding of the dynamics of submarine density flows and share common aspects of the methodology, which forms chapter 2. However, because this is a thesis by publication, each chapter can be read independently. Chapter 3

is based on two datasets using ADCP records of submarine sediment-laden density flows collected in the Congo Canyon. Chapter 4 studies further one of these two datasets. Chapter 5 analyses the third dataset of a saline submarine flow collected by an ADCP and CTDs on the Black Sea shelf, downstream from the Bosphorus Strait. Chapters 3 and 4 have been published in Science Advances and Geophysical Research Letters respectively; Chapter 5 is to be submitted to Journal of Geophysical Research.

This introductory chapter provides a brief overview of concepts discussed in greater detail within the science chapters (Chapters 3, 4, and 5).

In chapter 3, the analysis of the highest-resolution datasets yet from a submarine sediment-laden density flow ever collected in the field results in a novel flow model. The datasets were collected in 2010 and 2013 in the Congo Canyon at approximately 150 km from the head of the canyon, which is connected to the Congo River. The turbidity current measurements show flows that, in contrast to all previous direct observations and most model predictions, last for days rather than hours or minutes. The turbidity currents in this chapter stretch over time, which results in an increasing flow duration, due to the difference in velocity between the fast front and the slow tail of the flow. The front of the flow hosts the fastest and densest part of the flow, and confines the highest turbulence to the near-bed region. The fast and dense front triggers high bed shear stress that mobilises seafloor sediment. This seafloor sediment gets entrained into the flow and moves towards the slower body and then tail of the flow, where the velocity eventually decays and the sediment settles out. Thus, the flow front becomes the driver of the flow that allows self-sustainability of the flow. This contrasts with previous models in which the fastest and more erosive part of the flow is located in the body, which would then be the driver of the flow. In the latter model, the body would feed the slower moving head with sediment and this would not be self-sustaining, and would result in flow extinction within minutes or hours. The conclusions of this chapter suggest that the turbidity currents in the Congo Canyon are typical of mud-rich systems. In contrast, turbidity currents in coarser systems, such as Monterey Canyon, Var Canyon and Gaoping Canyon, might behave similarly to previous direct observations in other systems (Khripounoff et al., 2009; Liu et al., 2012; Xu et al., 2004). This work also concludes that the frequent and week-long turbidity currents in the Congo Canyon can flush important amounts of sediment, organic carbon, nutrients, and fresh water into the deep ocean.

In chapter 4, the 2010 Congo Canyon dataset previously analysed in chapter 3 is further studied. The aim of the chapter is understanding the connection between meander bends in submarine channel systems and the suspension of sediment in flows. Previous work concerning the structure of submarine flows in meanders agrees that flows display a helical-shaped flow in bends. However, previous work has made contradictory conclusions in terms of the direction of the circulation of the basal flow, and whether it is alike or opposite to rivers. The work in this chapter concludes that the direction of the helical flow in meanders is controlled mainly by two pressure gradients. The centrifugal acceleration that flows experience in the bend generates the first pressure gradient. This pressure gradient generates a basal flow circulation towards the inner bend. Thus, the densest basal part of the flow is pushed towards the inner bend where it develops the second lateral pressure gradient due to the density stratification. This second pressure gradient has a basal opposite direction to the centrifugally-driven pressure gradient. The ratio between both pressure gradients defines the direction of the basal flow that can be either river-like or river-reversed. This work emphasises the importance of the evolution of the lateral density stratification around meanders. This chapter reconciles previous work conclusions and determines that the submarine channel evolution depends on the curvature of the channel and the stratification of the flow around the bends.

In chapter 5, an extensive dataset collected from a channel on the Black Sea shelf is studied. The measurements comprise density and velocity records of a saline submarine flow in several transects around a bend, thus enabling the study of the spatial evolution of the helical flow around a bend. Most of previous works on helical submarine flows have been based on 2-dimensional (2D) studies due to the difficulties in obtaining 3-dimensional (3D) datasets. The analysis of this 3D dataset demonstrates that the characteristics of the 2D view of a 3D flow depends strongly on the 2D frame of reference, and that results from different 2D frames of references can appear opposite to one another. This explains previous discrepancies in results from field, experimental and numerical modelling studies. Finally the chapter shows how the 3D helical structure forms a key control on the distribution of the sediment around the channel bend, which links the flow behaviour and local bathymetry to the evolution of the channel bend.

Chapter 6 summarises the conclusions of this thesis revisiting the research questions in the previous section. It also includes potential future steps towards a

further understanding of the dynamics of submarine density flows.

1.2 Classification of submarine density flows

This section presents a classification of the different types of submarine density flows that exist in nature, and expands into turbidity currents and saline flows, which are the submarine density flows on which this thesis focuses.

Submarine density flows are currents driven by the difference in density between the flow (caused by sediment in suspension, temperature, salinity) and the ambient seawater in which they occur. The ratio between the flow and the ambient densities defines four general behaviours for submarine density flows (Figure 1.1): (1) **vertical flows** occur when fluids denser than the seawater enter vertically and progress vertically towards the seafloor; (2) **overflows** develop when fluids that are less dense than seawater flow along the seawater-air boundary; (3) **interflows** form when fluids progress along the density interface between two seawater layers with lower and higher densities respectively than the progressing interflows; and (4) **underflows** occur when fluids denser than seawater flow along the seafloor.

This thesis is focused on submarine underflows and among them, on turbidity currents and saline flows. Turbidity currents are stratified underflows with higher densities towards the bottom of the flow, even when they are relatively 'well-mixed' (Talling et al., 2012). Saline flows exist as well-mixed flows and stratified flows (Nidzieko et al., 2009), and are found in flooding estuaries (Nidzieko et al., 2009) or in narrow straits that connect basins with different salinities (Umlauf and Arneborg, 2009).

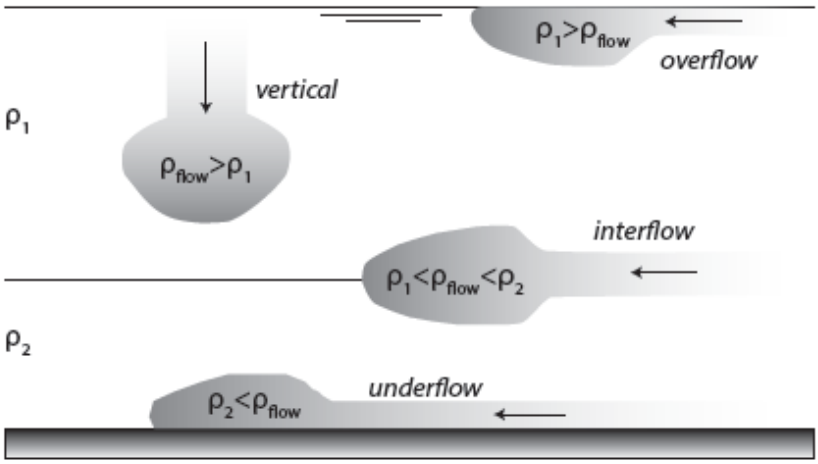

Figure 1.1. Scenarios of density flows resultant from the ratio between densities of flow and ambient seawater (modified from Allen (1985)).

1.3 Submarine channel systems

All of the submarine density flows, discussed in this thesis occur within submarine channels. This overview introduces submarine channel systems as part of a combined system with submarine density flows, in which both evolve and impose distinctive attributes to each other.

The morphology of submarine channel systems changes from steep, V-shaped cross-channel sections, which are typically located proximal to the shelf, to U-shaped cross-channel sections, which are typically located distally to the shelf. This change in the morphology of submarine channel systems coincides with changes in the energy of submarine density flows and their capability to erode or transport sediment. Thus, submarine density flows usually show their higher energy at proximal sections, where the flow capacity of erosion is higher as the V-shape cross-section of the submarine system manifests. Deposition starts to dominate over erosion at more distal sections of the submarine channel systems, and U-shape cross-channel sections develop. Submarine density flows show their lowest energy at the most distal sections of submarine channel systems, where the flow is depositional and forms submarine fans.

The steep to shallow evolution of submarine channel systems and erosional to depositional evolution of submarine density flows occur worldwide (Figure 1.2). This thesis analyses two submarine channel systems: (1) Congo Canyon, located in the upper erosional part of the Congo submarine channel system, and (2) Black Sea channel, located in the depositional Black Sea shelf.

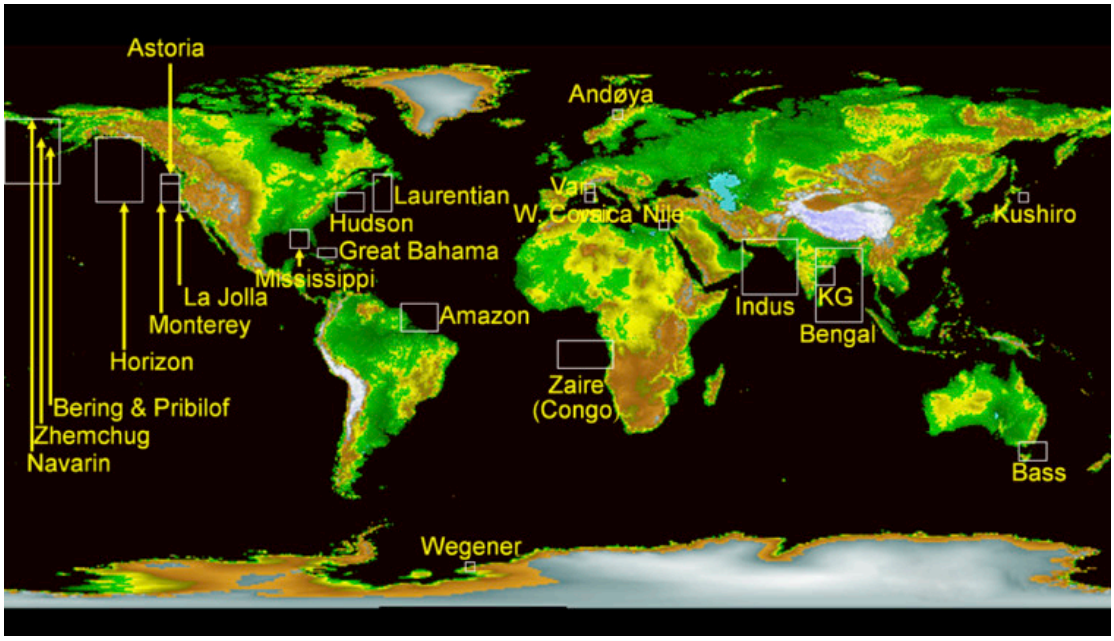

Figure 1.2. Distribution of the largest submarine channel systems on Earth (modified from Normark and Carlson, 2003).

1.4 Anatomy of submarine density currents

The aim of the section is to provide an overview of the classical anatomy of submarine density flows (Meiburg and Kneller, 2010; Middleton, 1993; Simpson, 1997), and to introduce the three main flow parts based on the velocity and erosive capacity of each part. This classical model is challenged by the conclusions presented in chapter 3, where a new model of the anatomy of turbidity current is proposed.

A classical model of submarine density flows, mostly based on experimental and numerical models, consist of three sections, termed the head, body and tail. These sections are characterized by distinctive flow behaviours.

The head occurs at the front of the flow. The front of the head is often slower than the following flow. It is slowed down by the simultaneous friction (1) between the flow and the ambient seawater at the top of the flow, and with the seafloor at the bottom of the flow; and (2) between the flow and the ambient seawater in front of the flow, which is pushed out of the way by the submarine density flow to enable the flow passage (Cartigny et al., 2013; Kneller and Buckee, 2000; McCaffrey et al., 2003). The head of the flow is followed by the body, which is more stable than the head. The body tends to flow faster than the

head front because it only experiences the friction by both ambient seawater and seafloor (Cartigny et al., 2013; Kneller and Buckee, 2000; McCaffrey et al., 2003). Finally, the body is followed by the flow tail where flow velocities decay rapidly and the flow dissipates (Kneller and Buckee, 2000). Importantly, in this model, the part of the body just behind the head is the section of the flow that is fastest; it feeds and accelerates the flow through erosion (Cartigny et al., 2013; McCaffrey et al., 2003). Thus, the classical model of the internal relative circulation within a submarine density flow is characterised by a circulation from the part of the flow just behind the head towards the flow front, and from there towards the back of the body and tail.

Chapter 2:

Methodology

2.1 Acoustic Doppler Current Profilers (ADCP): Successful monitoring of submarine density flows in recent years

Advances in technology and mooring configuration have begun to enable successful direct monitoring of sediment density currents on the seafloor. Acoustic Doppler Current Profilers (ADCPs) have recently achieved a high number of successful measurements of submarine density flows. ADCPs can be deployed in a mooring line (chapters 3 and 4) for long deployments (Cooper et al., 2013; 2016; Khripounoff et al., 2003), mounted on ship hulls (Parsons et al., 2007), or AUVs (chapter 5; Sumner et al., 2013).

ADCPs infer velocity measurements from acoustic frequency variations. This inference, called Doppler shift, arises from acoustic waves reflected by scatterers in the way of the acoustic waves (Oberg and Mueller, 2007; Teledyne, 2011). The ADCP emits acoustic waves along at least 3 paths (or beams) at a fixed frequency and then receives the reflected acoustic response from fluid parcels (or bins) along the beams (Figure 2.1). They compute the averaged velocity of the fluid at each bin through the comparison between the emitted and received wave frequency (Teledyne, 2011). The instrument expresses the averaged velocity in three components (V_{North}, V_{East} and $V_{Vertical}$), which depending of the configuration of the instrument relate to geographical orientation (if the ADCP is moored) or ADCP orientation (if the ADCP is mounted on hull or AUV). This thesis is based on datasets collected by different instruments, and their configuration is described in following sections of this chapter.

ADCPs also measure the strength of the acoustic waves (or echo intensity), which can be inverted to provide an estimation of sediment concentration as detailed in

section 2.5 of this chapter (Thorne and Hanes, 2002; Thorne and Hurther, 2014). Thus, ADCPs provide direct or indirect measurements of two key parameters in the study of the dynamics of submarine density flows: (1) velocity (Parsons et al., 2007; Sumner et al., 2013); and (2) sediment concentration (Thorne and Hanes, 2002; Thorne and Hurther, 2014).

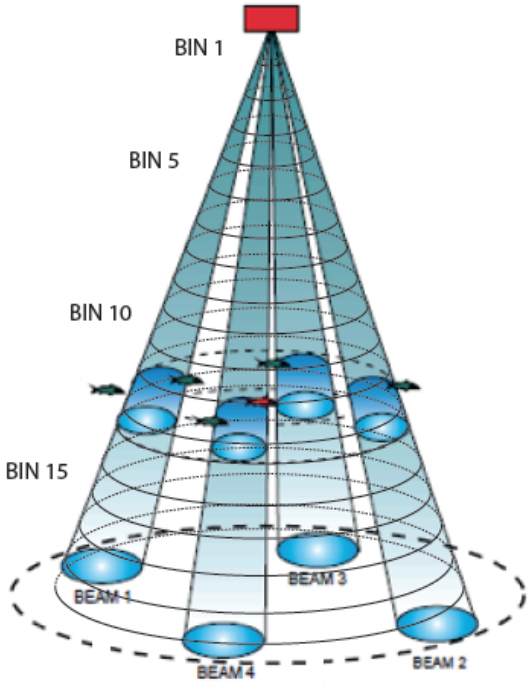

Figure 2.1. Sketch of operation of an ADCP (modified from Teledyne 2010).

Previous studies on turbidity currents have used ADCP measurements to analyse the turbidity current structure. ADCPs have been deployed in natural environments to study the flow velocity records inferred by these acoustic instruments (Corney et al., 2006; Sumner et al., 2014; Xu et al., 2013). ADCP echo intensity measurements have been also inverted to obtain estimates of scatter concentration in natural environments (Lavery and Ross, 2007) and conceptual studies to achieve sediment concentrations from acoustic measurements have been of scientific interest in recent years (Thorne and Hanes, 2002; Thorne and Hurther, 2014). However, ADCPs have not yet been used to measure sediment concentration in turbidity currents.

Perhaps the most crucial limitation of ADCPs is their performance in the near-bed region, which is key to understanding the interaction between flow dynamics and sediment mobilisation. The outside of the acoustic beam reflects from the

seafloor earlier than the main (axial) beam, whose direction is not vertical. Consequently, the returning wave interferes with the main measurement in the near-bed region (Sumner et al., 2013; Teledyne, 2011). This area where measurements become less reliable is called the side lobe interference area (SLIA) and its size depends on the angle of aperture of the acoustic beam and the height over the seafloor at which the ADCP is deployed (Teledyne, 2011). The decision on the height of the ADCP above the seafloor becomes crucial when planning an ADCP deployment: large distances between the ADCP and the seafloor are more likely to capture measurements from the top of turbidity currents than short distances. However, a larger distance between the ADCP and the seafloor proportionally increases the thickness of the side lobe interference area.

Further limitations of the ADCP instrument are reflections of acoustic beams from bathymetric features, the ADCP battery life and the saturation of the ADCP measuring capability. The acoustic beams emitted by the ADCP may encounter additional obstacles, such as submarine canyon walls, that perform similarly to the seafloor in terms of acoustic reflections. Similarly to the side lobe interference area, the insonified volume and dimension of the insonified footprint on the seafloor depends on the angle of aperture of the acoustic beam and the height over the seafloor at which the ADCP is deployed. The acoustic beams of an ADCP that is deployed closer to the canyon walls than the radius of the footprint would hit the canyon walls resulting in unreliable measurements. The battery consumption by ADCPs is of importance for long deployments. In these cases a compromise between the duration of the deployment and the interval between measurements is usually required. The saturation of the ADCP receiver affects the quality of the results of the datasets. Measurements of fast and dense turbidity currents have shown blanked areas in the records that suggest that the velocity and sediment concentration of some areas exceed the ADCP operating ranges of velocity and echo intensity.

Despite the limitations of the ADCPs, this acoustic instrumentation has revolutionised the monitoring of submarine density flows and enabled major advances in our understanding of the dynamics of submarine density flows in the past 10 years (Khripounoff et al., 2009; Sumner et al., 2014; Xu et al., 2013).

2.1.1 ADCP datasets analysed in this thesis

2.1.1.1 Congo Canyon datasets

ADCP data were collected during two periods (Cooper et al., 2013; 2016). From December 2009 to March 2010, a 300-kHz Teledyne© RDI Workhorse ADCP was suspended 85 m above the Congo Canyon floor from a fixed mooring. The second ADCP was located on a mooring ~700 m down-canyon and operated at a lower frequency of 75-kHz (Cooper et al., 2013). These moorings were located on the channel floor at a water depth of ~2,000 m (Figure 3.1C and 4.2) (Cooper et al., 2013). Two 300-kHz Teledyne© RDI Workhorse ADCPs were subsequently deployed at the 2013a and 2013b sites (Figure 3.1B) from January to March 2013, suspended 66 m above the canyon floor (Cooper et al., 2016). The 2013b site was located 22 km down-canyon from the 2013a site (Figure 3.1B).

The ADCPs measured flow velocity by transmitting four beams of acoustic energy into the water column, which were set at 20˚ to the vertical, and at 90˚ to each other. The 300-kHz ADCP of the 2009-2010 deployment was set up to measure a three-dimensional velocity profile that consisted of 39 individual measurements (bins), with a vertical spacing of 2 m. A velocity profile was recorded every 5 s. The ADCP records its roll and pitch, neither of which exceeded 1.5° during the duration of the instrument deployment. The height of the ADCP above the seabed (85 m) and the acoustic beam spread (20°) result in an insonified fluid cone (Figure 4.2) that covers a circle of approximately 62 m of diameter on the seabed. The exact location of the ADCP footprint within the ~200 m wide canyon floor is unknown, but the seafloor reflection at the same bin depth indicates that the footprint stayed clear of the canyon wall (Figure 2.2).

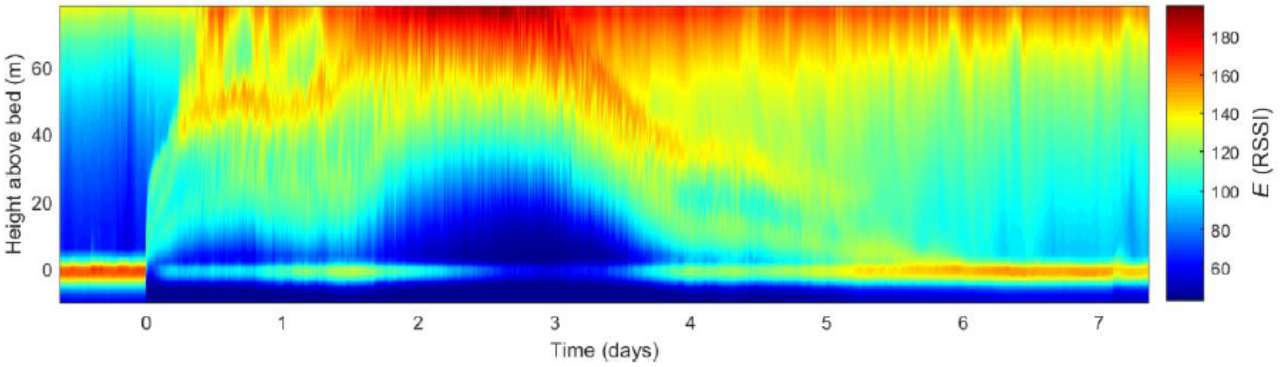

Figure 2.2. Raw backscatter plot. Backscatter data averaged over 500 seconds and all four beams of the 300-kHz ADCP throughout the turbidity current. The echo from the bed occurs around a height of 0 metre.

The combination of the 85 m of elevation of the ADCP over the seabed and the 20º angle of the acoustic beams to the vertical line results in a SLIA that covers the first ~5 m above the seabed in this work. However, the two ADCPs in the January-March deployment of 2013 were unable to record data within the lowermost 18 m of the flows (Cooper et al., 2016). This was because the moorings were located toward the margins of the canyon floor such that one or more of the ADCP's four beams returned strong echoes from steeply dipping canyon flanks. These strong returns prevented data acquisition within the lower 18 m of flow (Cooper et al., 2016). Detailed analysis of distances to seafloor returns from individual beams indicates that at both 2013 sites, the ADCPs were located above the flat canyon thalweg but within ~45 m of the canyon wall (Figure 2.3).

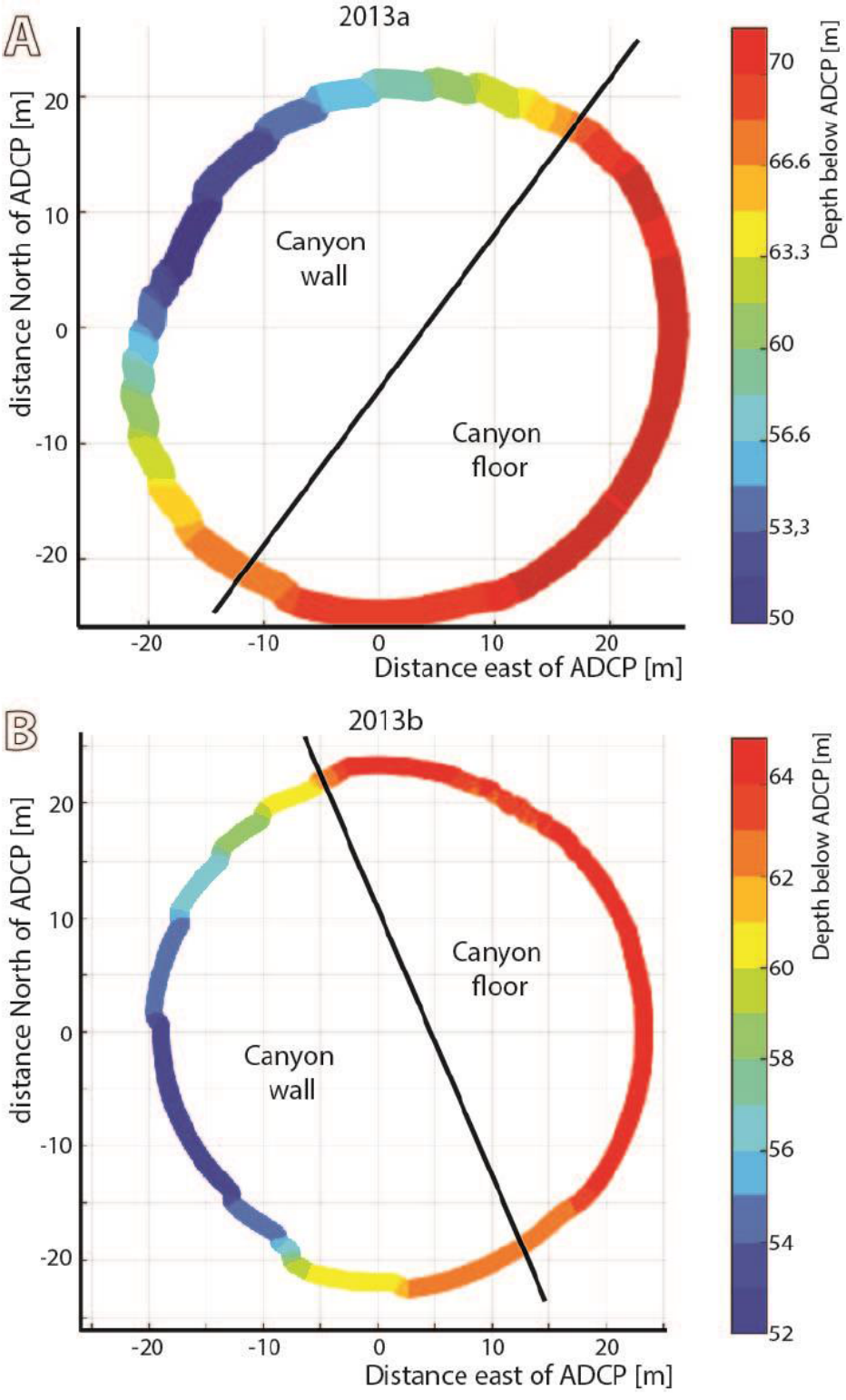

Figure 2.3. Distance to the seafloor in different directions measured by an individual ADCP beam at the up-canyon 2013a site and the down-canyon 2013b site in 2013. The centre of the ADCP beam's acoustic footprint is located on the margin of the flat (red colours) canyon floor and the more steeply inclined canyon margin (yellow-to-blue colours).

2.1.1.2 Black Sea datasets

The dataset analysed in chapter 5 was measured on the 1st and 2nd of July 2013 using a 600-kHz acoustic Doppler current profiler (ADCP) mounted on an autonomous underwater vehicle (AUV). The ADCP recorded the velocity of the helical flow along six cross-stream transects (T1-T6), and along one downstream multi-segmented transect (LS1-LS5), around the submarine channel bend (Figure 5.1).

The velocity measurements provided by the ADCP (V_{North}, V_{East} and $V_{Vertical}$) were referred to the instrument axis instead of to geographical coordinates because the ADCP was mounted on a moving vehicle. Additional processing was required to analyse heading, pitch and roll of the AUV and to refer the velocity measurements to global geographical coordinates.

2.2 Flow front velocity of Congo Canyon flows derived from 300-kHz ADCP dataset (2009-2010 deployment)

The frontal velocity of the turbidity current is derived from the difference in arrival time of flow at each of the four acoustic beams of the 300-kHz ADCP deployed during 2009-2010 (Figure 2.4). The footprint of four ADCP beams spans ~45 m X ~ 45 m on the canyon floor. The arrival time of the flow at each of the beams is recognized by a strong increase in the backscatter intensity (Figure 2.4). The distance between the centers of the four beams is known, but their orientation relative to the direction of flow front propagation is uncertain (angle α in Figure 2.4). The distances between centers of ADCP beams must therefore be calculated in the direction of travel of the flow front (Figure 2.4) to calculate flow front velocities. This is done by expressing the arrival time at the individual beams as a function of the flow front velocity. The resulting frontal flow velocity was found to be 1.2 to 1.5 m/s. Uncertainties in the calculated flow front velocity are due to uncertainties in the arrival times resulting from the 5-s spacing between consecutive measurements (Figure 2.4). This method assumes that the ADCP heading is stable over the period considered (a few tens of seconds, Figure 2.4), that the frontal velocity does not fluctuate significantly as it travels between ADCP beams, and that the flow front is reasonably straight over distances of several tens of meters orthogonal to its direction of travel.

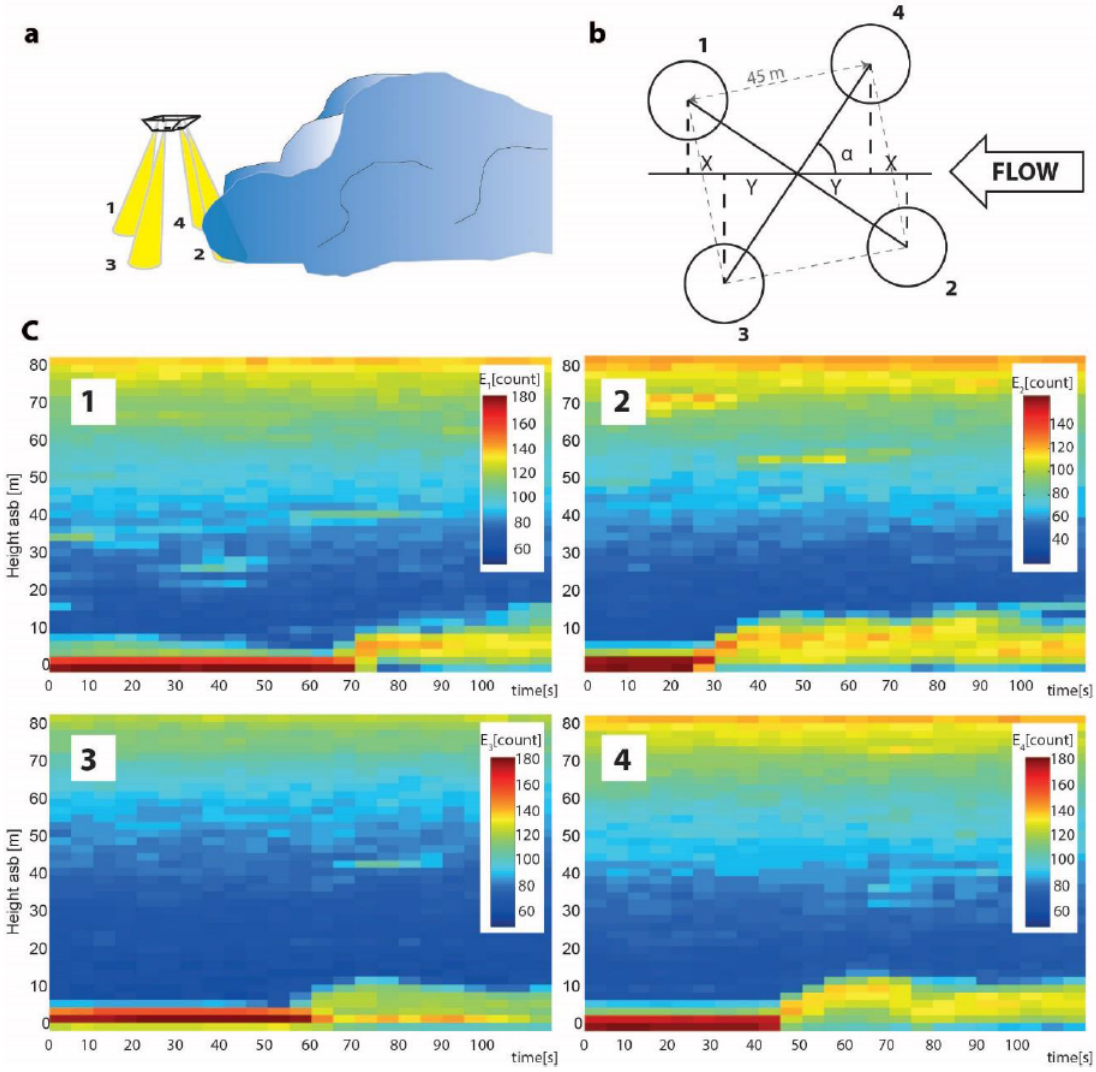

Figure 2.4. Illustration of the method used to calculate flow front velocity. (A) Schematic diagram of flow approaching the deployed ADCP **(B)** The geometry of the four beams, which can be used to define the following relationships for flow front velocity (V) in terms of distances X and Y, and time delays between the flow from reaching ADCP beams 1 to 4 ($t_{4\text{-}2}$ for time between beams 4 and 2 etc); $V = X(t_4\text{-}t_2) = X(t_1\text{-}t_3)$; $V = 2Y\ (t_3\text{-}t_4)$; $V = (X+2Y)/(t_3\text{-}t_2) = (X\text{-}2Y)/(t_1\text{-}t_4)$. **(C)** Echo intensity (E; expressed in counts) recorded by each individual ADCP beam at flow arrival (yellow-greenish area). Highest echo intensity centered on 0 metre above seafloor (asb) indicates the position of the seabed. Number in each subpanel indicates the ADCP beam number.

2.3 Velocity fluctuations from Congo Canyon 300-kHz ADCP dataset (2009-2010 deployment)

Large-scale velocity fluctuations were used here as a proxy for turbulence intensity within the flow (Figure 3.3C). These velocity fluctuations were calculated by (i) calculating the average velocity over a 1-min period, (ii) subtracting the 1-min average velocity from a single velocity measurement made at the center of this 1-min period, (iii) squaring the velocity difference values, (iv) calculating an average velocity difference profile over a 500-s period, and (v) taking the square root of the resulting average. Given the 5-s measuring resolution and the 1-min moving average, these velocity fluctuations are biased toward large-scale velocity fluctuations and should therefore only be used as a crude indicator of turbulence intensity. In addition, it should be taken into consideration that the velocity fluctuations will also include any possible noise on the data.

2.4 Secondary velocities from Congo Canyon 300-kHz ADCP dataset (2009-2010 deployment)

Secondary circulation is a balancing flow in a plane perpendicular to the flow direction. Motion towards one side of the plane at certain flow depths is compensated by motion towards the opposite side at the rest of the flow depths. Secondary velocities are the velocity components in this plane, across the depth-averaged flow direction. In our study, the flow depth has been yielded from the integrated system of equations (Ellison and Turner, 1959) that provides flow top distance to the seabed at each time. The seabed has been located by a contrasting high value of echo intensity in a profile of decreasing echo intensity measurements in the water column below the ADCP. The measurements within the SLIA were removed and substituted by linear interpolated velocities from the deepest valid bin measurement to zero at seabed level for the three components of the velocity (V_{North}, V_{East}, $V_{Vertical}$). The maximum velocities have been located in the resulting working dataset. Due to the velocity extrapolation method, flows whose maximum velocities are within the SLIA will show their peak velocity height at the top of this area instead of at the actual height, which is within the unreliable SLIA measured area (Figures 4.3 and 4.4).

The depth-averaged flow direction was calculated from the depth-averages of the North and East components of the velocities given by the ADCP. Secondary velocities towards the outer bend are positive while negative towards the inner bend (Figures 4.3 and 4.4).

The calculation of secondary velocity gives values occasionally close to the speed of seawater that has been identified as tidal currents (Figure 4.3). Tides strong enough could affect the results of the analysis of secondary circulation. Secondary velocities for the periods when this happens have been removed from the results (Figure 4.3).

Depth-profiles of secondary velocities were analysed to identify patterns in the configuration of the secondary circulation. Secondary velocities were calculated for each flow time and arranged by thickness. The average of these values by thickness constitutes the depth-profiles of secondary velocities (Figure 4.4A). This process was repeated for each turbidity current and the resultant depth-profiles were averaged into one only profile (Figure 4.4B).

Depth-profiles of different thicknesses are formed by different numbers of measurements. The depth-profiles were normalized by depth and then averaged to obtain a unique profile for primary velocity (Figure 4.4D) and for secondary velocity (Figure 4.4E).

2.4.1 Evolution of primary velocity - depth-average magnitude and flow direction

The definition of primary and secondary velocity intrinsically links both variables through the flow mean direction. Figure 2.6 shows the evolution of the depth-averaged primary velocity in relation with the flow mean angle for the same flows shown in Figure 4.3.

The consistency of the flow direction during all the flows suggest that all flows were confined in the canyon, whose downstream direction points approximately 212º in relation with the geographical North.

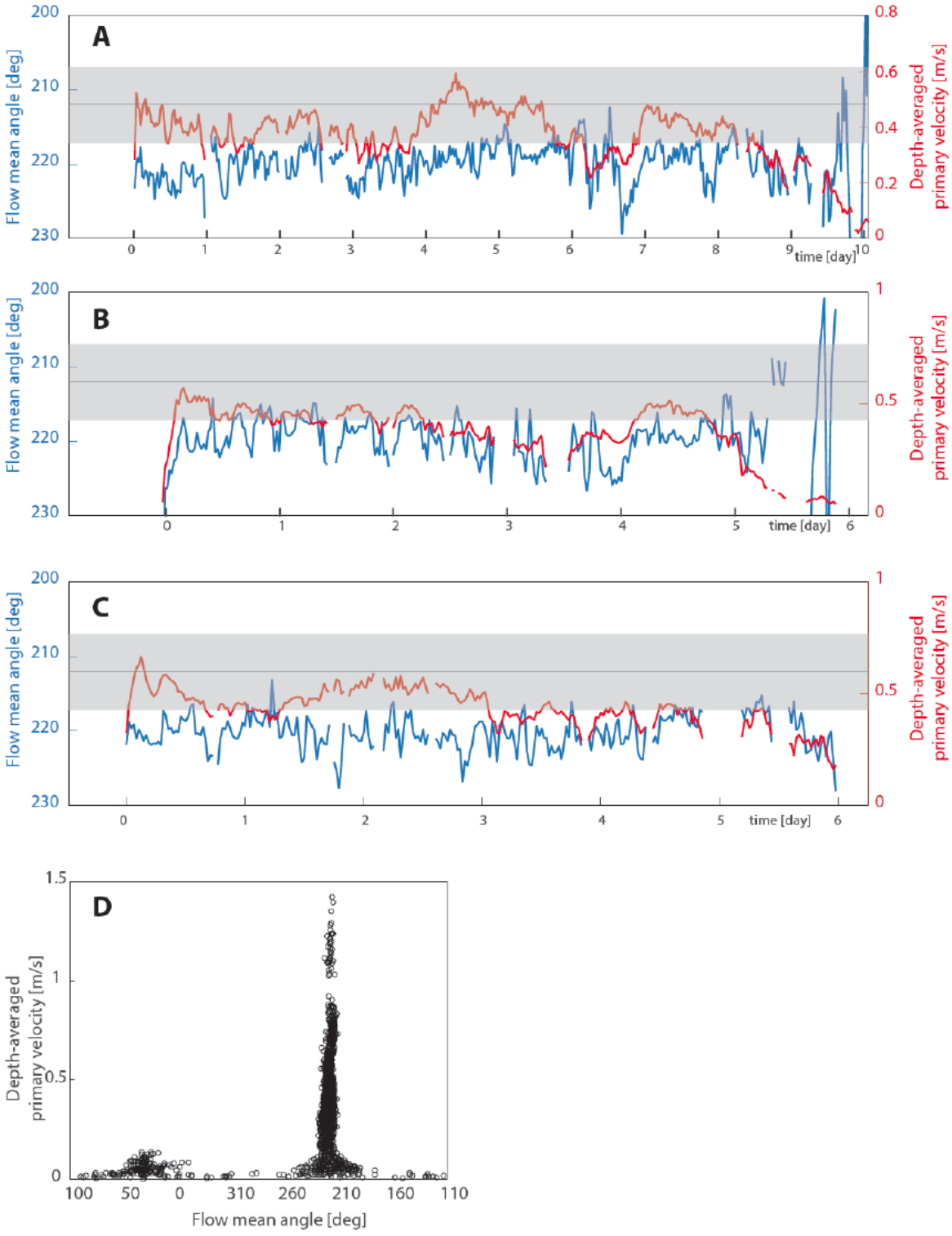

Figure 2.6. Comparison of depth-averaged primary velocity and flow mean angle. (A) Flow 1. **(B)** Flow 4. **(C)** Flow 10. **(D)** Combination of all flows. Results correspond to 30-minute averages of measurements. Grey line in panels A-C shows the measured angle of the channel axis at the deployment site (212º). Greyed area represents a +/- 5º variation from the channel axis angle that accounts for the 10 m X 10 m bathymetry resolution accuracy.

2.4.2 Variability in secondary circulation of depth-normalized profiles

Figure 4.4 shows that the secondary velocity spans between ~+/- 0.2 m/s for profiles sorted by thickness (Figure 4.4B) while the average of the secondary velocity of depth-normalized profiles spans between ~+/-0.02 m/s (Figure 4.4.E). Figure 2.5 shows that the variability in the depth-normalized secondary circulation profiles supports the difference. The presence of variability in the exact structure as a function of the flow thickness leads towards an averaged value of secondary velocities one order of magnitude smaller than the individual profile depth-normalized measurements.

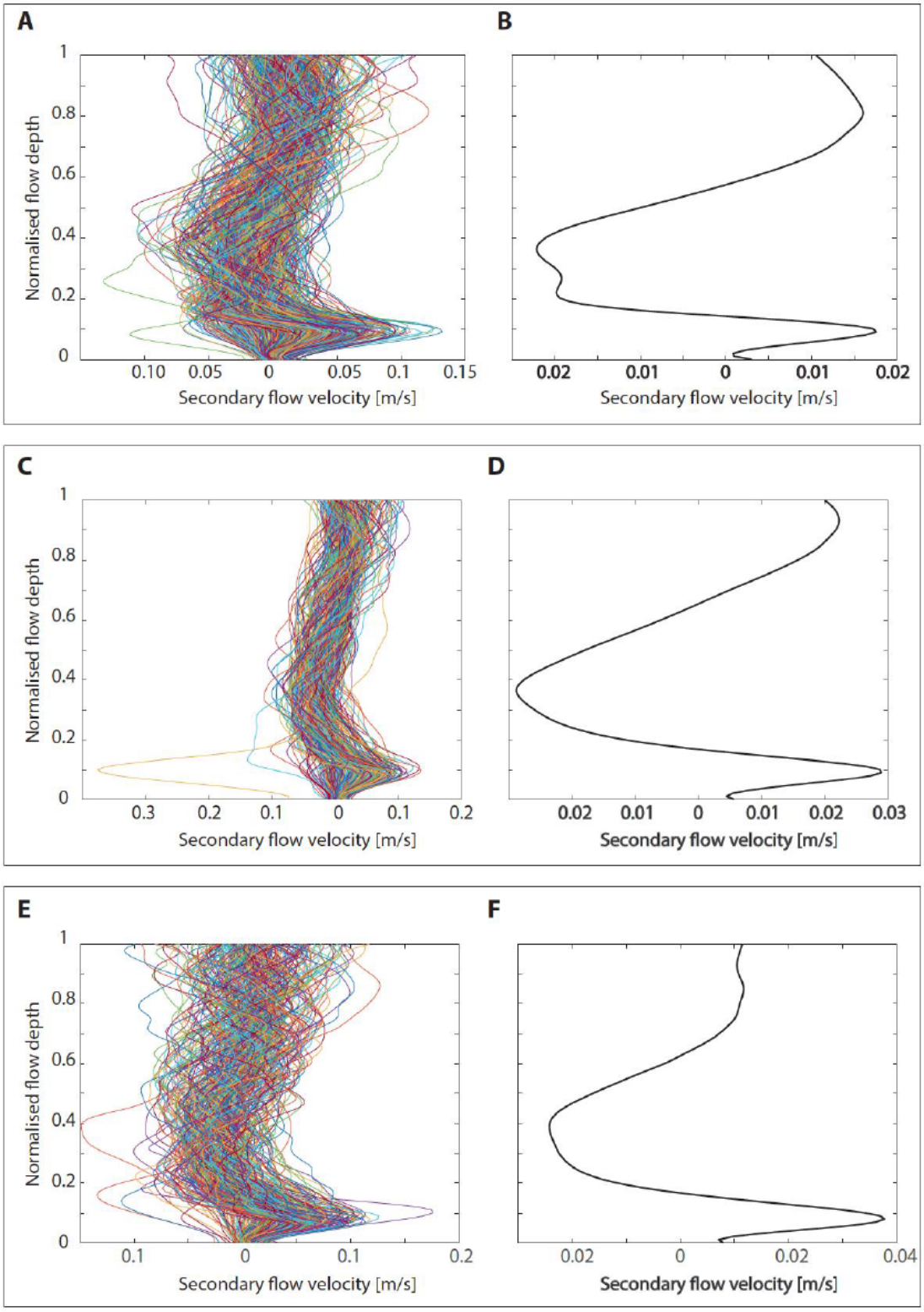

Figure 2.5. Variability in secondary circulation measurements of depth-normalized flows shown in Figure 4.3 (A) Flow 1, depth-averaged secondary velocities of flow profiles, **(B)** Flow 1, mean of depth-averaged secondary velocities profiles, **(C)** Flow 4, depth-averaged secondary velocities of flow profiles, **(D)** Flow 4, mean of depth-averaged secondary velocities profiles, **(E)** Flow 10, depth-averaged secondary velocities of flow profiles, **(F)** Flow 10, mean of depth-averaged secondary velocities profiles.

2.5 Sediment concentration from Congo Canyon 300-kHz and 75-kHz ADCP datasets (2009-2010 deployment)

Suspended sediment concentrations within the flow (Figure 3.3D) were obtained by inversion of the acoustic backscatter (Figure 2.2) acquired by a 300-kHz ADCP (Thorne et al., 1995). They were validated using a second ADCP located on a mooring ~700 m down-canyon, which operated at a lower frequency of 75-kHz (Cooper et al., 2013). This inversion analysis is innovative, because these are the first sediment concentration values derived for any full-scale turbidity current from multiple-frequency ADCPs.

The basic approach is to first convert the raw backscatter data from the receiver signal strength indication (RSSI) units to a logarithmic decibel scale and then compensate for any bias due to variable orientation of the ADCP beams during the measurements. Using the 300-kHz ADCP, the loss of strength (attenuation) of echo from the bed was calculated by comparing the bed echo strength before the flow event to the echo strength during the flow. A sediment concentration profile was inferred assuming uniform grain size throughout the flow, along with a reference sediment concentration just above the bed. The sediment concentration profile within the flow was computed in an iterative fashion such that it best fit the observed change in attenuation of the bed echo before and during the flow. We then used the second, 75-kHz ADCP, data to constrain the most likely grain size within the flow at each given point in time. This assumes that there is a single grain size in a vertical profile above the bed at each given point in time. This is done by taking the sediment concentration profile and reference concentration inferred previously from the 300-kHz ADCP data and determining the grain size(s) that produces the closest fit to the bed attenuation seen in the 75-kHz ADCP data. Finally, we were able to assess assumptions regarding a uniform grain size within the flow using a calculated parameter, Kt, which essentially indicates local departures from the backscatter profiles assuming a single grain size.

This method, which first used the 300-kHz ADCP data and then the additional 75-kHz ADCP data, is now outlined in more detail below. The raw backscatter data in RSSI, E, were converted to linear backscatter counts, V, for all beams using

$$V = 10^{K_c\left(\frac{(E-N)}{20}\right)} \quad [1]$$

where Kc is a measured constant for each of the four transducers (values supplied for deployed instruments by Teledyne RDI Inc.) and N is the noise level for each transducer channel, determined as the mean of the acquired values at the maximum sediment attenuation during the acquisition period. The orientation of the ADCP biased the measured backscatter intensity, probably due to the side lobe interference in the near-bed bins and variation in the bed elevation across the interrogation volume. Hence, for each set of four beam profiles acquired with the 300-kHz ADCP, the heading of the ADCP compass was used to remove the heading bias in backscatter intensity. This allowed us to recover and use the beam that had the lowest acoustic side lobe interference. Backscatter (V) from homogeneous suspensions of sediment is randomly distributed, so profiles were averaged by determining the root mean square value of 100 consecutive profiles over 500 s.

The ADCP measurement bin with the consistently highest raw echo magnitude throughout the record (bin 40) was assumed to contain a bed echo. The bed echo attenuation throughout the duration of the turbidity current was then calculated as the ratio of the backscatter in bin 40 during the event to the backscatter in the same bin of the same transducer beam at the same compass heading before the event. Figure 2.7 shows the mean bed attenuation values averaged for the four transducers for the duration of the event, as well as the bed attenuation of the lower-frequency 75-kHz ADCP. The values are expressed in decibel and are derived as $20\log_{10}(A_{bed})$, where

$$A_{bed} = 20\log_{10}\left(\frac{V_{event}}{V_{clear\ water}}\right) \quad [2]$$

An initial sediment concentration profile can then be derived using water column backscatter and an initial reference mass concentration at the bed, assuming that the flow contains a uniform grain size. This is because the mass concentration of suspended sediment, M(r), as a function of range from the ADCP transducers, r, is related to the backscatter magnitude, $V_{rms}(r)$, by the following relationship (Thorne and Hurther, 2014)

$$M(r) = \left(\frac{V_{rms}(r)\varphi(r)r}{K_t\ K_s(r)}\right)^2 e^{4(\alpha_w r + \alpha_s(r))} \quad [3]$$

where $\varphi(r)$ is a correction for the transducer's near field (Downing and Thorne, 1995); Kt should be constant and describes the sensitivity of the individual transducer; Ks is related to the scattering properties of the sediment in suspension and is a function of the particle type and size relative to the acoustic frequency; α_w is the sound attenuation due to the properties of the water and is calculated using the formula of Francois and Garrison (1982a, 1982b) as 0.0079 nepers/m, using a measured mean water temperature of 3.7˚C and mean depth of 1,924 m, with an assumed pH of 8 and 35 ppt (parts per thousand) salinity; and α_s is the sound attenuation due to suspended sediment. The range, r, is divided into discrete units corresponding to the bin size of 2.13 m along the acoustic beams, which are inclined at 20˚ to the vertical and correspond to a 2.0-m vertical bin spacing through the water column.

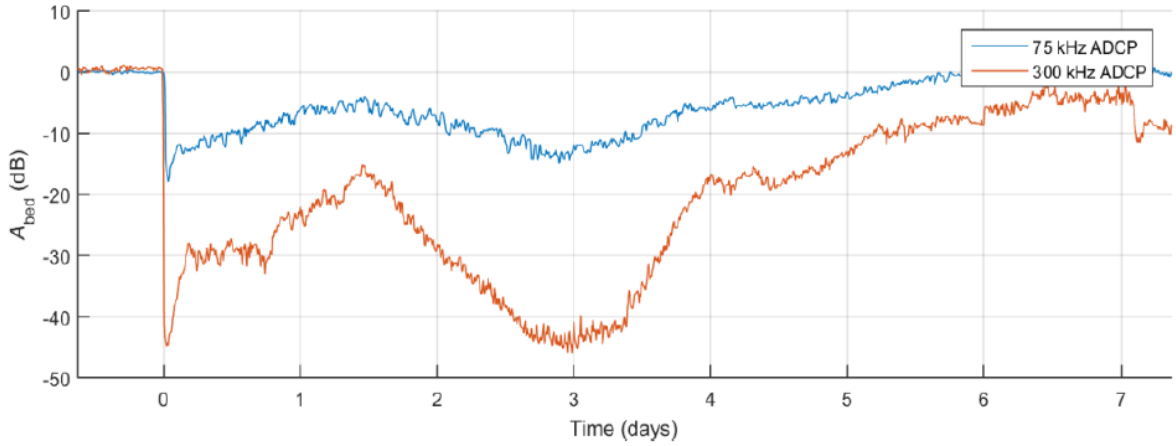

Figure 2.7. The bed echo attenuation for 300- and 75-kHz ADCP during the turbidity current.

Solving Eq. 3 is nontrivial because the α_s (r) expression is itself a function of M(r)

$$\alpha_s(r) = \int_0^r \xi(r) M(r) dr \qquad [4]$$

where $\xi(r)$ is a function of the particle type and size relative to the acoustic frequency. The explicit solution of Lee and Hanes (1996), which assumes that the grain size is constant for all ranges from the ADCP transducers, was used to close the equations. This assumption of a uniform grain size is necessary given the lack of information about grain size variability, but it also removes the

requirement of knowing the values of the Ks and Kt constants in Eq. 3 (Thorne and Hanes, 1996). As a result, the sediment concentration profile M(r) is given by

$$M(r) = \frac{\beta(r)^2}{\beta_{ref}^2 / M_{ref} - 4\xi \int_{r_{ref}}^{r} \beta(r)^2 \, dr} \quad [5]$$

where

$$\beta(r) = V_{rms}(r) r e^{2\alpha_w r} \quad [6]$$

and Mref is a known concentration at a reference range, r_{ref}. The first value of Mref used to determine M(r) is a guess, because the concentration at the reference range is unknown. However, for the inversion to remain constrained, the reference range needs to be set at the farthest range, that is, the bed, to prevent the accumulation of errors beyond the reference range. The attenuation coefficient constant, ξ, for the single, assumed, grain size is derived as the sum of acoustic scattering and viscous absorption expressions through the water column. The acoustic scattering component is evaluated by first calculating the scattering cross section, χ, using the heuristic expression of Moate and Thorne (2012), which was developed as a generic expression for sands of varying mineralogy. The scattering attenuation coefficient is then determined by

$$\xi_{scattering} = \frac{3\chi}{4a} \quad [7]$$

The viscous absorption component, $\xi_{viscous}$, is calculated using Urick's (1948) formula using a value of 1.52 m^2/s for the kinematic viscosity of water at 3.7°C and an assumed density of 2,650 kg/m^3 for the sediment. The plot in Figure 2.8 shows the values of the sediment attenuation coefficient, ξ, for a single value of grain diameter across the range of 0.001 to 1 mm for both ADCP frequencies. For small particles, the viscous absorption term dominates and is at a peak for clay/silt particles. For diameters greater than ~400 μm, the scattering term dominates and ξ increases with diameter. The cumulative through-water attenuation of the derived mass concentration profile can be calculated from the transducers to the bed (bins 1 to 39), $A_{profile}$, using the profile of M(r) obtained in Eq. 5

$$A_{profile} = e^{\int_{o}^{r_{ref}} -4\xi M(r) dr} \quad [8]$$

The reference mass concentration can then be adjusted iteratively through the above equation set until the cumulative attenuation of the derived concentration profile matches the bed echo attenuation and, in essence, when the difference between the two attenuation values, $A_{profile} - A_{bed}$, reduces to approximately zero.

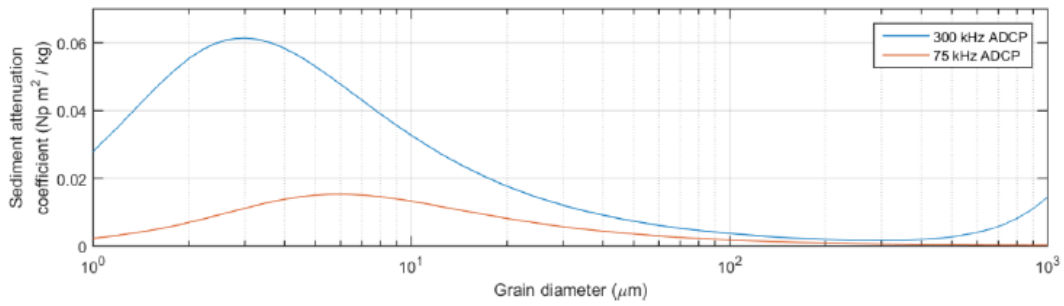

Figure 2.8. Sediment attenuation coefficient (ξ) for 300- and 75-kHz frequencies, by particles with diameters between 1 and 1,000 μm.

The second 75-kHz ADCP acquired backscatter data over a range of ~230 m above the bed at a location on the canyon floor approximately 700 m downstream from the 300-kHz ADCP. The bed echo attenuation, A_{bed} (Figure 2.7), enables a method of estimating the grain size in suspension by evaluating $A_{profile}$ at 75-kHz using the M(r) derived with the 300-kHz ADCP. This assumes that the suspended sediment structure of the flow remains unchanged over the distance of ~700 m along the thalweg. $A_{bed} - A_{profile}$ is therefore calculated for all profiles for a single grain size.

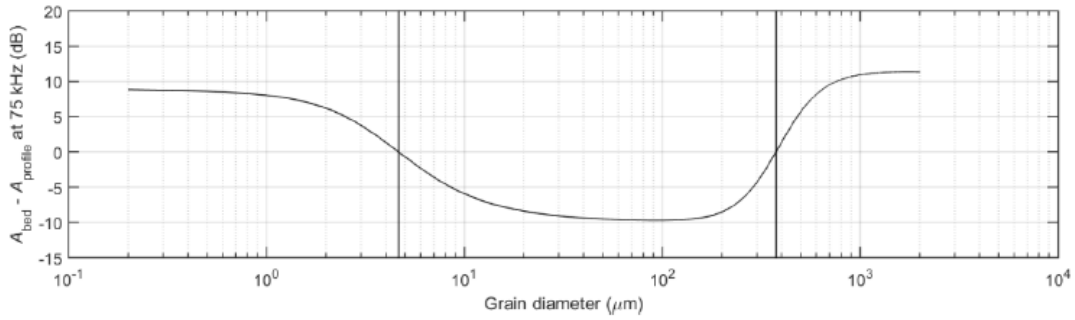

Figure 2.9. Difference between the bed echo attenuation (Abed) and the predicted cumulative echo attenuation (Aprofile) within the water column from the 75-kHz ADCP data. The value of $A_{profile}$ is based on the sediment concentration profile previously calculated from the 300-kHz ADCP data. The difference ($A_{bed} - A_{profile}$) is calculated for a range of grain sizes from 2 μm to 2,000

μm. Only two grain sizes (shown by vertical lines) produce a zero value of A_{bed} – $A_{profile}$ and thus satisfy both the 75-kHz and 300-kHz backscatter observations. This analysis uses backscatter data comprising averages of 100 consecutive measurements (pings) acquired over 500 s. It also assumes that a vertical profile through the flow at a given point in time comprises only one grain size, whereas it is likely that grain size varies with height above the bed.

The suspended grain size for a given concentration profile is found by iterating through a range of possible grain sizes and comparing the error between A_{bed} and $A_{profile}$ at 75-kHz for each profile. Two solutions were found for each set of profiles, considering a plausible range of grain diameters from 0.1 to 1,000 μm. The values of $A_{bed} - A_{profile}$ for a single averaged profile are shown in Figure 2.9, and the two grain size solutions throughout the event are displayed in Figure 2.10.

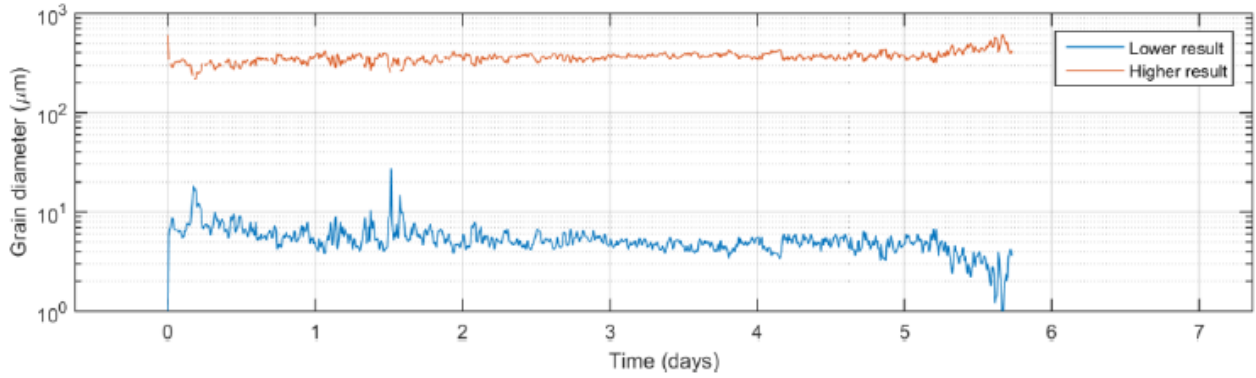

Figure 2.10. The suspended grain size results derived from the comparison between the 300- and 75-kHz ADCP bed echo. Two grain sizes satisfy both the 75-kHz and 300-kHz ADCP data ('lower result and higher result'; Figure 2.8). This figure shows how those two grain sizes vary over time at the study site. However, this still assumes that there is a single grain size in the flow at each point in time, and that grain size is not changing with height in the flow. Figure 2.13 shows constraints on how grain size varies with height above the bed, as well as through time.

The smaller of the two possible grain sizes (4.23 μm) is the most realistic option, because it closely matches the average D_{50} of nearby sediment cores that was 2.8

μm (Figure 2.12). The final result (Figure 2.11) was therefore derived using a uniform grain size of 4.23 μm throughout the event.

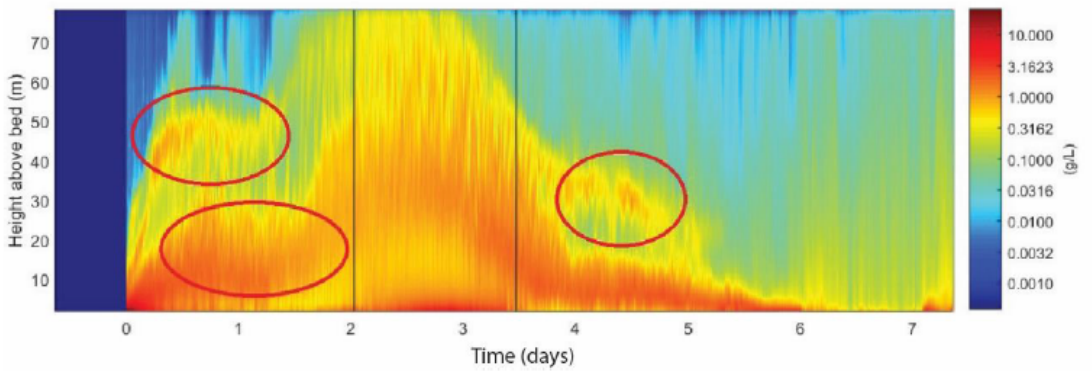

Figure 2.11. Sediment concentration (g/liter) derived using the ADCP backscatter magnitudes. This analysis assumes that the flow contains a uniform grain size diameter of 4.23 μm. Potential artefacts are shown by red circles, where higher sediment concentrations overly lower sediment concentrations. These artefacts may result from variations in grain size within the flow, or from other factors, such as flow interactions with tidal currents. The periodic increase of the background water velocity has been interpreted as tides (Figure 3.3). This increase in background water velocity coincides with an increase in raw echo intensity in the water column (Figure 2.2). We suggest that the increase in echo intensity is due to a wake of sediment from the turbidity current that experiences the friction at the flow top from the opposite-directed tide.

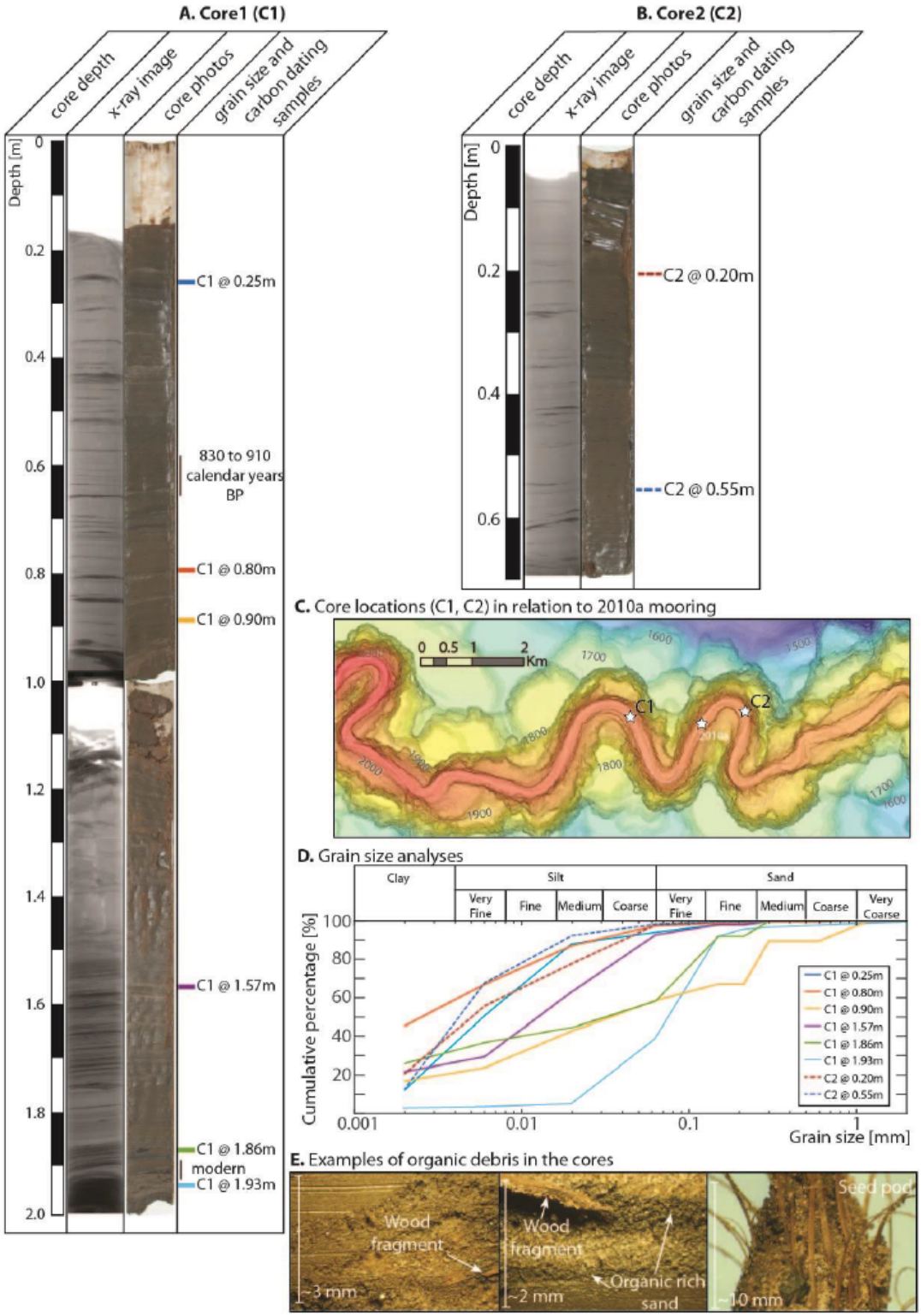

Figure 2.12. Cores from floor of Congo Canyon. (A and B) Core photo, x-ray images and sample locations. Dating in calendar years before present. **(C)** Core locations in relation to mooring site. **(D)** Grain size analyses. **(E)** Examples of organic debris from the cores.

A key assumption is that the flow contains a single grain size, and we note that grain size may vary vertically and through time, and multiple grain sizes may be present at one location. In general, sediment concentrations tend to be higher in the lower part of the flow, as expected for stable density stratification (Figure 2.11). The highest sediment concentrations occur at the base of the frontal-cell. Sediment concentrations also increase in the tail of the flow, where vertical concentration gradients likely become stronger. However, there appear to be artefacts within this sediment concentration data set (shown in red circles in Figure 2.11), where higher sediment concentrations overlie lower sediment concentrations. This inverted density stratification is likely to be unstable and unrealistic. Our analysis assumes a single grain size within the flow, and these artefacts may be due to vertical changes in grain size or other factors such as zones of strong turbulence or the influence on acoustic returns of refraction at interfaces with different densities.

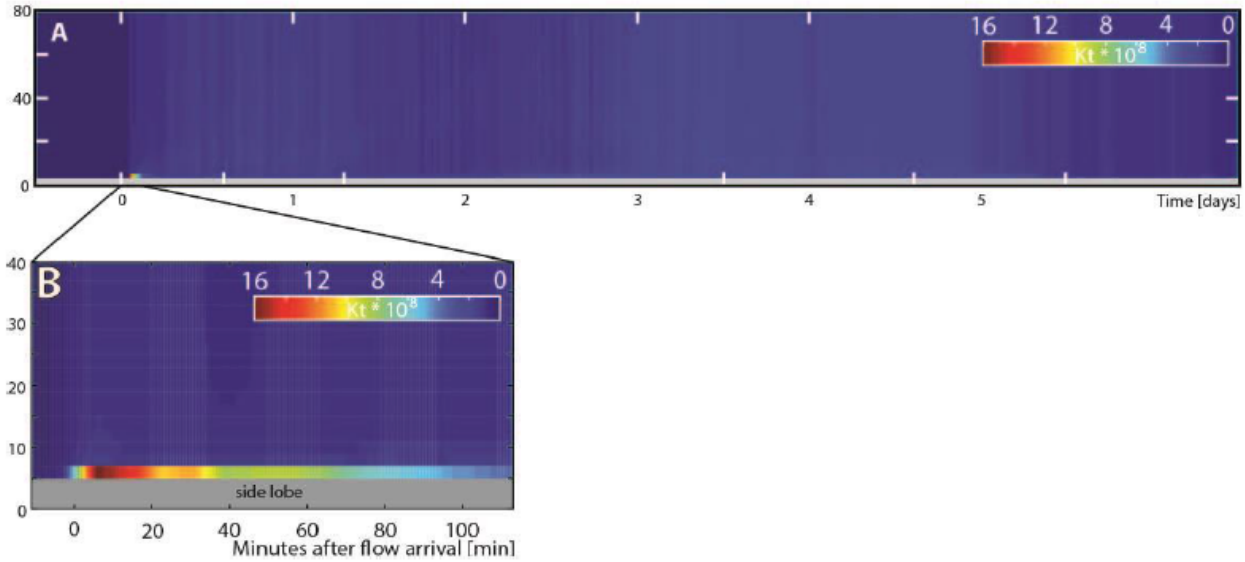

Figure 2.13. The calibration constant Kt. This constant is a measure of differences between the local grain size in the flow, and an assumed uniform grain size throughout the entire flow. This figure therefore shows that the lower 2-3 metres of the flow, during the initial 20-30 minutes of the event, is much coarser grained than the rest of the turbidity current. **(A)** Variation in Kt profiles throughout the whole 6 day long turbidity current. **(B)** Changes in Kt during the initial 2 hours of the flow, within the lower 40 metres.

To provide an estimate of uncertainties in the calculated sediment concentrations, and the amounts of sediment transported by each turbidity current (Table 3.1), we also calculated sediment concentrations for flows with uniform grain size that vary from 3 to 20 μm, not just 4.23 μm. This grain size range reflects modal grain sizes seen in canyon floor cores in the general vicinity of our mooring site (Figure 2.12). Flows containing a uniform grain size of 3 μm would have sediment concentrations that are 90% of those calculated using a uniform grain size of 4.23 μm. Conversely, flows with a uniform grain size of 20 μm would have sediment concentrations that are 320% of the values calculated using a grain size of 4.23 μm. These calculations, with uniform sediment grain sizes of 3 to 20 μm, are then used to give the range of sediment transported by an average turbidity current (for example, ~1.1 to 3.8 Mt) in the text. However, these ranges neglect the effects on backscatter inversions from spatial or temporal changes in grain size within a single flow.

As a test of the methodology, for a concentration profile, M(r), a calibration constant, Kt, can be derived for all ranges, r, by evaluating

$$K_t = \beta M^{1/2} e^{2r\alpha_s} \quad [9]$$

If the uniform grain size assumption for a given profile is true, then the value of Kt should remain constant throughout the range from the transducers to the bed, because Kt is a fixed acoustic property of the transducer. The values of Kt are plotted in Figure 2.13. During the first 20 to 30 min, Kt increases significantly in the near-bed region (Figure 2.13). This suggests that the mean grain size increases toward the bed and that, as a result, sediment concentrations in those initial near-bed bins are probably underestimated in Figure 2.11. Throughout the remainder of the event, the profiles of Kt remain approximately constant, suggesting that the grain size remains relatively constant, albeit with some minor variations that map to the artefacts discussed above (red circles in Figure 2.11).

2.6 Bed shear stresses and Shields diagram for Congo Canyon 300-kHz ADCP dataset (2009-2010 deployment)

Bed shear stresses determine which sediment sizes the flow can transport, and whether the flow will pick up additional sediment from the bed or sediment will

settle out of the flow. Bed shear stresses are expressed as a bed shear velocity (u*), which can be calculated in two ways.

First, u* can be derived from the shape of the vertical velocity profile below the velocity maximum (Yu and Tan, 2006). This method assumes that the velocity profile near the bed is logarithmic. The slope of that log-linear plot is used to calculate the value of u*. We only used velocity profiles that had three or more measured values below the velocity maximum. In some parts of the flow, the ADCP could not measure below the velocity maximum, and this method cannot be applied. These u* values are plotted as blue squares in Figure 2.14.

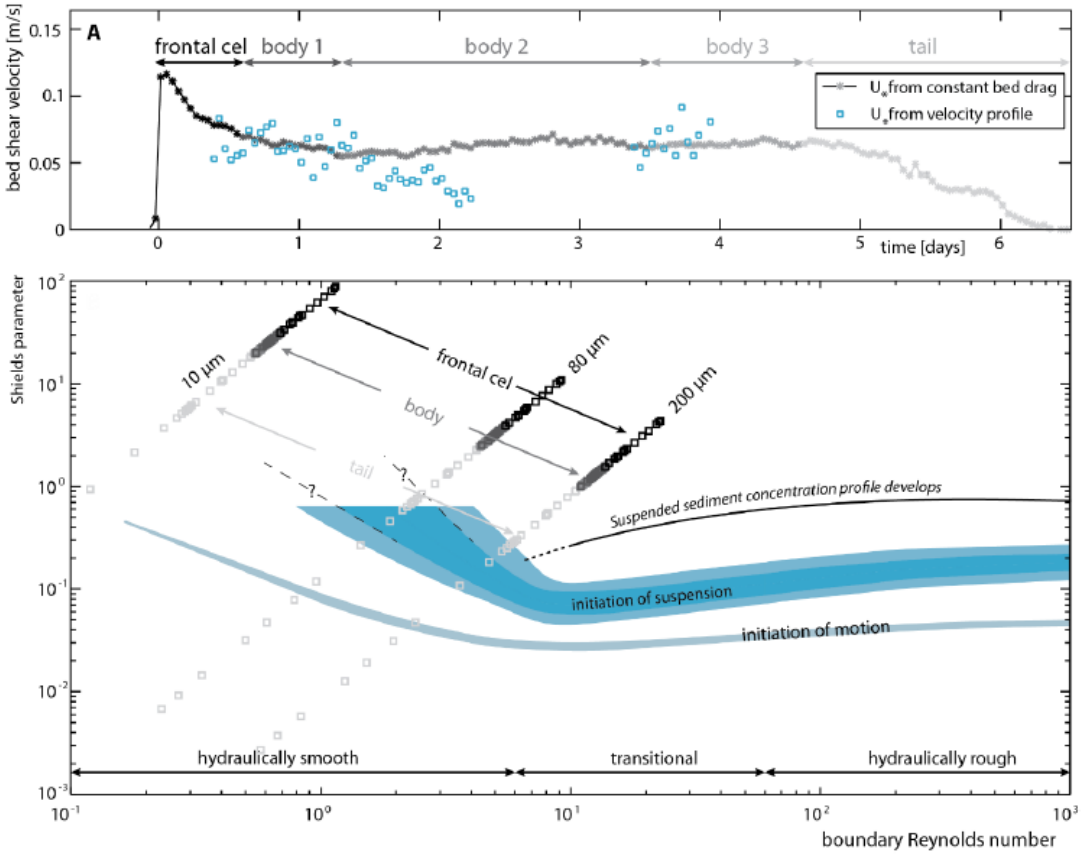

Figure 2.14. Bed shear stresses generated by the flow. (A) Bed shear velocities plotted over time. The blue square are shear velocities extracted from the gradient of the near-bed velocity profiles. The black and grey stars are shear velocities extracted from the velocity maximum based on a fixed bed drag coefficient. **(B)** Shields diagram (modified from de Leeuw et al., 2016) showing which grain size can be transported either along the bed or in suspension. Here we plotted three grain sizes that are expected in the Congo Canyon (200 µm, 80 µm, and 10 µm). The plot shows that the frontal cell of the flow is the most

capable of suspending sediment, and will erode sediment from the canyon floor to maintain a suspended sediment concentration profile. The values measured in the body of the flow are lower, but still sufficient to keep a suspended sediment concentration profile. At the tail of the flow the values drop below the initiation of suspension line, and will no longer be able to suspend the sediment in the flow. There are as yet few constrains on the initiation of suspension for clay-size particle, as indicated by the questions marks.

The second method of calculating the bed drag coefficient links the bed shear velocity to the maximum flow velocity (Komar, 1977). The bed drag coefficient is assumed to only relate to bed roughness and will be constant for a fixed location during the flow. This allows us to extrapolate bed shear velocities for the whole flow, based on the maximum flow velocities. Bed shear velocities are then used to calculate Shields numbers and boundary Reynolds numbers for different grain sizes. We show calculations for three grain sizes: 200, 80, and 10 μm. By plotting the results in a Shields diagram (Figure 2.14) (de Leeuw et al., 2016), it can be seen that the frontal-cell is powerful enough to suspend all three grain sizes under the assumption of a cohesion-less bed. The decreasing values of the Shields number and the boundary Reynolds number over the body of the flow indicate that erosion will become less vigorous, but sediment will remain in suspension. Lower values of u* in the tail show that sediment is no longer supported and will begin to settle out. It appears that this produces relatively high sediment concentration layers near the bed within the tail of the flow (Figure 2.11).

2.7 Calculations of water, sediment, and organic carbon discharges from the Congo Canyon 300-kHz ADCP dataset (2009-2010 deployment)

Water discharges were calculated by multiplying the flow velocity measured by the ADCP at each height above the canyon floor (that is, each bin) by the width of the canyon at that corresponding height and the vertical height range of each bin (~2m). These values were then summed to give the total water discharge through time (Figure 2.15).

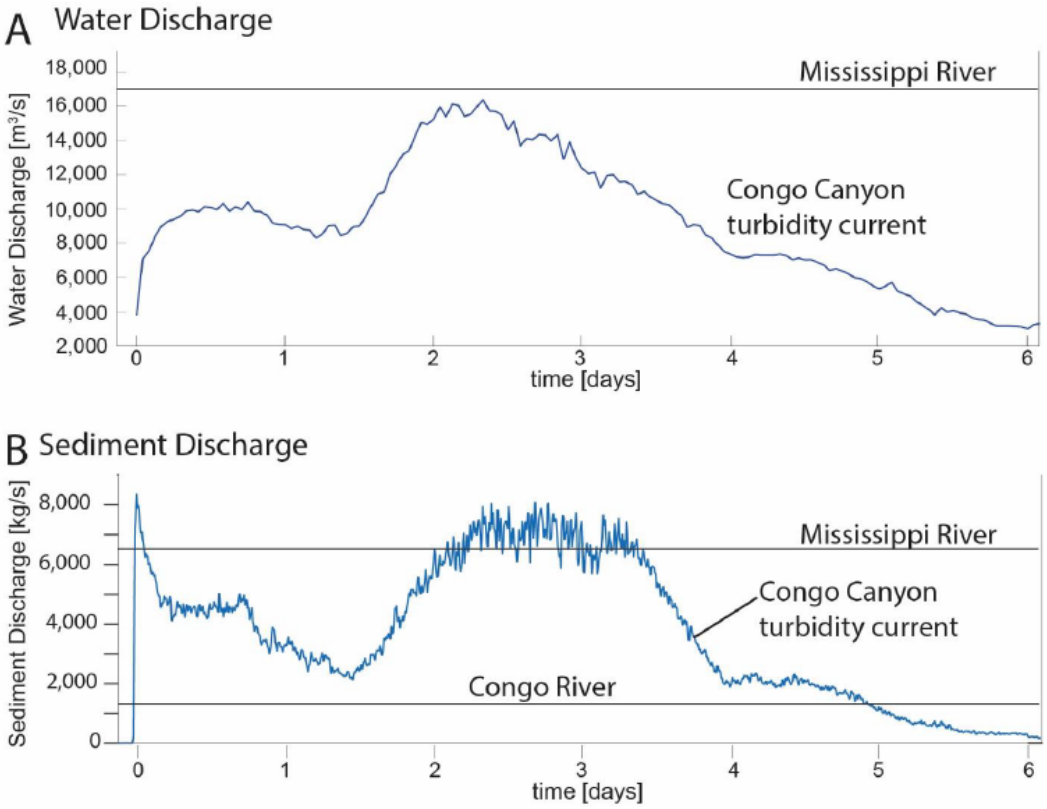

Figure 2.15. Comparisons of the instantaneous sediment and water discharges in the Congo Canyon turbidity current shown in Figure 3.3, with the mean annual discharges of water and sediment in major rivers. (A) Water discharge in the Congo Canyon turbidity current (blue line) and Mississippi River (Milliman and Syvitski, 1992) (black line). The Congo River has a mean annual discharge of 41,000 m3/s (Milliman and Syvitski, 1992). **(B)** Sediment discharge within the turbidity current studied here, compared to the average annual sediment fluxes from the Mississippi and Congo Rivers (Milliman and Syvitski, 1992).

Estimates of sediment concentration were then derived from ADCP measurements at each bin, as described above. These sediment concentrations will have significantly greater uncertainties than the ADCP's velocity measurements (see discussion in section 2.5). Sediment concentrations were multiplied with water discharges calculated for each bin to calculate the overall sediment flux during each turbidity current (Figure 2.15). This sediment flux may be an underestimate because it does not include the lower 3 to 4 m of the flow, which is within the ADCP blanking distance. The average sediment flux during a turbidity current is estimated to be 2.1 X 10^3 kg/s (Table 3.1), assuming a uniform grain size of 4.23

μm. Assuming a uniform grain size within each flow, which varies between 3 and 20 μm, the average amount of sediment carried by an individual turbidity current then becomes 2.1 X 10^3 to 6.7 X 10^3 kg/s. The average turbidity current in the Congo Canyon would then carry a total of ~1.2 Mt of sediment during its 6.7-day duration, assuming a uniform grain size of 4.23 μm, or 1.1 to 3.8 Mt for uniform grain sizes that range between 3 and 20 μm. The amount of sediment transported by turbidity currents each year (~22 Mt) is calculated by assuming that the average sediment flux of 2.1 X 10^3 kg/s occurs during 33% of the time (Figure 3.3A).

An average organic carbon content of 3 to 5% weight was assumed for the sediment carried within the turbidity current. This value is based on the organic carbon content measured within turbidity current deposits on the Congo Fan, which are dominated by terrestrial (rather than marine) organic carbon (Stetten et al., 2015). This assumes that the composition of sediment within the flow is broadly similar to that buried in flow deposits. Oxidization of organic carbon during burial of these sediments will result in the amount of organic carbon within the flow being underestimated. This calculation results in an annual flux of 0.5 to 1.1 Mt/year of predominantly terrestrial organic carbon through the canyon. This is 1.2 to 2.6% of the estimated 43 Mt of terrestrial organic carbon that is buried globally in the oceans each year (Schlünz and Schneider, 2000).

2.8 Congo Canyon turbidity current triggering

To better understand potential triggers, the timing of turbidity currents in the Congo Canyon was compared to environmental variables such as river discharge and wave heights. We were unable to carry out robust statistical analysis of turbidity current triggering due to the small number (six events) of observed turbidity currents. Our analysis of how these flows were triggered therefore remains qualitative.

Turbidity current triggering has previously been linked with sediment-laden river flood water discharge at the coast (Mulder et al., 2003). To test this relationship, turbidity current timing in the Congo Canyon was compared to river discharge data from the Kinshasa gauging station (4.3˚S, 15.3˚E). This gauging station is located ~450 km upstream from the mouth of the Congo River, and it is the closest available station.

Large waves, internal tides, and standing waves are thought to be able to trigger turbidity currents in submarine canyons (Inman et al., 1976; Komar, 1977; Paull et al, 2002). Ocean buoys can provide an excellent record of these variables, but their global coverage is spatially variable and these data are not always freely available. For the Congo Canyon, we therefore used global model data. Six-hour estimates of significant wave height (in meters), mean wave period (in seconds), mean wave direction (in degrees), and surface pressure (in pascal) were obtained from the ERA-Interim global atmospheric reanalysis model produced by the European Centre for Medium-Range Weather Forecasts (ECMWF) (Dee et al., 2011) at the head of the Congo Canyon (Figure 2.16). The data were gridded at a resolution of 0.125˚. The data revealed no clear relationship between ocean wave or surface pressure characteristics and turbidity current frequency (Figure 2.16). Turbidity current occurrence does not coincide with peaks in significant wave height, nor do magnitudes vary to the extent that they have when previously linked to turbidity current triggering (Patterson, 1974; Pope et al., 2017). It is therefore unlikely that the measured turbidity currents were triggered either directly by surface waves or after a delay as a consequence of wave action on the seafloor.

Earthquake records during the period in which ADCPs were deployed were obtained from the U.S. Geological Survey Advanced National Seismic System Comprehensive Earthquake Catalog (ComCat; https://earthquake.usgs.gov/earthquakes/search/). The timing of earthquakes (Mw > 2.5) within 300 km of the head of the Congo Canyon was compared to known turbidity current arrival times.

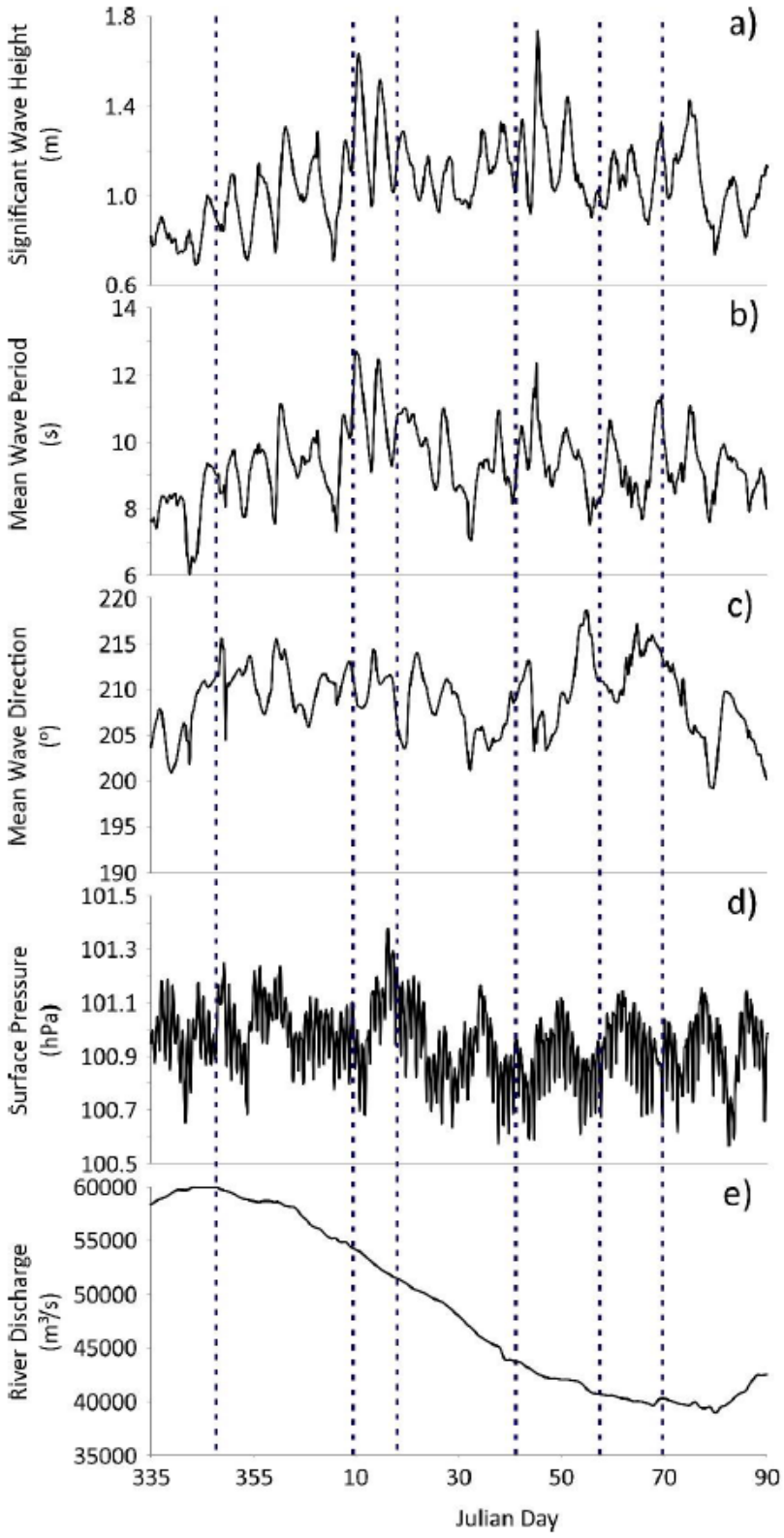

Figure 2.16. Comparison of turbidity current arrival times with possible triggering factors in the Congo Canyon. Turbidity current arrival times indicated by dashed lines. (A) Significant wave height. **(B)** Mean wave period. **(C)** Mean wave direction. **(D)** Surface pressure. **(E)** River discharge.

Chapter 3:

Newly recognised turbidity current structure can explain prolonged flushing of submarine canyons

This chapter is based upon text published in Science Advances (http://advances.sciencemag.org/content/3/10/e1700200 - doi: 10.1126/sciadv.1700200). The published 'Material and methods' and 'Supporting Information' sections have been relocated into chapter 2 of this thesis. The aim of the adjustments is to maintain the flow of the main text through keeping the extensive 'Material and methodology' and 'Supporting Information' sections separate.

Maria Azpiroz-Zabala[1,2], Matthieu J.B. Cartigny[3], Peter J. Talling[3], Daniel R. Parsons[4], Esther J. Sumner[2], Michael A. Clare[1], Stephen M. Simmons[4], Cortis Cooper[5], and Ed Pope[6]

[1] National Oceanography Centre, University of Southampton Waterfront Campus, European Way, Southampton SO14 3ZH, UK.

[2] National Oceanography Centre Southampton, University of Southampton, Southampton SO14 3ZH, UK.

[3] Departments of Earth Sciences and Geography, University of Durham, Durham DH1 3LE, UK.

[4] School of Environmental Sciences, University of Hull, Cottingham Road, Hull, HU6 7RX, UK.

[5] formerly at Chevron Energy Technology Company, 6001 Bollinger Canyon Road, San Ramon, CA 94583, USA.

[6] Department of Geography, Durham University, South Road, Durham, DH1 3LE, UK.

Data collection was led by Cooper. The majority of data analysis was conducted by Azpiroz-Zabala with assistance from Cartigny. The methodology for using backscatter data to infer sediment concentration was developed by Parsons and Simmons. Triggering data were investigated by Clare and Pope. The final manuscript has benefitted from contributions from all co-authors along with comments from an editor and two anonymous reviewers.

Abstract

Seabed-hugging flows called turbidity currents are the volumetrically most important process transporting sediment across our planet and form its largest sediment accumulations. We seek to understand the internal structure and behavior of turbidity currents by reanalyzing the most detailed direct measurements yet of velocities and densities within oceanic turbidity currents, obtained from weeklong flows in the Congo Canyon. We provide a new model for turbidity current structure that can explain why these are far more prolonged than all previously monitored oceanic turbidity currents, which lasted for only hours or minutes at other locations. The observed Congo Canyon flows consist of a short-lived zone of fast and dense fluid at their front, which outruns the slower moving body of the flow. We propose that the sustained duration of these turbidity currents results from flow stretching and that this stretching is characteristic of mud-rich turbidity current systems. The lack of stretching in previously monitored flows is attributed to coarser sediment that settles out from the body more rapidly. These prolonged seafloor flows rival the discharge of the Congo River and carry ~2% of the terrestrial organic carbon buried globally in the oceans each year through a single submarine canyon. Thus, this new structure explains sustained flushing of globally important amounts of sediment, organic carbon, nutrients, and fresh water into the deep ocean.

3.1 Introduction

Turbidity currents are seabed-hugging flows driven downslope by the excess weight of suspended sediment. These flows form the largest sediment accumulations on Earth (Bouma et al., 2012). Only terrestrial river systems carry similar volumes of sediment (Talling et al., 2013), although one turbidity current can sometimes transport more sediment than the annual global flux from all

rivers combined (Milliman and Syvitski, 1992; Talling et al., 2007). Understanding turbidity current structure and duration is important for mitigating the considerable hazard that they pose to expensive seafloor infrastructure, such as oil and gas pipelines (Cooper et al., 2013; 2016), or the network of seafloor cables that now carries >95% of Internet and other global data traffic (Carter et al., 2014). Turbidity currents play a significant role in global carbon cycling and sequestration (Galy et al., 2007; Schlünz and Schneider, 2000), supply important nutrients to deep-sea ecosystems (Canals et al., 2006), and ventilate the deep ocean with fresh water (Kao et al., 2010), whereas their deposits (called turbidites) host major petroleum reservoirs worldwide (Nilsen et al., 2008) and contain important archives of Earth's geological past (Nilsen et al., 2008).

In contrast to many millions of direct observations of velocity and suspended sediment concentration in rivers (Milliman and Syvitski, 1992), there are remarkably few direct measurements from turbidity currents (Talling et al., 2013). These submarine flows are notoriously difficult to monitor due to their relatively inaccessible location, often unpredictable occurrence, and ability to severely damage instruments placed in their path (Talling et al., 2013). This paucity of direct observations has meant that previous models for turbidity currents were based mainly on laboratory-scale experiments or inferred from deposited sediment layers. To make a step change in understanding of turbidity currents and of their wider impacts, there is a compelling need to measure key parameters within full-scale events. In particular, we need to understand the internal structure of these flows and how this structure then determines the flow evolution and duration.

This study is based on the highest resolution measurements (made every 5 s) yet collected within an oceanic turbidity current (Cooper et al., 2013; 2016). Initially shown by Cooper et al. (2013; 2016), these measurements were collected in the Congo Canyon (Cooper et al., 2013; 2016) at a water depth of 2 km using downward-looking acoustic Doppler current profilers (ADCPs) suspended 66 to 85 m above the seafloor (Figure 3.1). Flows were measured at a single site from December 2009 to March 2010 (Cooper et al., 2013), as well as at an additional site from January to March 2013 (Figure 3.1, B and C) (Cooper et al., 2016).

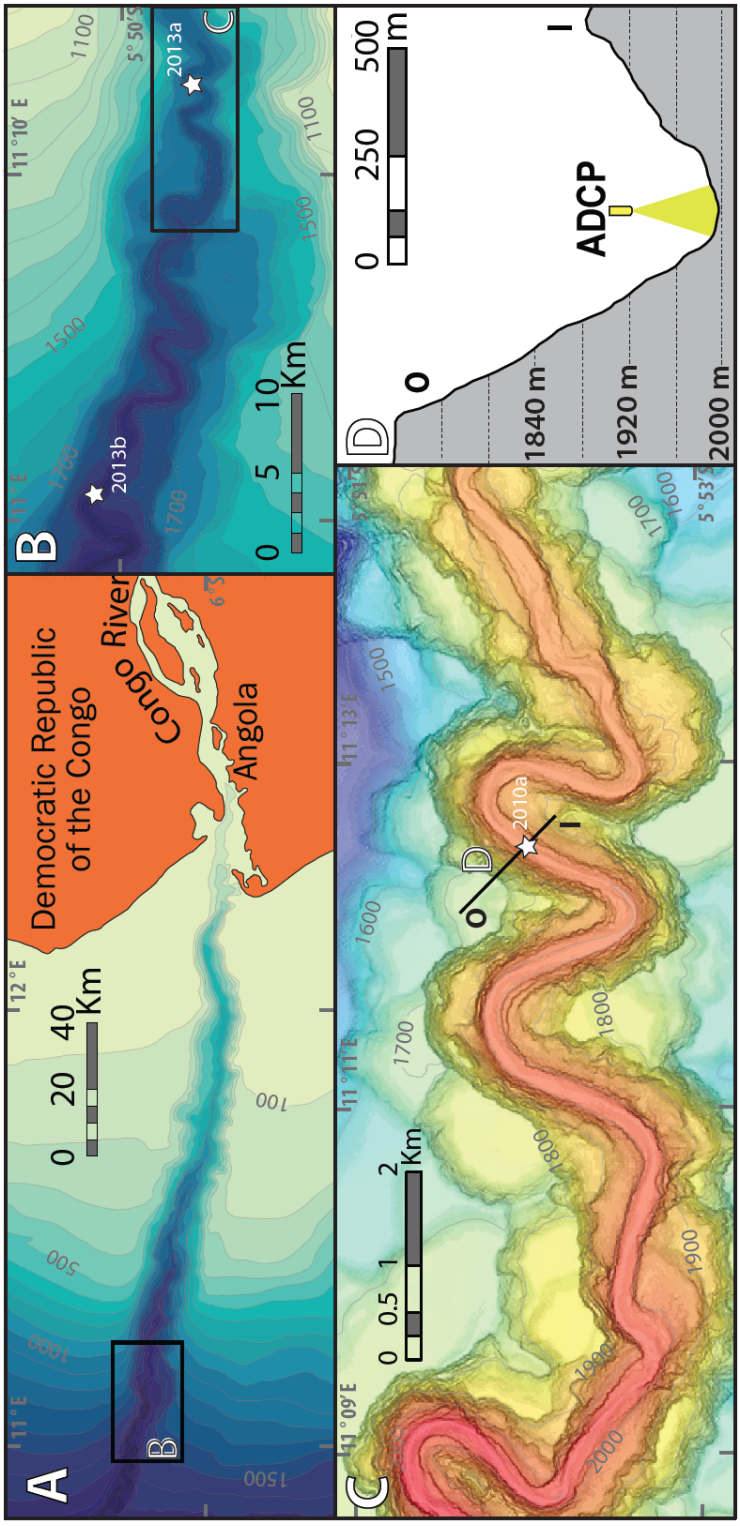

Figure 3.1. Mooring locations in the Congo Canyon. (A) Map of the Congo Canyon showing study area (rectangle), with bathymetric contours in meters. **(B)** Map showing the location of the two moorings deployed in 2013 (Babonneau, 2002; Cooper et al., 2016). **(C)** Map showing location of 2010 mooring (Cooper et al., 2013). **(D)** Cross-canyon profile showing ADCP suspended 85 m above the canyon floor. Location of cross section indicated in (C).

A major surprise from both the 2009–2010 and 2013 measurements was that individual turbidity currents lasted for almost a week (Figure 3.2 and Table 3.1), rather than hours or minutes as in all previous oceanic measurements from shallower water (Figure 3.2) (Talling et al., 2013). Here, we present a new model of turbidity current structure that explains these prolonged flow durations. This model is based on a reanalysis of the ADCP data set collected by Cooper et al. (Cooper et al., 2013; 2016), including the application of a novel acoustic inversion technique that provides us with a first insight into the distribution of sediment within individual flows (see chapter 2).

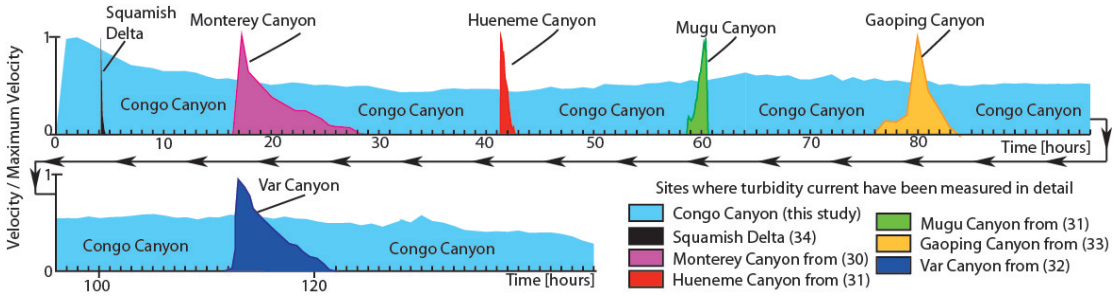

Figure 3.2. Turbidity currents that flush the Congo Canyon are far more prolonged than any previously monitored oceanic turbidity current. This figure compares the duration of the Congo Canyon flows studied here and oceanic turbidity currents that have been monitored previously using ADCPs in other shallower water locations (Hughes Clarke, 2016; Khripounoff et al., 2012; Liu et al., 2012; Xu et al., 2004; Xu et al., 2010).

Our first aim is to document the internal structure of these turbidity currents, which is important because it determines how turbidity currents behave and evolve over time and space. Our second aim is to understand why these flows are so sustained. We show how their internal structure can explain their prolonged duration. Our third aim is to understand why the duration and character of these Congo Canyon turbidity currents differ from all previous measured oceanic turbidity currents and most laboratory experiments. We conclude by outlining the wider implications of this sustained flushing of submarine canyons for geohazards, organic carbon fluxes, and benthic ecosystems.

3.2 Results

Turbidity currents were active in the Congo Canyon for ~33% of the time during our 2009–2010 deployment period. Six prolonged flows dominate the 2009–2010 data set (Figure 3.3A). The average flow lasted for 6.7 days, had a thickness of 62 m, and reached peak velocities of 1.5 m/s (Table 3.1). The highest velocities occurred at the front of the flow and are associated with maximum sediment concentrations (Figure 3.3, B to D) of up to several tens of grams per liter (Table 3.1 and Figure 3.3D). The velocity profiles over the remaining part of the flow showed considerable variation in their shape (Figure 3.3, E to I), with peak velocities of around 0.8 to 1 m/s occurring between 6 and 14 m above the seafloor (Table 3.1). Average sediment concentrations are consistently about 0.02% by volume (Table 3.1). Peak sediment discharges of ~6,000 kg/s (Table 3.1) exceed the sediment discharges of the Congo River and rival those of the Mississippi River (Milliman and Syvitski, 1992). On average, a single turbidity current transports 2.3 km^2 of water, ~1.1 to 3.8 Mt (million metric tons) of sediment, and ~0.03 to 0.19 Mt of organic carbon into the deep sea. Ranges in the amount of sediment and organic carbon (Table 3.1) reflect variations in the grain size and organic carbon content assumed (see chapter 2).

FLOW	**1**	**2**	**3**	**4**	**5**	**6**	**Mean**
Duration [days]	10.1	5.5	5.2	6.6	6.3	6.3	6.7
Maximum thickness [m]	53	57	48	69	77	68	62
Maximum ADCP velocity [m/s]	1.2	1.2	1	2.4	1.9	1.4	1.5
Average ADCP velocity [m/s]	0.4	0.4	0.3	0.7	0.5	0.4	0.5
Front propagation velocity [m/s]	0.8	0.8	0.7	1.6	1.5	1.0	1.1
Average height of maximum velocity above the bed [m]	6.8	6.9	5.8	14.2	11.8	10.0	9.3
Time of maximum velocity after arrival of the flow front [min]	25	34	100	8	25	25	36
Average sediment concentration [$\%_{vol}$]*	0.018	0.020	0.020	0.023	0.020	0.017	0.020

Peak sediment concentration [$\%_{vol}$]*	0.076	0.047	0.086	0.163	0.168	0.155	0.116
Maximum discharge [10^3 m^3/s]	4.6	4.9	2.7	14.9	16.3	10.4	9.0
Average discharge [10^3 m^3/s]	2.4	2.8	1.6	6.9	6.0	3.7	3.9
Maximum sediment discharge [10^3 kg/s]*	3.1	2.7	2.0	13.2	9.0	6.1	6.0
Average sediment discharge [10^3 kg/s]*	1.2	1.5	8.8	4.3	3.2	1.7	2.1
Water volume displaced [km^3]	2.1	1.4	0.7	4.0	3.3	2.1	2.3
Sediment volume displaced [Mton]*	1.0	0.7	0.4	2.5	1.7	0.9	1.2
Organic carbon displaced [Mton] †	0.04	0.03	0.02	0.10	0.07	0.04	0.05

*Assuming a uniform grain size of 4.23 μm for inverting ADCP backscatter to sediment concentration (see chapter 2). †Assuming an average carbon content of 3 to 5% weight, as measured within turbidity current deposits on the Congo Fan (see chapter 2) (Stetten et al., 2015).

Table 3.1. Summary of flow properties of the 2010 deployment (numbering corresponds to Figure 3.3A).

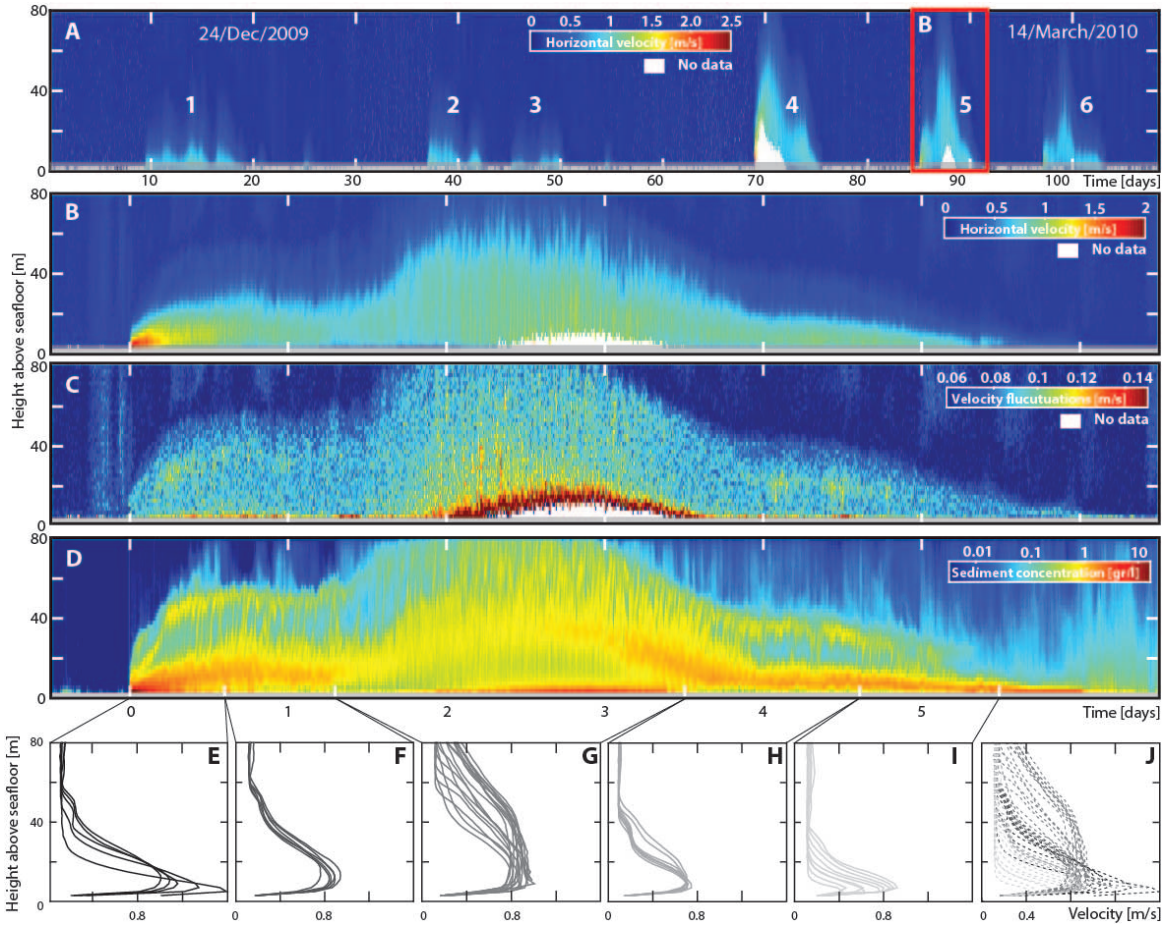

Figure 3.3. Turbidity current structure and duration from ADCP measurements at the 2009–2010 mooring site. (A) Full velocity time series for 3 months in 2009–2010 (Cooper et al., 2013), showing that flows are active for ~33% of the time. Single flow in (B) to (D) is shown by the red box. **(B)** Horizontal velocity (30-min averages). **(C)** Intensity of large-scale velocity fluctuations, defined as the root mean square of differences between individual velocity measurements and 1-min averages. **(D)** Sediment concentrations inverted from 300- and 75-kHz ADCP acoustic backscatter (see chapter 2, and figures 2.2 and 2.7 to 2.13). This analysis assumes that the flow contains a single grain size, and variations in grain size may cause artefacts such as higher concentrations above lower concentrations. **(E to I)** Velocity profiles for different temporal parts of the flow. **(J)** All velocity profiles combined in one plot.

The internal structure of these turbidity currents in the Congo Canyon differs from that seen in previous experiments and measurements. On the basis of laboratory-scale experiments, previous models for sustained turbidity currents comprise an unsteady flow front (the head), followed by a steadier period of flow (the body) that finally wanes (the tail) (Figure 3.4A) (Kneller and Buckee, 2000).

The head is slower and thicker than the body because it has to displace surrounding water. Thus, the faster-moving body feeds the head with sediment-laden fluid (Figure 3.4A) (Cartigny et al., 2013; Kneller and Buckee, 2000; McCaffrey et al., 2003; Middleton, 1993). The highest sediment concentrations occur in the head and lower part of the body; concentration, velocity, and flow thickness then decline within the tail of the flow (Figure 3.4A) (Kneller and Buckee, 2000; McCaffrey et al., 2003). The basic structure and hence behavior of turbidity currents in the Congo Canyon differ from these laboratory flows, and all previous measurements of surge-type oceanic turbidity currents (Figure 3.2), in two important regards.

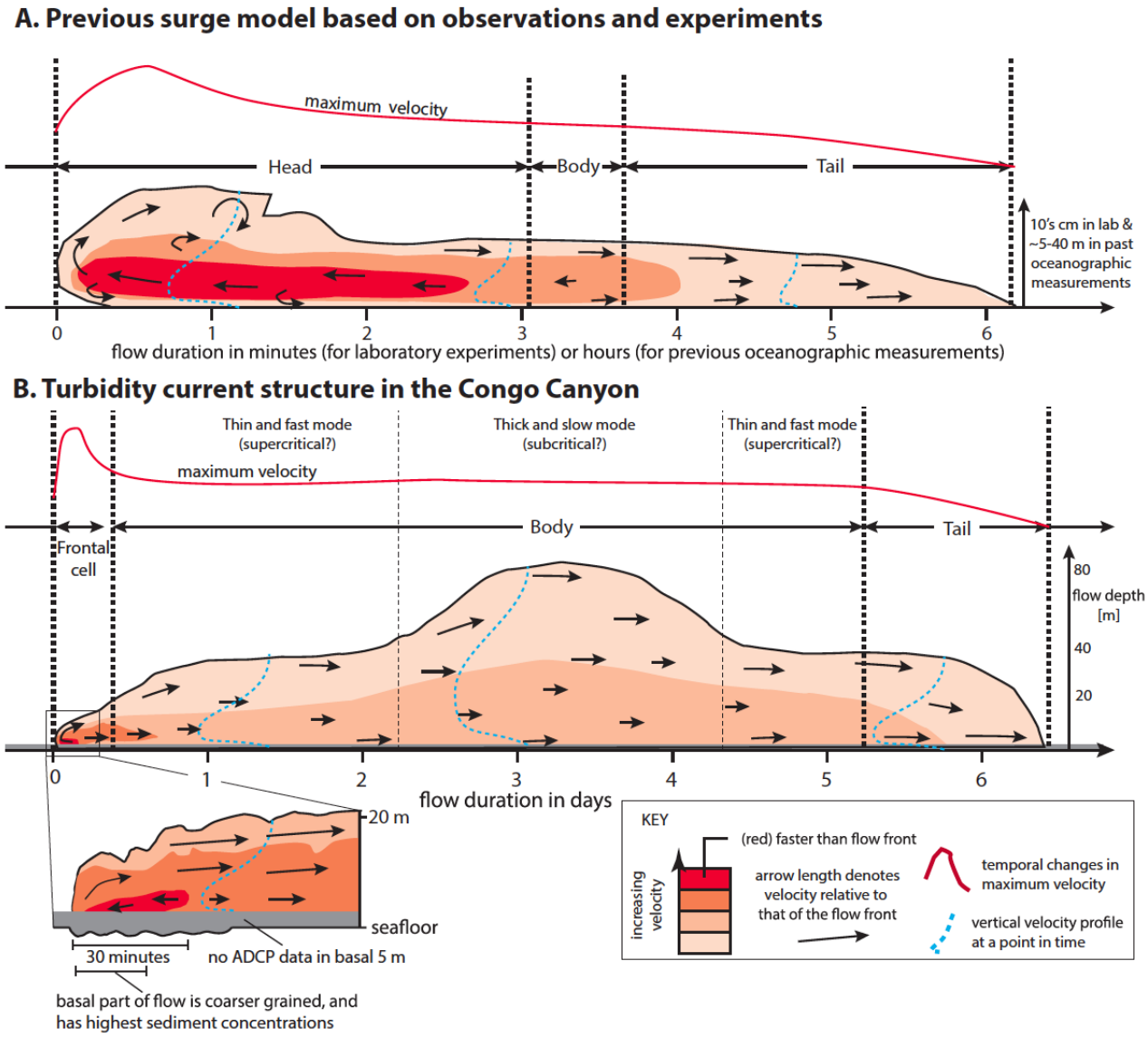

Figure 3.4. Turbidity current structure in laboratory experiments and in the Congo Canyon. Structure is shown by temporal changes in velocity measured at one spatial position, with red solid line denoting highest flow velocities.

(A) Typical laboratory experiment with a finite-volume (surge-like) release (Cartigny et al., 2013; Kneller and Buckee, 2000; McCaffrey et al., 2003; Middleton, 1993) or previous oceanographic measurements (Hughes Clarke, 2016; Khripounoff et al., 2012; Liu et al., 2012; Xu et al., 2004; Xu et al., 2010); more sustained input would produce a better developed body. Arrows denote relative movement of sediment-laden fluid with respect to the flow front, with flow front velocity thus subtracted from measured velocities. The arrows show whether the body feeds the head. Temporal changes in maximum flow velocity are shown by red lines, and velocity profile shapes are shown by blue dotted lines. **(B)** Turbidity current structure in the Congo Canyon. Boundary between head and body is determined by the initiation of stable velocity values of the flow, which are maintained in the body. Boundary between body and tail is determined by a decrease in velocity values of the flow, which finalises with the flow extinction.

The first difference is that the Congo turbidity currents are composed of a short-lived zone (which we call the “frontal-cell”) of faster, dense, and coarse-grained flow (Figures 3.3, 3.4B, and 3.5). Our ADCP backscatter inversion indicates that coarsest grains and highest concentrations are found within a few meters of the bed, close to the flow front (Figures 3.5.C and 3.5D). This frontal-cell runs away from the trailing body, unlike most laboratory experiments in which the body is faster than the head (Cartigny et al., 2013; Kneller and Buckee, 2000; McCaffrey et al., 2003). The frontal-cell is thinner than the trailing body, and the velocity data show that the body is not feeding sediment-laden fluid into the frontal-cell (Figure 3.3B). Instead, in our observations, the frontal-cell sheds sediment-laden fluid into the trailing body (Figures 3.3B and 3.4B). This implies that the frontal-cell must continuously erode new sediment to replenish the sediment lost into the trailing body, making erosion of the canyon floor an important source of sediment. Calculations of bed shear stresses indicate that the frontal-cell can erode and incorporate sediment from the canyon floor, thus becoming self-sustaining (Figure 2.14) (Bagnold, 1962). Shear stresses beneath the trailing body are lower but still sufficient to suspend sand grains of up to ~200 μm (Figure 2.14).

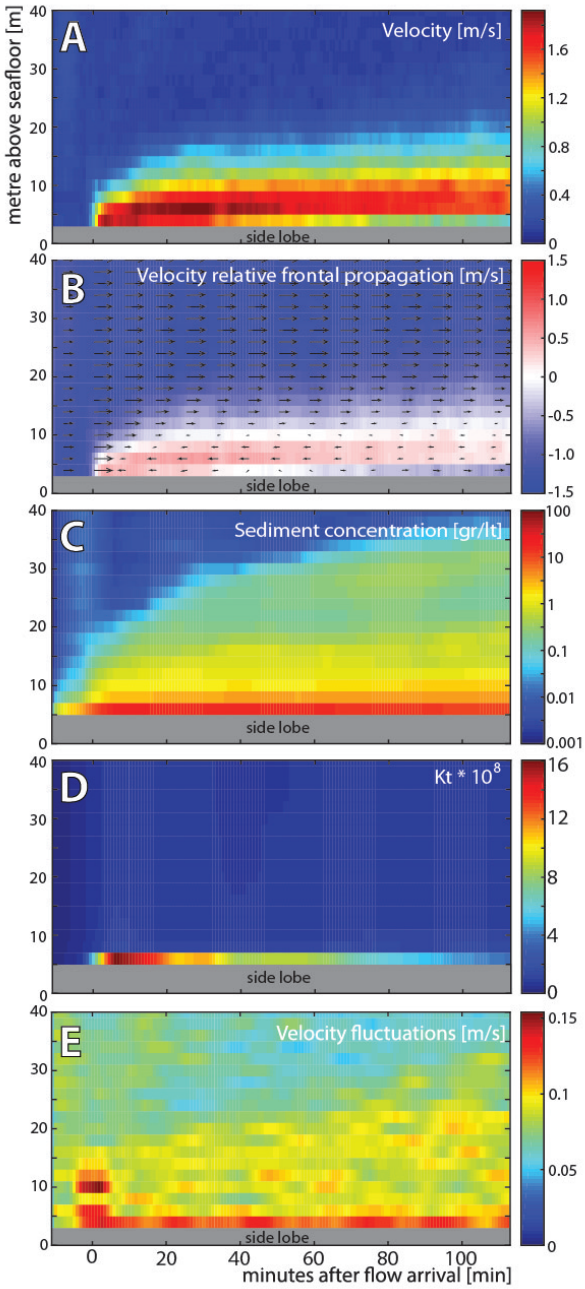

Figure 3.5. Structure of the frontal-cell during the first 120 min of the flow. **(A)** Horizontal flow velocity. Side lobe interference area (see chapter 2) is covered by the gray box. **(B)** Velocity relative to the flow front propagation velocity (which is here fixed at 1.35 m/s). **(C)** Sediment concentration as derived from the acoustic inversion. **(D)** Variation of the calibration constant (Kt) is used to indicate either grain size variation or higher sediment concentrations (see chapter 2). (E) Velocity fluctuations.

We introduce the new terms, frontal-cell and trailing body, for the following reasons. Sequeiros et al. (2009) used the term "head" for the self-sustaining frontal zone of a turbidity current. However, in the vast majority of previous

studies, the head is not self-sustaining and has to be sustained by transfer of sediment-laden fluid from the body. This is not the case here. To prevent confusion, we use the term frontal-cell for a self-sustaining head. Our use of frontal-cell also emphasizes the observed circulation pattern (shown by arrows in Figure 3.4B) in which fluid moves toward the flow front at the height of the velocity maximum, before being deflected upward and returning back toward the body in the uppermost and lowermost parts of the frontal-cell.

The second important difference is that the Congo Canyon flows are remarkably prolonged, with velocities of 0.8 to 1 m/s sustained for almost a week before dropping off in the tail of the flow (Figs. 3.2 and 3.3). This is in contrast to previous oceanic measurements in which an initial velocity peak is followed by a continuous decrease in velocity (Figure 3.2). We propose a new model in which sustained flow is achieved because the frontal-cell outruns and feeds the trailing body, causing the flow to stretch (Figure 3.4B). For example, if the flow front travels at 1.2 m/s, and the tail moves at 0.25 m/s, and both travel 170 km along the sinuous canyon, then the tail will arrive 6.2 days after the flow front at our measurement site. The amount of stretching depends on the relative values of the flow front and tail velocities, and reasonable values of these two velocities suggest stretching on the order of days (Figure 3.6). Flow stretching has the potential to generate ever more continuous turbidity currents further from the source, because slower moving events can be overtaken by faster moving ones, thus merging into a single longer event. However, previous studies of the deepest (>3.4 km) parts of the Congo Canyon have observed powerful but less frequent flows (Vangriesheim et al., 2009), suggesting that some flows die out in the lower canyon.

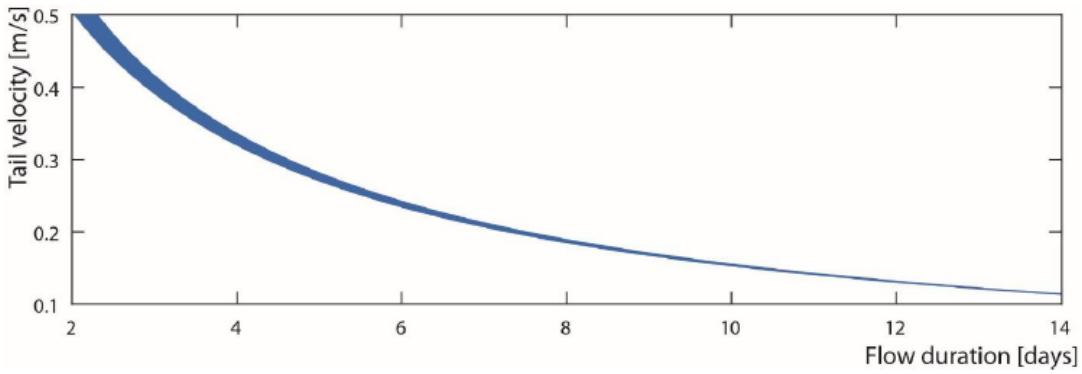

Figure 3.6.. Increase in flow duration caused by flow stretching, which is due to a difference in the speed of the front and tail of the flow. The plot illustrates how variations in tail speed will affect the calculated degree of flow stretching. A runout distance of 170 km is assumed, together with

frontal speeds of 1.2 m/s to 1.5 m/s. The width of blue line reflects that range of front speeds.

This stretching model has then been tested using a second ADCP data set collected from January to March 2013 (Cooper et al., 2016). The duration of these 2013 flows was compared at two sites along the Congo Canyon that are 22 km apart (Figure 3.1B) (Cooper et al., 2016). Flow durations at the two moorings are shown in Figure 3.7A and Table 3.2. ADCP measurements in the lowermost 18 m of these flows are lacking due to reflections from the canyon wall. This is because the January-March (2013) moorings were located close to the canyon wall, although still within the flat canyon floor (Figure 2.3). Nonetheless, at 18 m above the seafloor, the duration of these 2013 flows increased substantially in a down-canyon direction by an average of 0.74 ± 0.6 days (Figure 3.7A and Table 3.2). We note that the 2013 flows tend to be thicker at the downstream mooring, and this may also partly explain their longer duration at the downstream site (Table 3.2). However, this significant increase in measured flow durations between the two sites in 2013 generally supports the hypothesis that these flows stretched as they moved down-canyon.

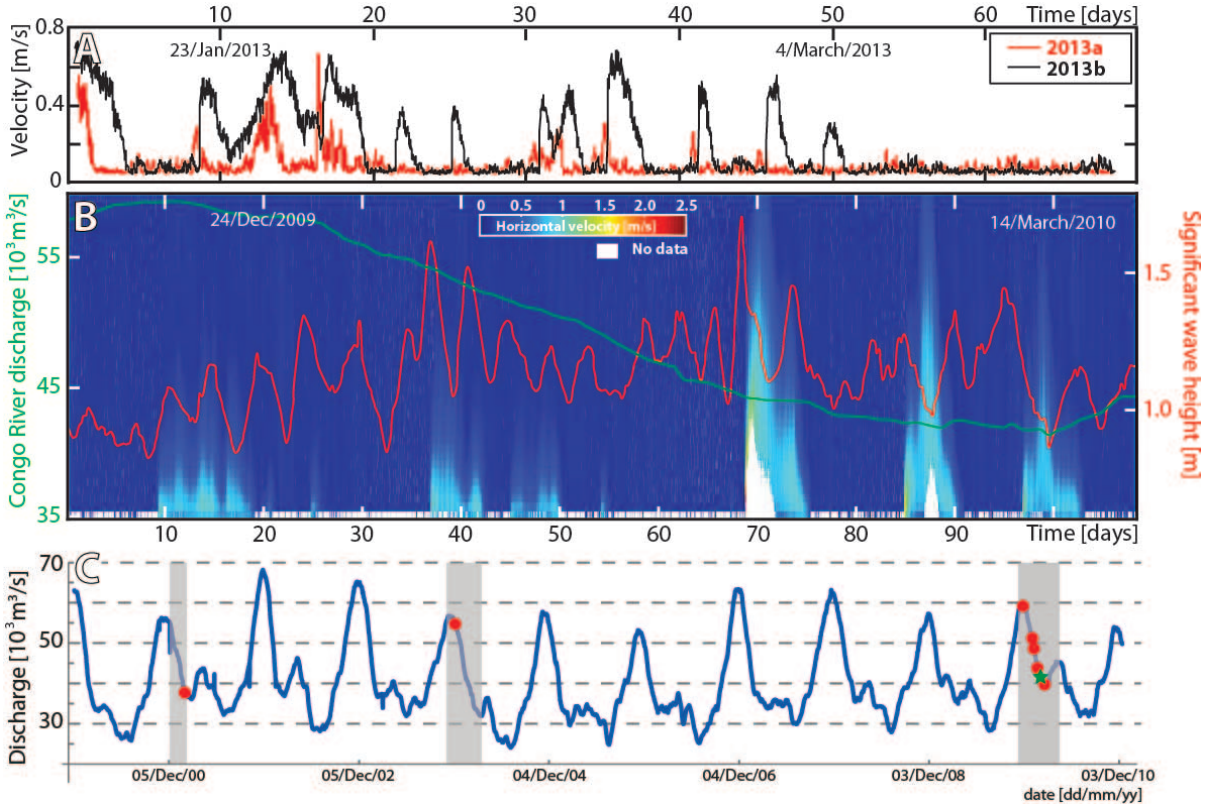

Figure 3.7. Timing and triggers of turbidity currents. (A) Flow velocities measured at 18 m above the seafloor by ADCPs at two mooring sites in 2013. Site

2013a is located 22 km up-canyon from site 2013b (Figure 3.1B) (Cooper et al., 2016). Difference in flow duration between site 2013a and 2013b might be due to the location of the mooring in relation to the canyon walls, i.e. the section of the flow monitored by ADCPs. **(B)** Turbidity currents of the 2010 deployment plotted against two potential triggers: significant wave height in red and Congo River discharge at the Kinshasa gauging station in green (see chapter 2). **(C)** Plot of changes in Congo River discharge (blue line), periods when measurement instruments were present in the canyon (gray bars) (Cooper et al., 2013; Khripounoff et al., 2003; Vangriesheim et al., 2009;), and timing of turbidity currents (red dots). The green star is the turbidity current shown in Figure 3.3.

Event No.	2013a* (up-canyon)			2013b Site (down-canyon)			Difference in flow duration (i.e. stretching) (days)
	Duration (days)	Elevation (m)	Peak speed at 18 m (m/s)	Duration (days)	Elevation (m)	Peak speed at 18 m (m/s)	
1	2.08	42.1	0.74	3.47	62.1	0.95	1.39
2	1.60	24.1	0.50	2.78	42.1	0.73	1.18
3	3.40	28.1	0.78	5.15	62.1	0.81	1.75
4	2.64	30.1	0.84	2.88	60.1	0.79	0.15
5	1.04	14.1	0.33	0.92	32.1	0.54	0.12
6	1.25	16.1	0.44	1.72	34.1	0.64	0.47
7	1.60	22.1	0.69	2.61	56.1	0.86	1.01
8	0.83	14.1	0.40	1.08	36.1	0.63	0.25
9	1.39	14.1	0.33	1.69	38.1	0.61	0.30
Mean ± standard deviation	1.76 ± 0.82	22.8 ± 9.54	0.56 ± 0.20	2.48 ± 1.32	47.0 ± 12.8	0.73 ± 0.13	0.74 ± 0.61

* The 2013a site is located 22 km up-canyon from the 2013b site.

Table 3.2. Flow durations, thicknesses, and peak velocity measured at heights in excess of 18 m above the bed in 2013.

3.3 Discussion

We first discuss whether the prolonged turbidity currents of the Congo Canyon result from sustained sediment sources or from internal flow stretching. We then seek to understand why these turbidity currents in the Congo Canyon differ significantly from most (but not all) laboratory experiments, and all previous measurements from full-scale oceanic flows. Finally, we outline the wider

implications of these sustained turbidity currents for carbon burial and geohazards.

3.3.1 How were these flows triggered?

It is important to determine whether the prolonged duration of these flows results from a sustained initial source of sediment, as opposed to stretching of the flow as it moves down-canyon. Several potential triggers can be eliminated for these Congo Canyon flows (also see chapter 2). The flows were not triggered by earthquakes, because no significant earthquakes [moment magnitude (Mw) > 2.5] occurred within 300 km of the canyon during our measurement period (ComCat website). There is also no clear correlation between wave height and timing of the flows (Figure 3.7B).

Prolonged turbidity currents have previously been attributed to hyperpycnal river floods that plunge to form a turbidity current moving along the seafloor (Mulder et al., 2003). However, the turbidity currents described here did not coincide with Congo River floods (Figure 3.7B). In addition, the Congo River is characterized by particularly low sediment concentrations that would not allow the river water to plunge beneath the saline ocean water (Mulder and Syvitski, 1995; Mulder et al., 2003; Parsons et al., 2001). However, previous cable breaks in the Congo Canyon show that powerful turbidity currents are more common during the months in which the Congo River discharge is elevated (Heezen et al., 1964). This association suggests a connection between river discharge and turbidity current frequency, even if the turbidity currents are not formed directly by plunging river water. For example, it is possible that increased river discharge produces more rapid sediment deposition or large-scale switching of the lowermost branches of the braided river mouth, which may lead to more unstable slopes (Clare et al., 2016; Heezen et al., 1964).

It has been previously shown that sustained turbidity currents may be initiated by prolonged slope failures called breaches. These sustained slope failures tend to occur in close-packed sands, which generate negative pore pressures once disturbed, resulting in a progressively up-slope migrating head scarp (van den Berg et al., 2002; Mastbergen and van den Berg, 2003). However, previously observed breaches only lasted for up to several hours, rather than several days, as would be needed to trigger these weeklong flows in the Congo Canyon. It

cannot be ruled out that more sustained breaching may occur in deep water, or prolonged slope failures may be triggered by other (as yet unknown) processes. However, it appears that sustained turbidity currents are unlikely to result from sustained sources such as plunging river floods or breaching. We submit that sustained turbidity currents may develop from a short-lived sediment source due to flow stretching, as a result of an erosive frontal-cell that outpaces and feeds an expanding trailing body.

3.3.2 Comparison with previous laboratory experiments

As outlined in Results, the structure of these turbidity currents in the Congo Canyon differs significantly from many laboratory-scale flows (Figure 3.4). For example, in short-lived experimental flows (termed surges), the head does not outrun the body, and the body is rather poorly developed (Figure 3.4A). This may be related to an inability for these relatively slow-moving and weak experimental flows to entrain sediment from the bed (de Leeuw et al., 2016). Entrainment of seafloor sediment is needed to develop a self-sustaining head (that is, a frontal-cell) such that this initial self-sustaining part of the flow can both push aside the surrounding seawater and outrun the body. If the head has a similar or lower density than the body, then the body will tend to be faster than the head because it benefits from being in the lee of the head.

However, the laboratory experiments of Sequeiros et al. (2009) show how the head of the flow may entrain sediment, thereby making the head self-sustaining. In these experiments, the head is seen to become denser and faster as it moves downslope, thereby meeting the criteria of self-acceleration (Parker et al., 1986). Sequeiros et al. (2009) did not explicitly discuss the implications of a self-sustaining head for flow stretching, nor did their experiments create a prolonged trailing body. However, assuming that sediment in the trailing body does not settle out, a self-sustaining head will tend to run away from the body and thus stretch the flow.

3.3.3 Comparison with previous measured oceanic turbidity currents?

These flows in the Congo Canyon have significantly different durations and structures from previously measured oceanic turbidity currents (Figure 3.2). We

are aware of seven other shallower water locations where vertical profiles of velocity or concentration (that is, backscatter) have been measured in oceanic turbidity currents, in each case using ADCPs (Hughes Clarke, 2016; Khripounoff et al., 2012; Liu et al., 2012; Xu et al., 2004; Xu et al., 2010). In some cases, the ADCP velocity profiles were measured only every hour, and the flows were only a few hours in duration such that the frontal part of the event was probably not captured.

Turbidity currents in these other locations lasted for between a few minutes and ~10 hours (Figure 3.2). These flows had a relatively consistent structure in which the maximum flow velocity occurred almost immediately behind the flow front, which was followed by a continuous decline in velocity (Figure 3.2). This structure is similar to that seen in surge-like laboratory experiments (Figure 3.4A). The first part of this structure also broadly resembles the frontal-cell within the Congo Canyon flows. However, turbidity currents at these other sites lack the elongated body that trails behind the frontal-cell in the Congo Canyon flows. Studies of flows in Monterey Canyon provide measurements from multiple locations that document flow durations at several points in the canyon (Hughes Clarke, 2016; Xu et al., 2010). These flows are noteworthy because they did not stretch. Their duration initially decreased from 8 to 6 hours and then remained at 6 hours (Xu et al., 2004).

Here, we propose that flows in these other locations also comprise a fast-moving frontal-cell (Figure 3.3B), which is erosive and thus self-sustaining. The frontal-cell also sheds sediment-laden fluid into the trailing flow. However, in locations other than the Congo Canyon, we propose that sediment shed into the trailing body tends to settle out rapidly, thereby counteracting flow stretching. If this is the case, flow stretching will be more pronounced in finer-grained turbidity currents in which sediment will settle more slowly.

This hypothesis is consistent with available field data indicating that flows in the Congo Canyon are significantly muddier than in the other seven locations. For example, deposits on the floor of Monterey Canyon typically comprise relatively coarse sand (Paull et al., 2010), whereas deposits on the canyon floor near our mooring sites in Congo Canyon consist of laminated sediments mainly composed of clay and silt (Figure 2.12). Deposits found on the lobe at the termination of the Congo canyon-channel system are also relatively fine-grained (Dennielou et al., 2017).

We therefore suggest that mud- and sand-rich turbidity currents tend to have different flow structures and durations. Mud-rich flows will have much better developed bodies, which may become self-sustaining and stretch. Sediment tends to settle out from the body of sand-rich flows so that their body is less well developed, and they primarily consist of a frontal-cell. Rapid settling from the body and tail of the sand-rich flows substantially reduces the degree to which these flows stretch. Other parameters, such as bed shear stress, turbulence and the ratio of sands and mud, might also influence the structure and duration of the flows.

3.3.4 Wider implications of sustained turbidity currents

This study shows how flow stretching can generate prolonged and powerful turbidity currents, which flushed the Congo Canyon for ~33% of the 120-day measuring window in 2009–2010 (Figure 3.3A). The wider implications of these prolonged flows of sediment and organic carbon into the deep ocean are profound. The Congo Canyon is directly connected to the Congo River, which drains about 2.2% of the Earth's land surface, mostly covered by tropical vegetation. The total organic carbon transport through the submarine canyon can be estimated by assuming that, during 33% (Figure 3.3A) of the time, turbidity currents are transporting an average of 2,100 kg of sediment per second (Table 3.1) that comprises 3 to 5% of organic carbon (Stetten et al., 2015). This transport results in the Congo Canyon carrying around 1.2 to 2.6% of the terrestrial organic carbon buried annually in the world's oceans (Schlünz and Schneider, 2000). These sustained turbidity currents favour transfer of organic carbon into the deep sea (Galy et al., 2007), and they help to explain widespread oxygen deficits linked to carbon remineralization (Stetten et al., 2015). Sustained input and degradation of large amounts of organic matter have strongly affected ecosystem functioning in the deep sea. Unusual seafloor communities have recently been described across the distal Congo Fan, resembling those based on chemosynthesis at cold seep sites (Congolobe group, 2017).

The powerful and sustained nature of the turbidity currents described here illustrates the challenge of mitigating hazards to important seafloor infrastructure, which underpins global telecommunications and energy supplies (Carter et al., 2014; Cooper et al., 2013; 2016; Smith, 2013). Previous attempts to mitigate this hazard include work to reroute a major gas pipeline beneath the

Congo Canyon, using directional sub-seafloor drilling (Smith, 2013). Here, we provide new insights into the duration, velocity, and density structure of turbidity currents, which are crucial for determining impact forces on seabed infrastructure. We show that subsea cables and pipelines must withstand powerful flows with discharges comparable to the Congo River or Mississippi River that persist for nearly a week rather than for only hours or minutes.

Chapter 4:

A general model for the helical structure of geophysical flows in channel bends

This chapter based upon text published in Geophysical Research Letter (Azpiroz-Zabala et al. 2017; doi.org/10.1002/2017GL075721). The published 'Supplementary Information' has been relocated within chapter 2 of this thesis.

M. Azpiroz-Zabala[1,2], M.J.B. Cartigny[3], E.J. Sumner[1], M.A. Clare[2], P.J. Talling[3], D.R. Parsons[4], C. Cooper[5]

[1] Ocean and Earth Sciences, University of Southampton, European Way, SO14 3ZH Southampton, UK

[2] National Oceanography Centre, Southampton, European Way, SO14 3ZH Southampton, UK

[3] Departments of Earth Sciences and Geography, University of Durham, DH1 3LE Durham, UK

[4] Department of Geography, Environment and Earth Sciences, University of Hull, Cottingham Road, HU6 7RX Hull , UK

[5] formerly at Chevron Energy Technology Company, 6001 Bollinger Canyon Road, San Ramon, CA 94583 USA

Collection of the ADCP data for this article was led by Cooper. The data were analysed by Azpiroz-Zabala with assistance of Cartigny. The manuscript was written by Azpiroz-Zabala, assisted by Cartigny, Sumner, Clare, Talling and Parsons. This article has benefited from the reviews of Joris Eggenhuisen and Kori Konsoer, as well as editor comments.

Abstract

Meandering channels formed by geophysical flows (e.g., rivers and seafloor turbidity currents) include the most extensive sediment transport systems on Earth. Previous measurements from rivers show how helical flow at meander bends plays a key role in sediment transport and deposition. Turbidity currents differ from rivers in both density and velocity profiles. These differences, and the lack of field measurements from turbidity currents, have led to multiple models for their helical flow around bends. Here we present the first measurements of helical flow in submarine turbidity currents. These 10 flows lasted for 1–10 days, were up to ~80 m thick, and displayed a consistent helical structure. This structure comprised two vertically stacked cells, with the bottom cell rotating in the opposite direction to helical flow in rivers. Furthermore, we propose a general model that predicts the range of helical flow structures observed in rivers, estuaries, and turbidity currents based on their density stratification.

4.1 Introduction

Extensive submarine channels transport billions of tonnes of sediment for hundreds of kilometers, to form vast sedimentary deposits (called submarine fans) in the deep sea (Normark, 1970; Savoye et al., 2009; Shepard, 1933). The largest submarine fans are fed by highly sinuous submarine channels, suggesting that meander bends may enhance sediment transport distances (Pirmez & Imran, 2003; Straub et al., 2008). Submarine channels host powerful but episodic sediment-laden gravity currents called turbidity currents. Individual turbidity currents can transport more sediment than the annual flux from rivers worldwide (Talling et al., 2007). There are few direct observations of deep-sea turbidity currents (Cooper et al., 2016; Khripounoff et al., 2003; Talling et al., 2015; Vangriesheim et al., 2009). Before collection of this data set (Azpiroz-Zabala et al., 2017; Cooper et al., 2013), there were no detailed (subminute) measurements from within a meander bend in the deep sea. Instead, our understanding of meandering deep-sea channels was based on laboratory-scale experiments and numerical modeling, or on comparisons to rivers, estuaries, and saline density flows.

Rivers, estuaries, and saline underflows display a helical flow structure when passing through a bend, which can be broken into downstream and cross-stream components (Figure 4.1; Nidzieko et al., 2009; Parsons et al., 2010; Rozovskii, 1957; Sumner et al., 2014). The helical structure results from competing forces that drive the flow around a bend. Centrifugal acceleration drives fluid outward causing superelevation of the flow surface at the outer bend (Rozovskii, 1957; Thorne et al., 1985). Superelevation of the flow surface causes a pressure gradient that pushes fluid close to the bed toward the inner bend (Rozovskii, 1957; Thorne et al., 1985). Because the densest fluid in a stratified flow is near the bed, this inwardly directed pressure gradient can cause dense fluid to accumulate at the inner bend resulting in lateral stratification of the flow. Lateral stratification within the flow causes lateral pressure gradients; in particular, if dense fluid collects near the inner bend, then this will produce a near-bed pressure gradient that pushes fluid back toward the outer bend (Nidzieko et al., 2009; Sumner et al., 2014). The magnitude and rotation direction of helical flow cells is determined by the relative strengths of the above forces, which depend on the specific velocity and density structure of a flow and how this structure evolves around the bend. Helical flow is important because it strongly influences erosion and deposition within a channel and is thus a fundamental control on how channels evolve (Peakall et al., 2000; Rozovskii, 1957; Thorne et al., 1985).

Previous work has demonstrated that the helical structure can vary in two key ways. First, it can vary in the direction of rotation. Second, there can be a single helix (i.e., one rotating cell) or multiple helices stacked on top of one another (Corney et al., 2006, 2008; Imran et al., 2008). Helical circulation in rivers is dominated by a single helix that rotates in a clockwise direction when looking downstream through a left-hand bend (Rozovskii, 1957; Thorne et al., 1985). Initial numerical models for turbidity currents suggested that helical circulation is similar to that in a river bend (Kassem & Imran, 2004). However, the first physical experiments of helical circulation in turbidity currents showed an opposite direction of rotation—with the near-bed flow moving toward the outer bank (Corney et al., 2006; Keevil et al., 2006). To complicate matters further, both directions of helical circulation (river like and river reversed) have subsequently been observed in turbidity current experiments and models, depending on flow conditions and channel morphology (Abad et al., 2011; Bolla Pittaluga & Imran, 2014; Cossu & Wells, 2010; Dorrell et al., 2013; Ezz & Imran, 2014; Giorgio Serchi et al., 2011; Huang et al., 2012; Imran et al., 2007; Islam & Imran, 2008; Janocko et al., 2013).

Flow around bends in well-mixed estuaries show a river-like basal helical circulation, while stratified estuaries and saline flows are river reversed (Nidzieko et al., 2009; Wei et al., 2013). In stratified flows, across-flow variation in stratification (i.e., flow density) sets up an additional lateral pressure gradient that is thought to play a key role in determining the direction of the flow rotation (Nidzieko et al., 2009; Sumner et al., 2014). Such stratification-triggered pressure gradients have been suggested to be important for turbidity currents, which are density stratified because of vertical variations in sediment concentration (Peakall & Sumner, 2015; Sumner et al., 2014). This hypothesis remains untested because of a lack of field-scale observations of turbidity currents.

Here we present the first direct measurements of turbidity currents at a meander bend in the ocean, including 10 flows with varying flow conditions. We use these data to determine the rotation direction of helical flow within these turbidity currents. This provides the first field test of existing numerical and experimental models. Second, we determine how flow structure varies with fluctuating flow properties and discuss the implications for the morphological evolution of submarine channel bends. Finally, we compare our results with existing field measurements in other geophysical flows and propose a general model for helical flow structure across a wide range of geophysical flows, including rivers, saline density flows, and turbidity currents.

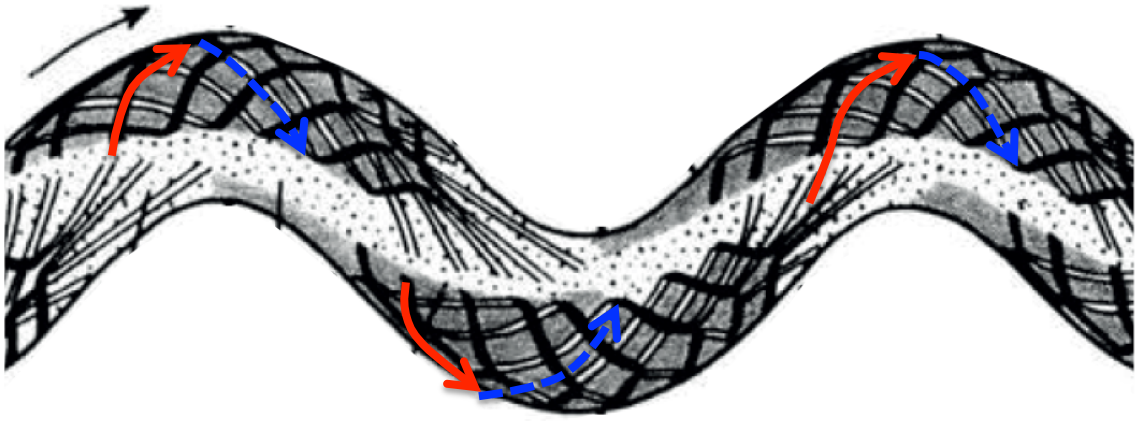

Figure 4.1. Schematic showing the helical flow observed in rivers (modified from Transportation Research Board, 2004). Red arrows indicate rotation of flow towards the outer bend. Blue arrows indicate rotation of flow towards the inner bend.

4.2 Study area

Our data were recorded at 2,000 m water depth in the Congo Canyon (Azpiroz-Zabala et al., 2017; Cooper et al., 2013). The Congo Canyon is the proximal part of one of the largest submarine channel systems on Earth, which is fed directly by the Congo River (Heezen et al., 1964). The submarine channel extends for over 1,000 km, from the continental shelf to its final termination at 5,000 m water depth (Heezen et al., 1964; Khripounoff et al., 2003). The upper part of the Congo Canyon has a meandering planform with tight bends, a deeply incised thalweg, and numerous terraces (Figure 4.2). The Congo Canyon is a highly active system in the present day. Several turbidity currents occur each year in the upper canyon, based on cable breaks (Heezen et al., 1964) and direct flow measurements (Azpiroz-Zabala et al., 2017; Cooper et al., 2013, 2016; Khripounoff et al., 2003).

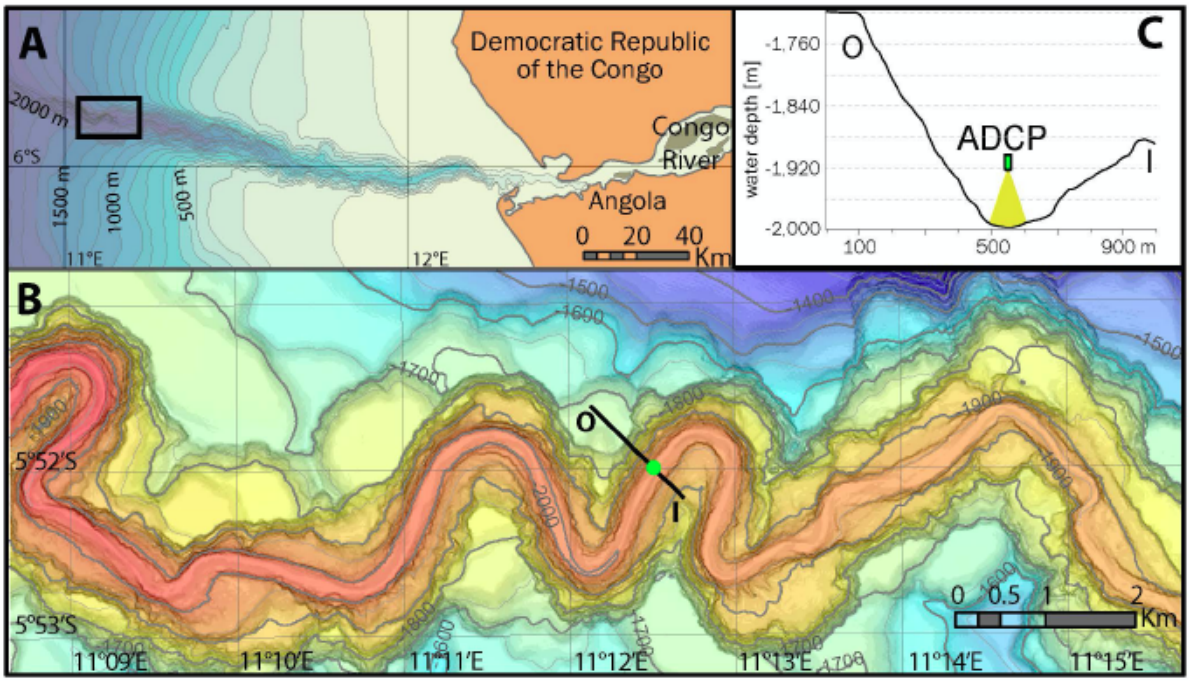

Figure 4.2. Location of the ADCP in the Congo Canyon. (A) Map of the Congo Canyon showing the study area (rectangle), with bathymetric contours in meters. **(B)** Detailed map showing the location of the instrumented mooring (green circle). Bold line indicates cross-canyon profile in Figure 4.2C. I and O denote the inner bend and outer bend, respectively. **(C)** Cross-canyon profile at deployment location showing acoustic Doppler current profiler (ADCP) suspended 85 m above the canyon floor.

4.3 Methods

This data set represents the first detailed direct measurements of turbidity currents in the deep ocean (Azpiroz-Zabala et al., 2017; Cooper et al., 2013). Ten flows were measured, with durations ranging from 8 h to over 9 days. Flow thicknesses varied from 16 m to 75 m, and flow velocities reached up to 2.3 m/s (Azpiroz-Zabala et al., 2017).

The data were collected using a 300-kHz acoustic Doppler current profiler (ADCP) anchored downstream of a meander bend in the Congo Canyon (Figure 4.2). The ADCP emits acoustic signals into the water column and computes averaged flow velocities over the acoustic footprint based on the Doppler shift (see chapter 2). The ADCP was downward looking and moored 85 m above the seafloor from December 2009 to March 2010 (Figure 4.2). Velocities were measured every 5 s and vertically averaged over 2 m high grid cells called bins (Cooper et al., 2013).

We deduce the helical circulation from the vertical velocity profiles measured by the ADCP by calculating primary and secondary velocities. We define primary velocity as follows. First, we evaluate the flow direction for each ADCP velocity measurement binned by depth and average the velocities in this vertical profile to obtain the mean flow velocity direction. The primary velocity is then the component of velocity parallel to the mean velocity direction in a horizontal plane. We then define secondary velocity as the component of the velocity measurements perpendicular to the mean velocity direction (Rozovskii, 1957). In a similar way to previous studies of helical flows made with single moorings, we use the secondary velocity to infer the helical flow structure (Nidzieko et al., 2009). The sign of the secondary velocity represents the direction of the secondary flow captured by the ADCP with positive values directed toward the outer bend and negative values toward the inner bend. The Rozovskii definition of secondary circulation assumes that the total outward directed velocity balances an equal total inward directed velocity. These secondary flow vectors define circulation cells that provide a two-dimensional view of the helical flow in the across-flow section (Figure 4.3 and schematic drawing in Figure 4.4B).

The ADCP data were processed using the following steps (see chapter 2 for more detail):

1. Data were linearly interpolated from velocities of 0 m/s at the seabed to the velocity value of the lowest reliable measurement at 5 m above the

seafloor following the method by Sumner et al. (2013) (side lobe interference area, see chapter 2).

2. The thickness of the flow is calculated following the integral relation by Ellison and Turner (1959).

3. The resultant vertical velocity profiles were depth averaged to obtain the average flow velocity and depth.

4. Primary and secondary velocities were calculated respectively as parallel and perpendicular to this average flow direction using the Rozovskii method (Rozovskii, 1957).

5. Additional interpolated velocity values in the side lobe interference area (see chapter 2), such as logarithmic values, were tested and similar general trends were obtained.

5. Results were averaged over 30 minutes to reduce sampling deviation of measurements.

6. Profiles influenced by tidal currents with magnitudes approaching that of the secondary circulation velocities were removed (see chapter 2).

7. Patterns of helical flow were analyzed by arranging the data by flow thickness.

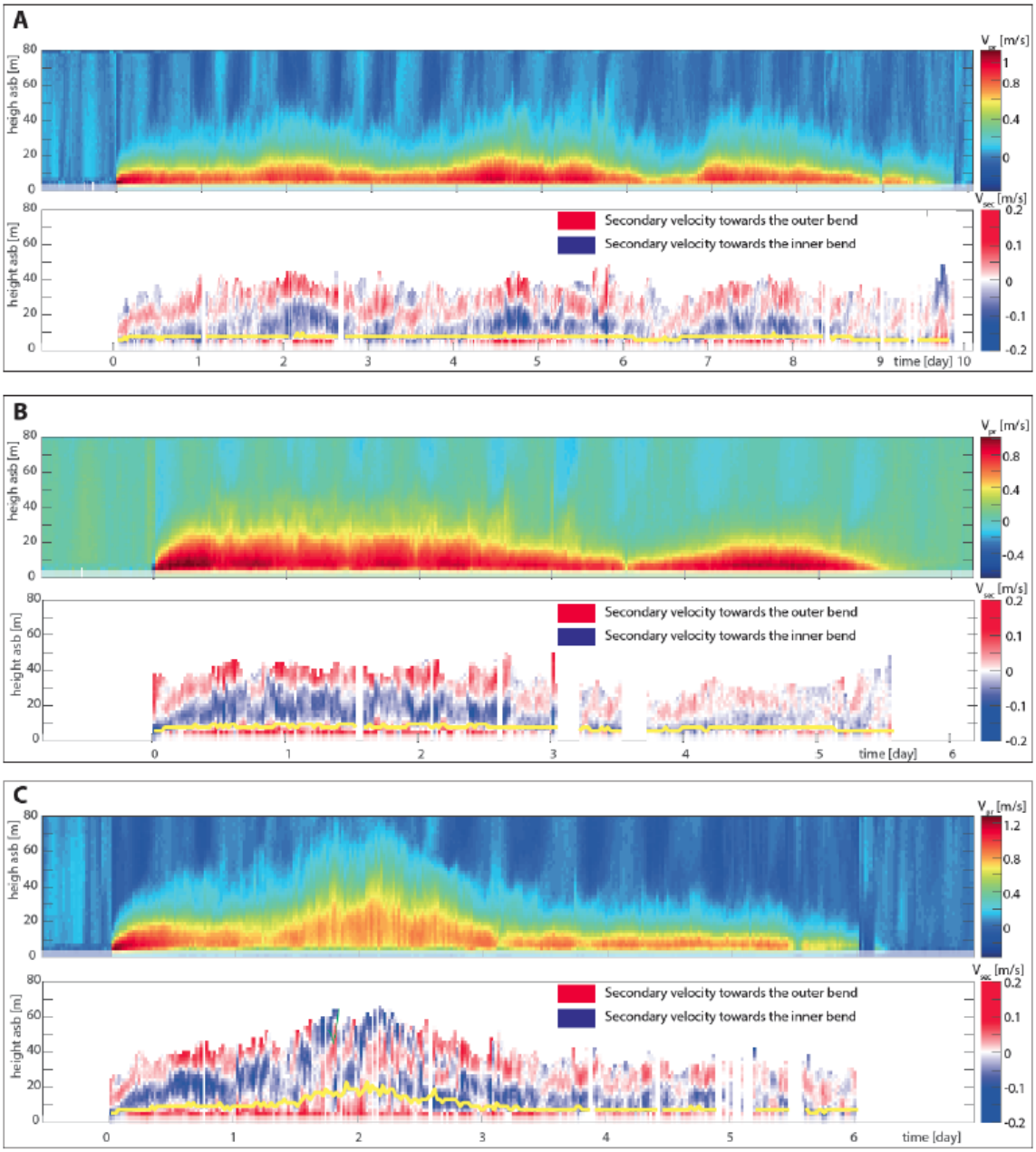

Figure 4.3 Primary (top) and secondary (bottom) velocities for three events recorded in the Congo Canyon. (A) Flow 1 is the longest duration flow. **(B)** Flow 4 shows the most stable secondary circulation structure. **(C)** Flow 10 is the fastest flow entirely recorded. Yellow lines in secondary velocity panels indicate height above the seabed (asb) of maximum velocity. Areas of side lobe interference are shaded at the bottom of each panel. Blank areas in secondary velocity panels define tidal currents (see chapter 2).

4.4 Results

We visualize and quantify helical flow in field-scale turbidity currents (Figure 4.3). The 10 measured flows vary in maximum thickness, duration, and primary velocity. Surprisingly, despite these variations, the secondary circulation pattern remains consistent among most flows (i.e., those 28–52 m thick; Figure 4.4). The secondary circulation comprises two vertically stacked cells, and this structure is independent of primary velocity and flow thickness (Figure 4.4). The lower cell rotates in a river-reversed direction, counterclockwise when looking downstream, while the upper cell has the opposite rotation direction (Figure 4.3 and schematic drawing in Figure 4.4B). In flows thinner than 28 m, the lower half of the bottom cell lies within the side lobe interference area and thus is not imaged accurately (see chapter 2). Flows thicker than 52 m appear to lack a consistent two-cell pattern; this results from having few (<3) profiles with these thicknesses, and thus individual profiles having a disproportionate impact on the average pattern (Figure 4.4).

The average normalized secondary flow profile has maximum velocities from 0.02 to 0.09 m/s, which are 2–5% of the corresponding primary flow velocity. The same two-cell pattern holds for thinner flows (28–34 m thick); however, the magnitude of secondary circulation is lower. In all cases, the center of the lowermost circulation cell corresponds to the height of the maximum primary velocity.

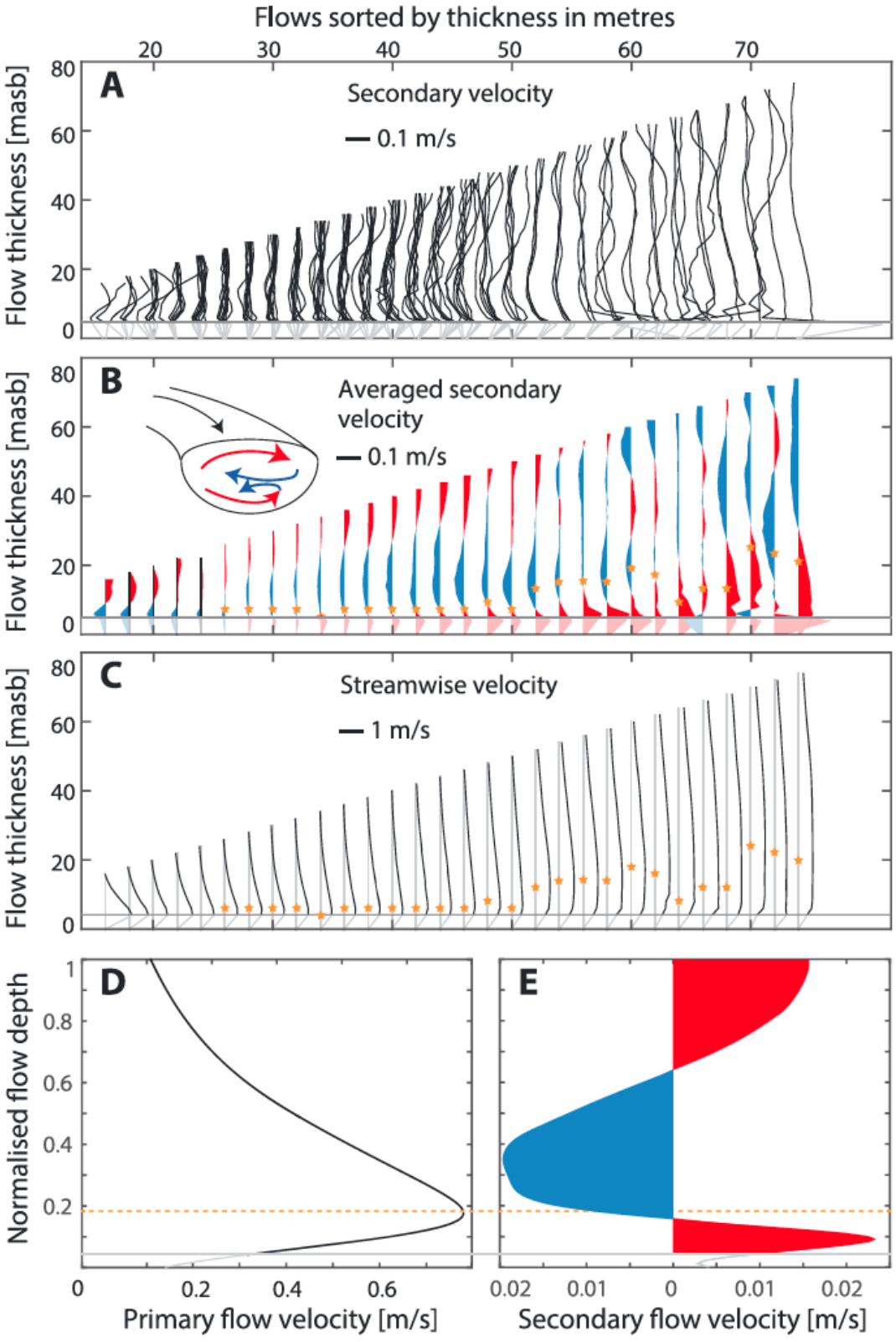

Figure 4.4 Profiles of the event-averaged primary and secondary velocity, which are ordered by flow thickness. (A) Event-averaged secondary velocity profiles arranged by their flow thickness. **(B)** Average of profiles shown in Figure 4.4A. Red colours denote positive secondary velocities, toward the outer bend. Blue colours denote negative secondary velocities, toward the inner bend. **(C)**

Event-averaged primary velocity profiles arranged by their flow thickness. **(D)** Depth-normalized primary velocity profile, and **(E)** depth-normalized secondary velocity profile constructed by averaging over all available measurements. Normalization has been calculated according to flow depth and might bias averaged velocities toward faster velocities. Masb in x axis in Figures 4.4A–4.4C denotes meters above seabed. The yellow stars in Figures 4.4B and 4.4C indicate the height of the maximum primary velocity. Profiles in side lobe interference area are shown in gray. Horizontal gray line marks the top of side lobe interference area.

4.5 Discussion

4.5.1 Observations of turbidity currents are consistent with previous models of stratified saline flows

Circulation cells form predominantly by the interaction of competing pressure gradients (Figures 4.5A–4.5C). In river-like circulation, centrifugal forces drive superelevation of the flow at the outer bend, generating a pressure gradient that drives near-bed flow toward the inner bend. River-like circulation can occur in density currents despite their near-bed velocity maximum because centrifugal acceleration moves the velocity maximum upward and outward (Sumner et al., 2014). In stratified saline density flows, an additional counteracting pressure gradient is generated by dense fluid accumulating near the inner bend, which sets up a lateral pressure gradient that drives near-bed flow toward the outer bend (Figures 4.5A and 4.5B) (Nidzieko et al., 2009; Sumner et al., 2014; Umlauf & Arneborg, 2009). Such lateral pressure gradients may be enhanced by lateral velocity variations (Eggenhuisen & McCaffrey, 2012a). If the stratification-triggered pressure gradient dominates, then near-bed fluid is forced back toward the channel axis causing a river-reversed direction of rotation (Nidzieko et al., 2009; Sumner et al., 2014; Umlauf & Arneborg, 2009). It was hypothesized that this mechanism might apply to sediment-laden turbidity currents (Sumner et al., 2014)—we provide the first field data to support this.

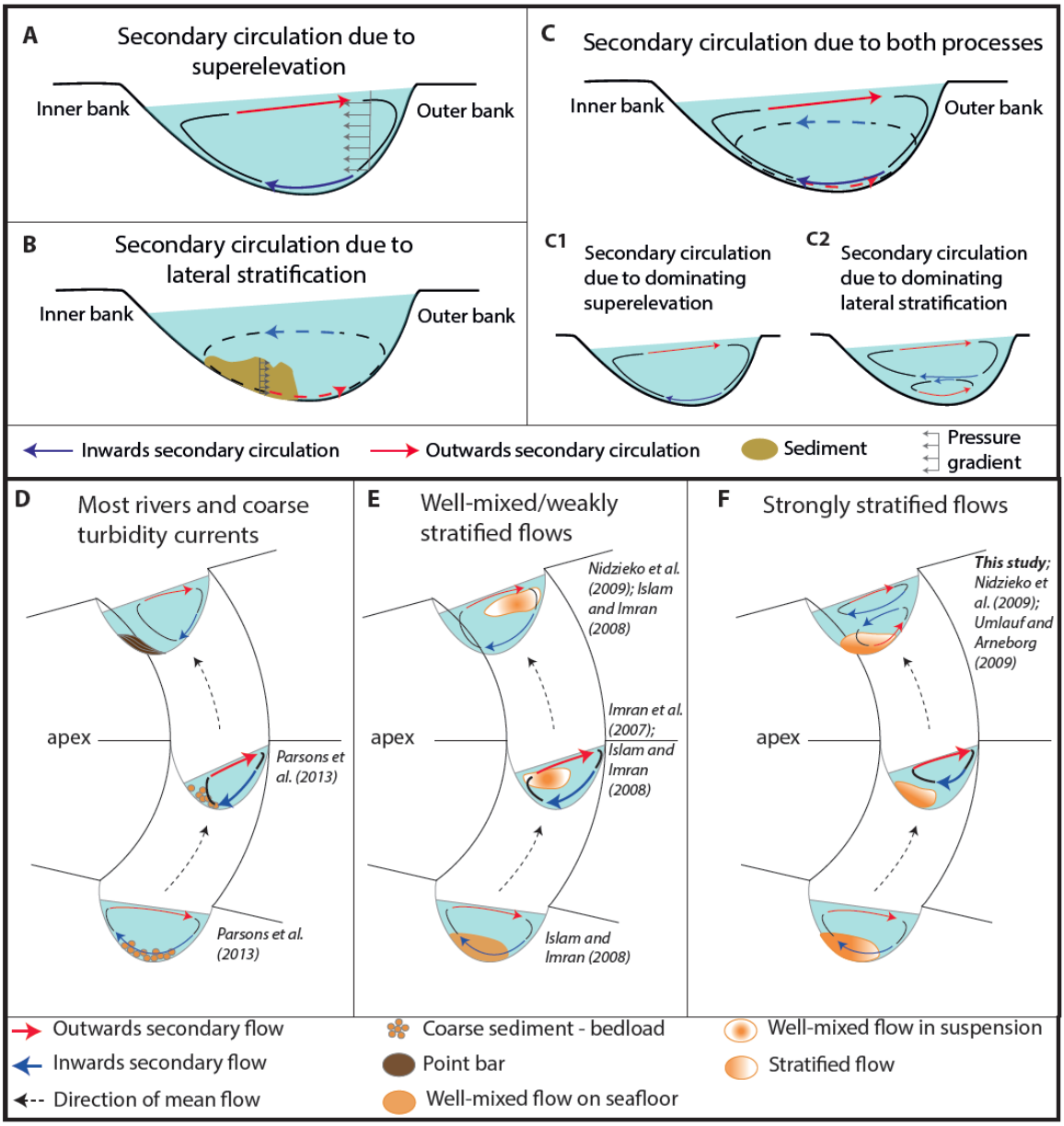

Figure 4.5 Schematic summary of secondary circulation patterns around a bend and their controls. Secondary circulation patterns result from competition between two main pressure gradients present in flows in bends. **(A)** Pressure gradient due to the water surface superelevation against the outer bend set up by centrifugal forces, and **(B)** pressure gradient due to stratification gradients in a density-stratified flow. Arrows denote resulting secondary flow patterns. Red denotes flow toward outer bend, and blue denotes flow toward inner bend, as in other figures. **(C)** Combination of secondary circulation cells due to superelevation and stratification pressure gradients in Figures 4.5A and 4.5B. Panel shows secondary circulation cells for two scenarios. The first scenario (C1) is when the pressure gradient due to superelevation is dominant, and the second scenario (C2) is when the pressure gradient due to density stratification is dominant. Schematic summaries of resultant secondary velocity around a bend.

(D) Model for most rivers and coarse turbidity currents (scenario A), **(E)** Model for well-mixed flows (scenario B), and **(F)** Model for stratified flows (scenario C). Thickness of secondary circulation arrows denotes intensity of the flow. Flow structures in the schematics were identified in the studies shown in italics next to the schematics.

4.5.2 Application of saline flow model to our observations

Our measurements were collected downstream from a bend apex (Figure 4.2). Therefore, the measurements are the result of evolving processes operating within the bend. As the flow travels around the bend, it experiences a centrifugal force that causes flow superelevation at the outer bend, generating a pressure gradient toward the inner bend (Figure 4.5A). This generates a single, river-like cell that pushes suspended sediment toward the inner bend. Accumulation of sediment-laden fluid at the inner bend causes a lateral pressure gradient that opposes the flow of sediment-laden fluid toward the inner bend (Figure 4.5B). In our observations just downstream of the apex, the centrifugal acceleration decreases, and therefore the inwardly directed pressure gradient (caused by superelevation) decreases. Thus, the outwardly directed pressure gradient (caused by stratification) equals the original superelevation-driven force. Cross-stream near-bed flow must stop before switching to become outwardly directed as the centrifugal forces start to decrease (Figure 4.5C). Our suggested model contrasts with earlier models that proposed that switching of secondary flow direction occurred between bends (Giorgio Serchi et al., 2011; Peakall & Sumner, 2015). Also, rather than reversing the original direction of the flow cell, this process spawns a new river-reversed near-bed flow cell, which is located beneath the original river-like flow cell (Nidzieko et al., 2009). This produces the observed two-cell structure. The upper cell is driven by pressure gradients due to flow superelevation. The lower cell is driven by pressure gradients due to lateral stratification (Figures 4.3 and 4.4). The thickness of the bottom cell is controlled by the height that sediment is elevated when pushed toward the inner bend. We observe correlation between the heights of maximum downstream velocity and the center of the bottom cell. This probably results from difficulties in mixing sediment across the low turbulence zone around the velocity maximum in turbidity currents (Eggenhuisen & McCaffrey, 2012b).

4.5.3 A general model for helical flow

In this section, we extend the above model to predict helical flow structure in a diverse array of geophysical flows, ranging from rivers to saline density flows and turbidity currents.

All flows experience centrifugally driven superelevation of their upper surface that creates a pressure gradient causing river-like helical flow (Figure 4.5A). This can cause accumulation of dense fluid or sediment toward the inner bend, which creates lateral stratification and causes an opposing pressure gradient back toward the outer bend (Figure 4.5B). We suggest that three potential scenarios exist (Figures 4.5D–4.5F), depending on which of these two pressure gradients dominate.

In scenario A (Figure 4.5D), a single weak river-like cell arises. The centrifugally driven pressure gradient displaces sediment to the inner bend as bed load but has insufficient energy to suspend the sediment. Therefore, there is no lateral stratification-driven pressure gradient back across the channel axis. We propose that scenario A occurs in bed load-dominated rivers and coarse-grained turbidity currents, and deposits point bars at the inner bend apex (Bagnold, 1977; Thorne et al., 1985).

In scenario B (Figure 4.5E), a single river-like cell is created. However, in this case the centrifugally driven pressure gradient is sufficient to move and suspend sediment at the inner bend. This results in a lateral stratification-driven pressure gradient that is smaller than the centrifugally driven pressure gradient. Thus, sediment remains in suspension and follows the streamlines of the circulation cell, causing overturning and mixing. We propose that scenario B occurs in well-mixed flows such as suspension-dominated rivers and saline flows, where sediment remains suspended with no deposition (Chikita, 1989; Nidzieko et al., 2009).

In scenario C (Figure 4.5F), two circulation cells are formed, with the lowermost cell showing river-reversed behavior. Here the centrifugally driven pressure gradient pushes sediment toward the inner bend. This stratification generates a lateral pressure gradient back across the channel. When the stratification-triggered pressure gradient is larger than the superelevation-triggered pressure gradient, cross-stream flow slows down and momentarily stops (Figures 4.5C and 4.5F). As the superelevation-generated pressure gradient decreases beyond the bend apex, the lateral pressure gradient due to sediment stratification causes

suspended sediment to flow back toward the channel axis. This generates a new helical flow cell, beneath the original cell. This bottom cell is river-reversed and is initiated just downstream of the bend apex where centrifugal forces decline. Above the new lower cell, the original river-like cell continues to rotate (Figure 4.5F). We propose that scenario C occurs in strongly stratified rivers, saline flows and turbidity currents, and sediment deposits downstream of the bend apex (Chikita, 1989; Darby & Peakall, 2012; Nidzieko et al., 2009; Parsons et al., 2010; Wei et al., 2013).

4.5.4 Application of the general model to a range of geophysical flows

Our new model differs from previous models (Dorrell et al., 2013; Giorgio Serchi et al., 2011; Peakall & Sumner, 2015) with respect to (i) the location in the channel system where a second basal cell develops and (ii) the importance of confinement in secondary circulation. In addition, our new model predicts the helical flow structure across a diverse array of particle-laden or saline flow types.

Previous work suggested that the rotation direction of secondary circulation is constant around an individual bend and only changes its rotation direction between adjacent bends (Giorgio Serchi et al., 2011). Here we propose that this hypothesis holds for the upper helical flow cell, which is governed by centrifugal forces. However, when a lower helical flow cell develops, this reversed flow cell is generated just downstream of the bend apex. Second, we propose that the level of confinement of the channel systems plays an important role in secondary circulation. In confined systems, sufficiently stratified flows will show an upper river-like helical flow cell. However, in unconfined systems this upper cell may overspill and thus destroy itself, leading to a single river-reversed basal circulation cell (Dorrell et al., 2013).

This new general model can be applied to a large range of flows, from coarse-grained rivers to saline density flows. Here we discuss the implications of the model for understanding the architecture and the evolution of submarine channels. We consider the behavior of multiple turbidity currents with the same size and stratification traveling through an evolving submarine channel. We hypothesize that stratified turbidity currents will behave according to scenario C of our model. In this case, near-bed flow is driven toward the outer bend by pressure gradients generated by density stratification within the flow. Previous studies suggested (Peakall et al., 2000) that this type of secondary flow causes

sediment to be deposited as point bars located downstream of bend apices. These point bars would increase the meander curvature, thus increasing the centrifugal forces and superelevation experienced by subsequent turbidity currents. However, once the pressure gradient toward the inner bend generated by superelevation exceeds the pressure gradient toward the outer bend generated by lateral stratification, then flow would switch to scenario B. In this case, near-bed flow is driven toward the inner bend by centrifugally driven pressure gradients. These pressure gradients exceed the lateral stratification-driven pressure gradients. As a consequence, the helical flow overturns sediment in suspension, thereby resulting in no deposition. At this point, the channel would cease meandering and its planform would become locked for flows of such size and stratification.

The largest submarine fans on Earth are fed by meandering channel systems. We propose that helical circulation around bends causes sediment to slosh from side to side or be overturned continuously, thereby helping to keep the sediment suspended over long distances. Together with fluid turbulence, helical flow thus plays a role in the extraordinary ability of turbidity currents to transport very large quantities of sediment for hundreds of kilometres.

Chapter 5:

Helical structure of a stratified gravity current on the Black Sea Shelf

This chapter is intended to be submitted to the Journal of Geophysical Research.

M. Azpiroz-Zabala[1,2], M.J.B. Cartigny[3], E.J. Sumner[1], M.A. Clare[2], P.J. Talling[3], J. Peakall[4], S.E. Darby[5], D.R. Parsons[6] and R.M.Dorrell[6]

[1] Ocean and Earth Sciences, University of Southampton, European Way, SO14 3ZH Southampton, UK

[2] National Oceanography Centre, Southampton, European Way, SO14 3ZH Southampton, UK

[3] Departments of Earth Sciences and Geography, University of Durham, DH1 3LE Durham, UK

[4] School of Earth and Environment, University of Leeds, Leeds, UK.

[5] Geography and Environment, University of Southampton, Southampton, UK.

[6] Department of Geography, Environment and Earth Sciences, University of Hull, Cottingham Road, HU6 7RX Hull , UK

The deposit data for this article were collected by Peakall, Darby, Sumner, Parsons and Wynn. The analysis for this chapter was carried out by Azpiroz-Zabala. This chapter was written by Azpiroz-Zabala with general comments, suggestions and editing by Sumner, Cartigny, Clare and Talling. The following people who were involved in the conception and execution of the Black Sea project will be co-authors on the submitted article but have not yet had the opportunity to review and comment on the text: Peakall, Darby, Parsons, Dorrell and Wynn.

Abstract

The flow structure of submarine density currents is fundamental in determining the locus of erosion and deposition in submarine channel systems and thus is important for understanding channel evolution. When submarine density currents flow around bends they adopt a helical structure. The structure and rotation direction of this helical structure in density currents has been a matter of contention and considerable debate over the last decade. We used an acoustic Doppler current profiler deployed from an autonomous underwater vehicle to study the three-dimensional structure of a density current flowing around a channel bend on the Black Sea Shelf. In addition, we measured the density of the flow and took grab samples to analyse sediment distribution on the seafloor. In order to study the helical structure of flows it is usual to decide upon a frame of reference and then decompose the flow into a downstream and a cross-stream component. Both components of the helical flow vary around meanders; however, most of the studies in submarine helical flows are based on the analysis of the cross-stream component only. Here we use different frames of reference (based on channel wall direction or flow direction) to calculate the downstream and cross-stream components of a submarine helical flow for which, unusually, we know the three-dimensional structure. Our results demonstrate that the chosen frame of reference strongly affects the apparent cross-stream structure of the flow to the extent that in different frames of reference the flow appears to rotate in different directions. This likely explains much of the apparent contradictions in the existing literature. We consider the suitability of different frames of reference. Furthermore, we compare the structure of the helical flow in this density current with predictions of what the helical flow should look like from previous models. Finally we consider the relationship between the measured flow with the morphology and sediment distribution on the seafloor.

Terminology

Downstream	Towards deeper water depths
Downstream	Towards deeper water depths following the direction of the flow
Cross-stream	Perpendicular to downstream direction

Cross-stream	Perpendicular to *downstream* direction
'Cross-channel'	Frame of reference that assumes that the cross-stream direction is normal to the channel direction
'*Rozovskii*'	Frame of reference that assumes that the cross-stream direction is normal to the depth-averaged flow direction
'*Zero net flow'*	Frame of reference that assumes that the cross-stream direction is normal to the transect-averaged flow direction

5.1 Introduction

Helical flows are spiralling flows that form at the bends of meandering channel systems. Their screw-shaped structure has been recognized in geophysical flows in diverse environments (i.e. gravity currents, estuaries, rivers) (Rozovskii, 1957; Nidzieko et al., 2009; Parsons et al., 2010; Sumner et al., 2014). Underwater meandering channel systems are associated with hydrocarbon reservoirs (Nilsen et al., 2008), and with submarine fans, which are the largest sediment deposits on Earth (Normark, 1970; Savoye et al., 2009; Shepard, 1933). Helical flows have been linked to the enhancement of sediment support, and thus transport, as well as causing increase in the curvature of meandering channel systems (Peakall et al., 2000; Pirmez and Imran, 2003; Straub et al., 2008). Increased curvature is a result of erosional and depositional patterns in the near-bed area, which in turn results from the structure of the helical flow throughout the depth of the flow.

Helical flow in rivers is well studied and understood (Rozovskii, 1957; Thorne et al., 1985). Centrifugal acceleration as rivers flow around bends causes the river surface to superelevate towards the outer bank. This generates a pressure gradient that pushes water at the base of the river towards the inner bank, with a return flow towards the surface of the river top that flows towards the outer bank (Rozovskii, 1957; Thorne et al., 1985).

In contrast to rivers, submarine flows, such as turbidity currents, are difficult to predict and to measure directly (Azpiroz-Zabala et al., 2017a; Clare et al., 2017; Inman et al., 1976; Talling et al., 2013). Consequently, their 3-dimensional (3D) helical structure has mainly been studied through experimental or numerical approaches. In order to do this, the flow is decomposed into downstream and

cross-stream two-dimensional (2D) slices (Abad et al., 2011; Bolla Pittaluga and Imran, 2014; Corney et al., 2006; Dorrell et al., 2013; Giorgio Serchi et al., 2011; Huang et al., 2012; Imran et al., 2007; Islam and Imran, 2008; Parsons et al., 2010). Thus, the 3D helical structure is viewed as a two-dimensional (2D) circulation cell or cells. Previous studies have made different conclusions about the helical structure of submarine gravity currents and its river-like (inwardly-directed) or river-reversed (outwardly-directed) basal circulation (Corney et al., 2006; 2008; Kassem and Imran, 2004; Imran et al., 2008). Recent studies highlighted the importance of considering the 3D nature of the helical flow and thus the limitations of viewing the helical structure in 2D (Azpiroz-Zabala et al., 2017b; Nidzieko et al., 2009; Sumner et al., 2014). These studies suggest that helical structure in submarine flows is mainly driven by the competition of pressure gradients due to (i) the superelevation; and (ii) the density stratification of the flow.

The magnitude and direction of these pressure gradients vary around the bend, and the time it takes for the flow to respond to these changing pressure gradients may also vary (lag time) (Azpiroz-Zabala et al., 2017b ; Nidzieko et al., 2009; Sumner et al., 2014). As a result, it may not be appropriate to try to balance the flow in a single 2D section because 2D sections study the flow structure within the defined section only and miss the variation of the flow structure in the third dimension. As such 2D views of the flow are partial representations of the flow that rely upon a frame of reference. This frame of reference is defined by arbitrary criteria that differ among different studies. For example, the frame of reference might be defined based on the direction of the channel or might be defined based on the direction of the flow. Additionally, the scarcity of direct measurements of submarine gravity flows around bends has prevented full 3D analysis of helical flow structure.

In this study, we present the first combined velocity and density field measurements of a continuous saline gravity flow at the entrance, apex and exit of a submarine bend. In order to study the flow we: (1) decompose the 3D flow into 2D slices using different frames of reference; (2) analyse how the different frames of reference affect our understanding of the structure of the helical flow; (3) compare the helical structure of the measured flow with previous models that aim to predict the structure of helical flow; (4) integrate measured 3D helical flow structure with measurements of grain size distribution and bathymetry of the

channel bend, to better understand the interaction between helical flow and sediment transport.

5.2 Area of study and methodology

5.2.1 Study area

The study area is located on the Black Sea Shelf, downstream from the Bosphorus Strait, which connects the Black Sea to the Marmara Sea. The study area comprises a channel and the surrounding shelf. The channel turns towards the West downstream forming an eroded bend on the seafloor, whose exit direction is approximately perpendicular to the entrance direction (Figure 5.1). The channel has most likely hosted submarine gravity flows for the past 7.5 ka (Flood et al., 2009). These submarine gravity flows occur as a result of the difference in density between the submarine flow and the ambient seawater. The Mediterranean Sea water excess of salinity (16-17 practical salinity units) with respect to the Black Sea water causes the excess of density that results in a submarine saline gravity flow through the channel.

The water depth of the channel thalweg within the bend spans from ~65 m to ~80 m, and the width of the channel ranges from ~400 m to ~725 m. The channel walls have heights from ~15 m to ~35 m above the thalweg (Figure 5.1).

Hydraulic jumps have been previously identified upstream of the bend (Figure 5.1). These hydraulic jumps disrupt the velocity structure of the flow, which then stabilises before entering the bend studied here (Dorrell et al., 2016; Sumner et al., 2013).

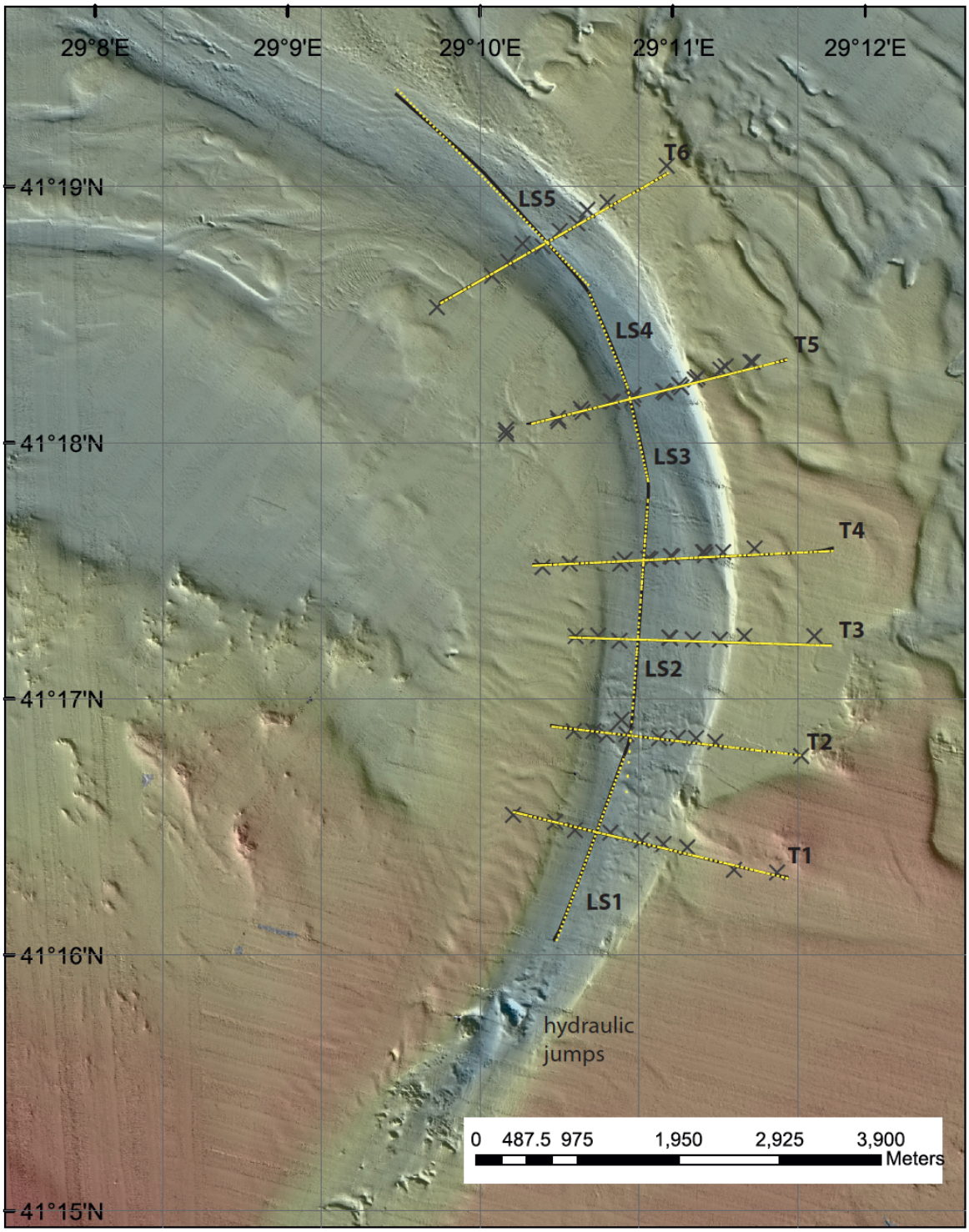

Figure 5.1. Bathymetry of the study area and surroundings showing cross-stream (T1-T6) and downstream transects (LS1-LS5). Black lines show AUV tracks, yellow lines show nearest approximation of ship tracks to straight lines. Stations of CTD deployments are marked with black crosses.

5.2.2 Data collection

The flow in this study was measured on the 1st and 2nd of July 2013 using a 600-kHz acoustic Doppler current profiler (ADCP) mounted on an autonomous underwater vehicle (AUV). The ADCP recorded the velocity of the helical flow along six cross-stream transects (T1-T6), and along one downstream multi-segmented transect (LS1-LS5), around the submarine channel bend (Figure 5.1). The downstream and cross-stream transects were designed as sections perpendicular and parallel to the channel respectively. Each of the six cross-stream transects was surveyed between 2 and 4 times. This was done to reduce the measurement scatter from one transect survey, and to obtain quantitative details of the flow structure (Parson et al., 2013; Szupiany et al., 2007). The ADCP was flown between ~10 and ~40 m above the channel floor.

Depth profiles of conductivity and temperature were measured using a conductivity-temperature-depth profiler (CTD) deployed at multiple stations along each of the six cross-stream transects (T1-T6). CTDs in transects T4 and T5 were deployed on different days (Table 5.1).

Transect	T1	T2	T6	T4	T5	T6
ADCP	01/07/13	01/07/13	01/07/13	01/07/13	01/07/13	01/07/13
CTD	03/07/13	02/07/13	03/07/13	28/06/13 30/06/13 01/07/13	30/06/13 02/07/13	01/07/13

Table 5.1. Days of collection of data in cross-stream transects.

The bathymetric data were collected using a hull-mounted EM302 multibeam echosounder (MBES) onboard the *RV Pelagia*, and an additional Reson SeaBat 7125 MBES also deployed from the *RV Pelagia*. The operating frequencies of the multibeam systems are 30-kHz and 200/400-kHz respectively.

The sediment grab samples were collected during a previous oceanographic cruise onboard the *RV Koca Piri Rei* in May 2010.

5.2.3 Methodology

5.2.3.1 Baseline calculations

All baseline calculations were processed in Matlab®. We analysed the ADCP data using the following steps:

1. Interpolation of datasets recorded at different time intervals onto a common time interval;
2. Interpolation of bottom track velocity, where data were missing;
3. Removal of AUV velocity component from the ADCP velocity measurements;
4. Correction of the ADCP deployment setting of East and North velocities relative to the AUV coordinate system (North was originally set as perpendicular to the AUV direction and East as parallel to the AUV direction);
5. Rotation of resultant flow velocities from a coordinate system relative to the AUV to a global coordinate system;
6. Calculation of the depth of each measurement using the height that the AUV was flying above the seafloor and the depth of the AUV beneath the sea surface;
7. Calculation of average straight-line plane (Parsons et al. 2013) for transects T1-T6 that were each surveyed several times;
8. Projection of measurements collected along irregular AUV tracks onto straight-line planes defined in step 7 (Parsons et al. 2013);
9. Interpolation of results on straight-line planes to obtain equally spaced flow measurements;
10. Arrangement of results in terms of Easting for transects T1-T6.

CTD measurements were processed according to the following procedure:

1. Application of the UNESCO 1983 methodology to obtain flow density profiles from the conductivity, temperature and depth CTD measurements (UNESCO, 1983);
2. CTD profiles were collected at several points (stations) along cross-stream transects T1-T6 (Figure 5.1). Measurements were collected every 0.25 m depth and data at the same depth between stations were interpolated;
3. Arrangement of results in terms of Easting;

4. CTD profiles collected along transects T4 and T5 were collected in different days. The above procedure was followed for the measurements collected on each day.

5.2.3.2 3D and 2D calculations of flow parameters

Using the above methods we built a 3D view of the helical flow structure. We then experimented with different existing methods to extract the 2D view of the flow. We now explain these methods, which were: (1) '*cross-channel*'; (2) zero net flow in profile or '*Rozovskii*'; and (3) zero net flow in cross-stream section or *'zero net flow'* (Figure 5.2).

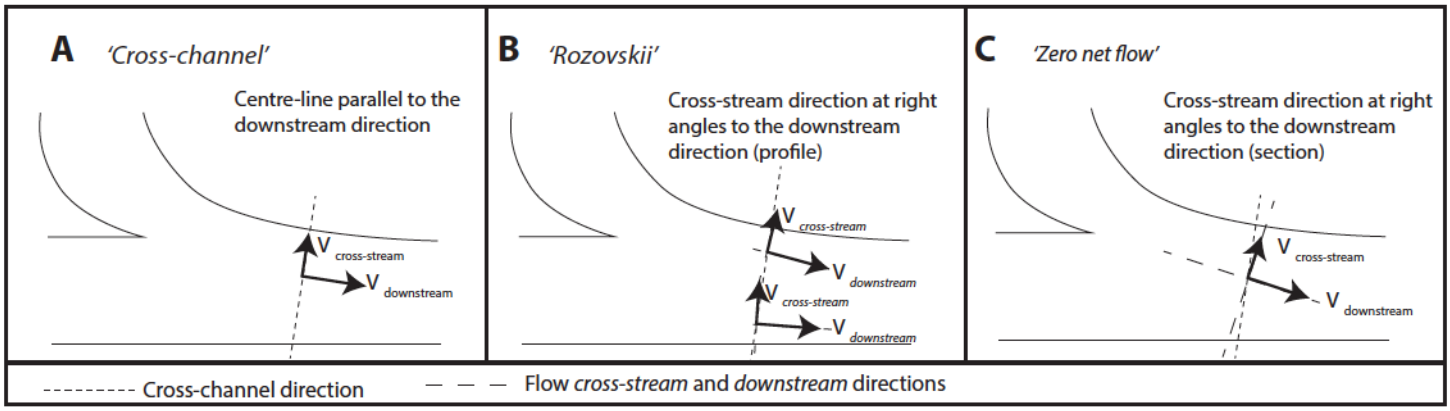

Figure 5.2. Schematic of the three methods ('*cross-channel*', '*Rozovskii*' and '*zero net flow*' used in this study to extract 2D view flow of the 3D helical flow (modified from Lane et al., 2000).

'*Cross-channel*'

This method defines that the cross-stream flow and the downstream flow are the flow normal and parallel to the channel margins respectively (Corney et al., 2006; Islam and Imran, 2008; Parsons et al., 2010; Sumner et al., 2014). The cross-stream transects in this work were designed to be normal to the channel axis. Therefore, velocities measured along the surveyed cross-stream transects represent '*cross-channel*' circulation, and the velocities perpendicular to them correspond to downstream circulation.

'Rozovskii'

This method is commonly used in river studies and states that the *cross-stream* flow is the circulation normal to the flow direction. The flow direction is calculated for each vertical flow profile as the averaged direction of the flow that permits a zero net circulation. Thus, the sum of the flow velocities towards the outer bend equals the sum of the flow velocities towards the inner bend in the vertical profile (Parsons et al., 2007; Rozovskii, 1957). The averaged direction of the flow is obtained from the mean of the components of the velocities at each measured depth. The '*Rozovskii*' *downstream* flow is the circulation parallel to the flow direction.

'*Zero net flow*'

Similarly to the previous method, the *cross-stream* and *downstream* flows are defined as the circulations normal and parallel to the flow direction. However, in this case, the flow direction is calculated as the averaged direction of the flow that permits a zero net circulation in the whole cross-stream transect (Dietrich and Smith, 1983).

5.3 Results

5.3.1 3D view of the flow

5.3.1.1 Saline flow and background current

All of the transects show a similar pattern for downstream velocity (Figure 5.3). The lower, confined part of the flow moves in a downstream direction; this is the saline gravity current. The upper, unconfined flow has upstream-directed velocities, and is a background oceanographic current. In upstream transects the gravity current has velocities of up to ~1.5 m/s (T1-T4 in Figure 5.1), whereas further downstream it has decelerated to ~1 m/s (T5 and T6 in Figure 5.1).

The top of the gravity current is defined as the sharp boundary between downstream and upstream velocities (Figure 5.3). It remains weakly unconfined in all cross-stream transects, either in the inner bend only (T1), or in both inner and outer bends (T2-T6).

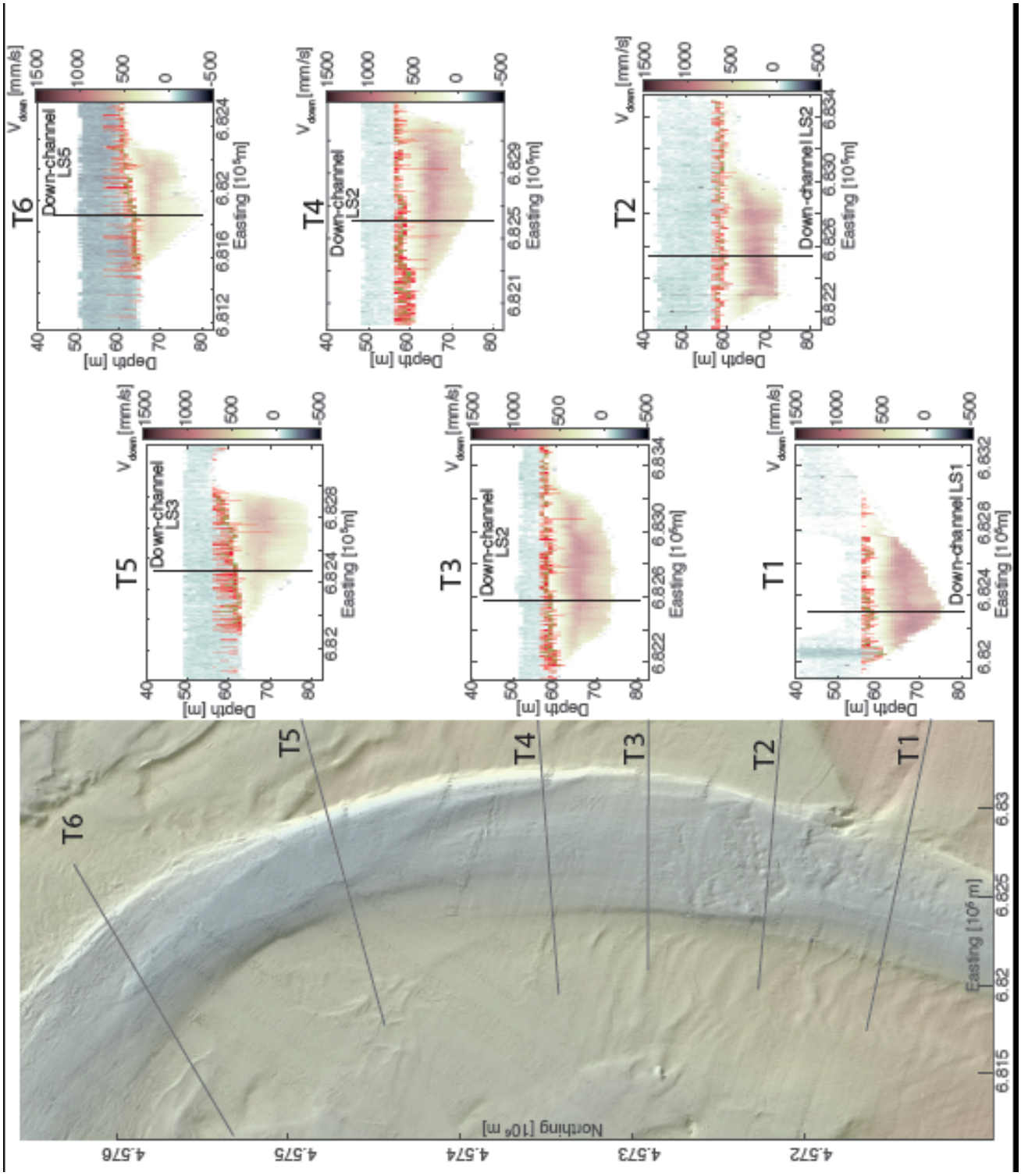

Figure 5.3. Downstream velocity and top of the flow. Positive velocities (in yellow and red) show downstream circulation of saline flow normal to transects T1-T6. Negative velocities (in blue) show upstream circulation of background current normal to transects T1-T6. Red line indicates zero downstream velocity, i.e. top of the saline flow based on collected measurements. This top of the flow has been smoothed to obtain the top of the flow shown in green. Saline current flows from bottom to top of figure.

5.3.2 2D view of the flow

The three different 2D frames of reference (‘*cross-channel’, ‘Rozovskii’* and ‘*zero net flow’*, see Methodology Section) are shown in Figure 5.4.

5.3.2.1 ‘Cross-channel’ circulation

The ‘*cross-channel’* circulation in transects T1-T4 shows an outward-directed velocity in nearly the whole section (Figure 5.4B). Inward-directed exceptions occur at the top of the saline flow (Figure 5.4B). This represents a circulation across the channel that has the opposite sense to river bends. However, the circulation switches towards a river-like structure in the transect T5, and such river-like circulation is fully developed in T6 (Figure 5.4B). The magnitude of the velocities towards the outer bend is higher than the magnitude of the velocities towards the inner bend. Maximum ‘*cross-channel’* values are measured in transects T1-T4 where they exceed 0.5 m/s (Figure 5.4B).

‘*Cross-channel’* circulation along transects LS1-LS3 show a consistent basal flow towards the outer bend, and occasionally weak flow towards the inner bend towards the top of the gravity current (Figure 5.5). This behaviour is reversed in transects LS4 and LS5 where the top and bottom of the *‘cross-channel’* circulation directs toward the inner and outer bend respectively (Figure 5.5).

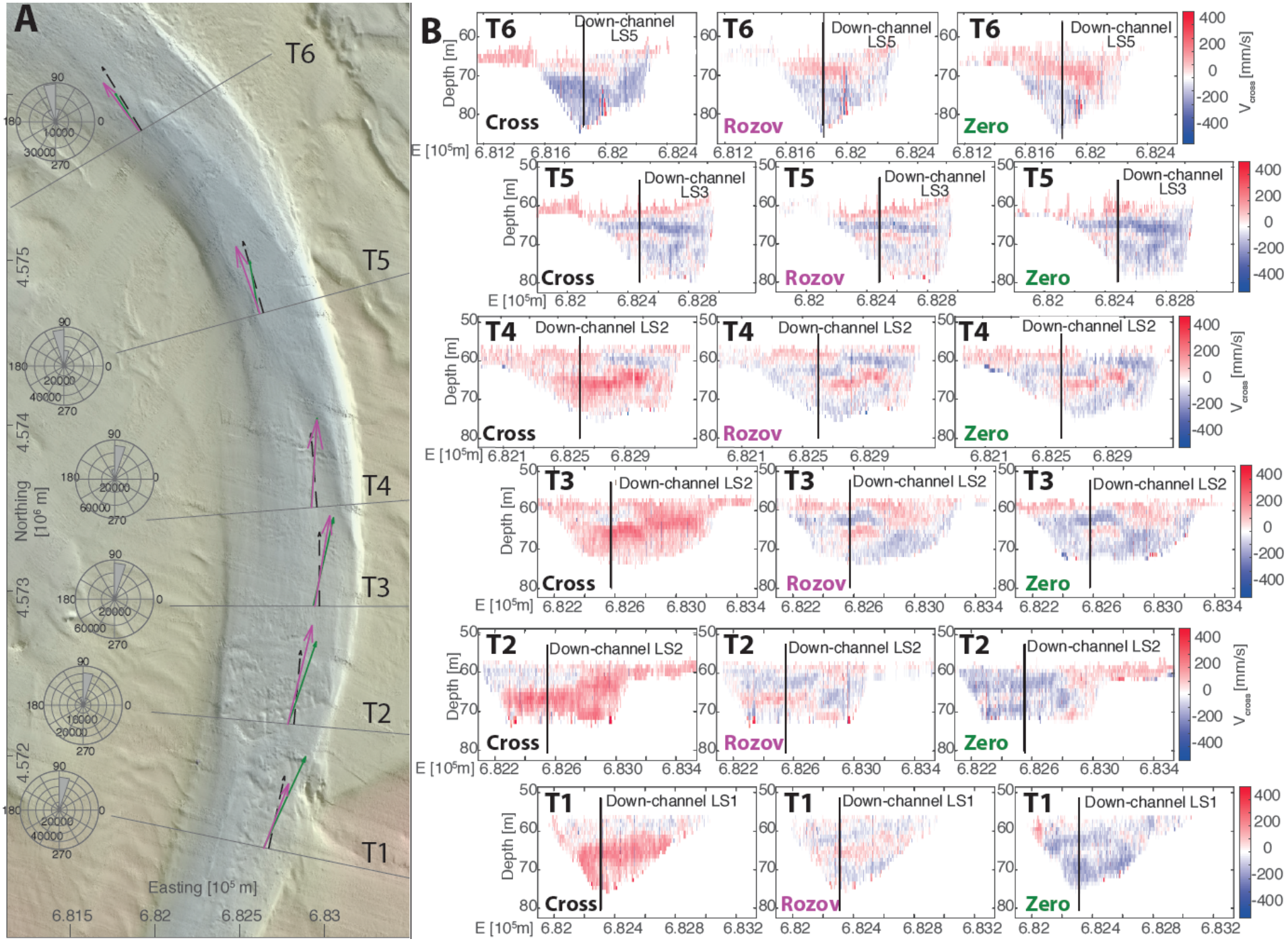
A
T6
T5
T4
T3
T2
T1
Northing [10⁶ m]
4.575
4.574
4.573
4.572
Easting [10⁵ m]
6.815
6.82
6.825
6.83
B
T6
Down-channel LS5
T5
Down-channel LS3
T4
Down-channel LS2
T3
Down-channel LS2
T2
Down-channel LS2
T1
Down-channel LS1
Cross
Rozov
Zero
Depth [m]
E [10⁵m]
V cross [mm/s]

Figure 5.4. 2D cross-stream velocities (right) and direction of saline flow (left) in transects T1-T6. (A) Direction of saline flow travelling around the bend. Rose diagrams show direction of saline flow at each surveyed point in T1-T6. Length of the flow direction vectors represents the magnitude of the velocity at each section/profile. Black, magenta and green arrows represent the directions according to '*cross-channel', 'Rozovskii'* and '*zero net flow'* frames of reference respectively. **(B)** Cross-stream velocities according to three frames of reference: '*cross-channel'* (in black), *'Rozovskii'* (in magenta) and '*zero net flow'* (in green). Positive velocities (in red) indicate circulation towards the outer bend. Negative velocities (in blue) indicate circulation towards the inner bend. Black lines in velocity panels indicate intersection with the downstream transect (LS1-LS5). Saline current flows from bottom to top of figure.

5.3.2.2 'Rozovskii' circulation

The results show inwardly directed near-bed flow in all transects except T2 and T5 (Figure 5.4B). This circulation shows a river-like bottom cell of circulation that is stacked with alternating flow cells with opposite (outwards/inwards) sense of rotation. T2 and T5 show a weak outwardly directed circulation at the base of the outer bend (Figure 5.4B). The absolute magnitudes of the velocities are below the maximum +/-0.5 m/s reached in other frames of reference (Figure 5.4B).

The flow is directed toward the outer bend in transects T1-T4 and slightly towards the inner bend in T5 and T6. The '*Rozovskii*' frame of reference and the '*cross-channel'* frame of reference differ by up to an angle of 15° in T3 (Figure 5.4A).

The '*Rozovskii*' circulation in the downstream transects (LS1-LS5) displays a regular structure with basal inwardly directed flow in all transects except LS3. A layer of opposite-directed flow towards the outer bend sits at the top of this basal flow. Occasionally, multiple layers that alternate the direction of rotation complete the profile (Figure 5.5).

5.3.2.3 'Zero net flow' circulation

All transects show a river-like basal circulation (Figure 5.4B). Thin outward-directed layers of flow are overlain by inwards-directed layers in T2-T5, which

represent multiple weak cells of circulation. Transect T6 shows a similar river-like pattern to the '*cross-channel'* and '*Rozovskii'* circulations (Figure 5.4B). The strongest circulation, which is inwardly directed, is displayed in transects T1, T2 and T5 (Figure 5.4B).

The flow is clearly directed towards the outer bend in transects T1-T5 (Figure 5.4A). The maximum rotations between the '*zero net flow'* and the '*cross-channel'* flow directions are a little less than 15˚ in transects T1-T4. The flow is directed towards the inner bend in T6. Here, the difference between the '*zero net flow'* and the '*cross-channel*' flow direction is less than 1˚ (Figure 5.4A).

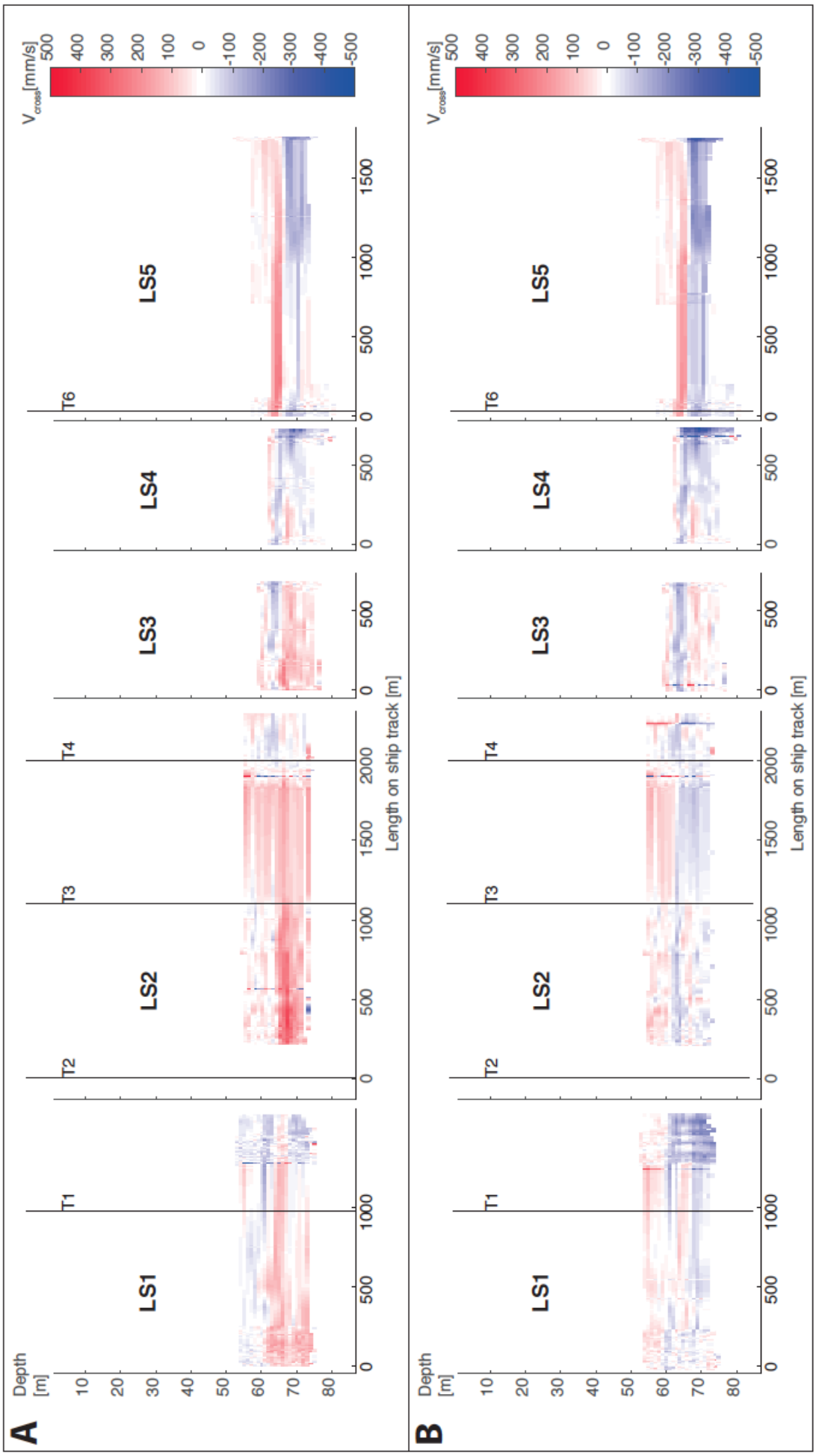
A
B
Depth [m]
10
20
30
40
50
60
70
80
LS1
LS2
LS3
LS4
LS5
T1
T2
T3
T4
T6
0
500
1000
1500
2000
Length on ship track [m]
V_{cross} [mm/s]
500
400
300
200
100
0
-100
-200
-300
-400
-500

Figure 5.5. (A) '*Cross-channel*' and **(B)** '*Rozovskii*' circulation at downstream transects (LS1-LS5). Vertical lines show intersection with transects T1-T6 (Figure 5.1). Positive velocities (in red) indicate flow direction towards the outer bend. Negative velocities (in blue) indicate flow direction towards the inner bend. Saline current flows from left to right of figure.

5.3.3 Differences among 2D flow views

This study demonstrates that the choice of frame of reference has a major impact on the appearance of the circulation cell, including whether it appears 'river-like' or 'river-reversed' (Figure 5.4B). When the angles between the different frames of reference are low (~1°), then the circulation cells look similar. However, when this angle between different frames of reference becomes high (~15°), then the circulation cells look very different (Figure 5.6).

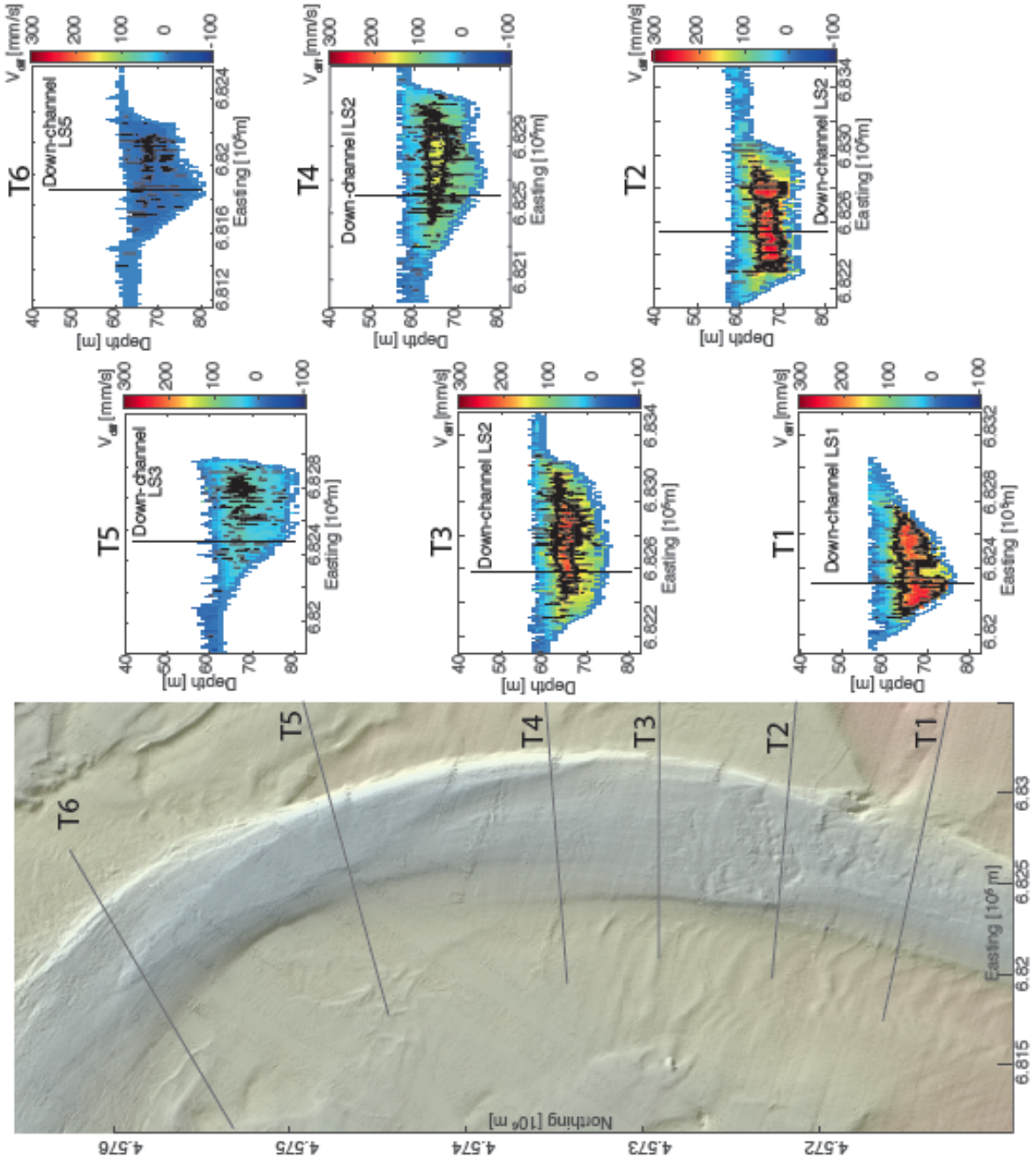

Figure 5.6. Difference between magnitude of '*cross-section*' and '*zero net flow*' velocities. '*Cross-section*' and '*zero net flow*' velocities are shown in Figure 5.4. Black contour indicates downstream velocities higher than 0.8 m/s. Saline current flows from bottom to top of figure.

5.3.4 Density results

The density structure of the saline flow is similar in transects T1-T6. Maximum and minimum densities are between 1,014 gr/l and 1,027 gr/l and these

isopycnals are located between 10 and 16 m of depth apart from each other (Figure 5.7). In all transects, the densest fluid accumulates in the inner bend, as previously observed in other saline flows (Nidzieko et al., 2009; Sumner et al., 2014).

The collection of multiple CTD casts on different days in transects T4 and T5 (Table 5.1) enables analysis of density variability on different days. In cross-stream transect T4, the 1,024 gr/l isopycnal rises 5 m between 28th of June 2013 and 30th of June 2013 linked to an increase of basal flow density up to 1,027 gr/l (Figure 5.7). A similar ~1,027 gr/l density is observed on the 30th of June at the flow inner bottom in transect T5. This value decreases to 1,025 gr/l approximately by the 2nd of July 2013 (Figure 5.7).

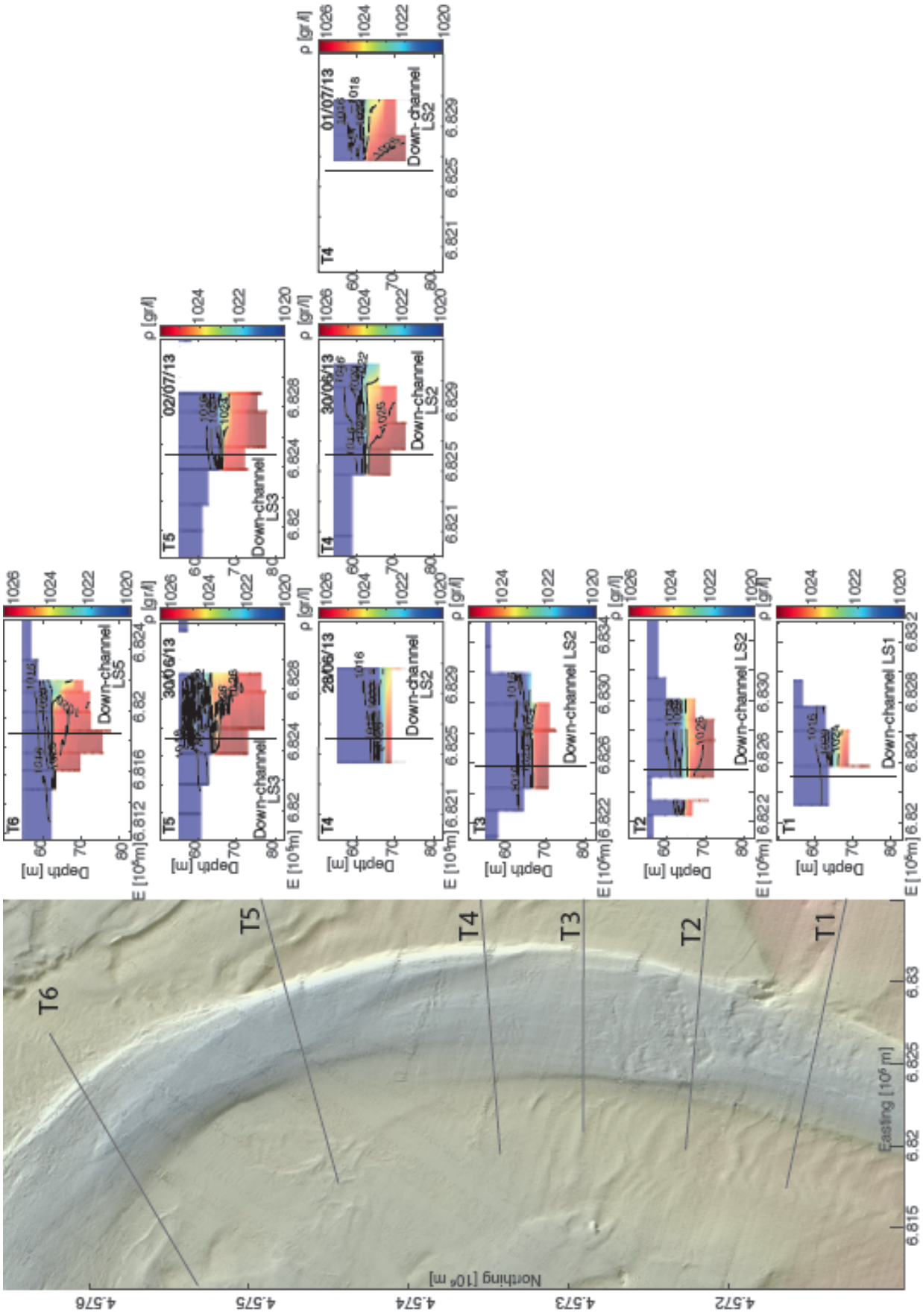

Figure 5.7. Profiles of density [gr/l] of the saline flow in cross-stream transects (T1-T6). Calculations of density according to UNESCO 1983 standard based on CTD data. CTD casts in transect T4 and T5 were collected in several

days (Table 5.1) – day of collection is shown within profile plot. E stands for Easting. Saline current flows from bottom to top of figure.

5.3.5 Grain size distribution and bathymetry in the channel

Grain size and bathymetric data were collected to understand the relationship between the flow and its deposits. Grain size in the channel shows a general fining trend with distance downstream (Figure 5.8). Coarse grains (gravels and sands) dominate the sediment in the channel floor of the most proximal cross-stream transects (T2 and T4). In contrast, muddy material predominates in the samples within the channel along transect T5 and the inner channel bend of T6 (Figure 5.8).

The cross-sectional shape of the channel varies around the bend (Figure 5.8). The position of the channel thalweg is harder to define in cross-stream transect T2 than in the other cross-stream transects in this study (Figure 5.8). Two channels occur within cross-stream transect T4 with one towards the inner bend and one towards the outer bend (Figure 5.8). Cross-stream transect T6 shows an outer bend bar (Figure 5.8). The comparison between cross-stream transects highlights the transition between V-shaped thalwegs in T1 and T6 and U-shaped thalweg in the intermediate cross-stream transect T3 (Figure 5.8). The water depth of the channel thalweg is between 70-75 m in transects T1-T4 and drops to ~80 m in transect T5 and T6 (Figure 5.8). The outer walls within the channel are consistently steeper than the inner channel walls (Figure 5.8).

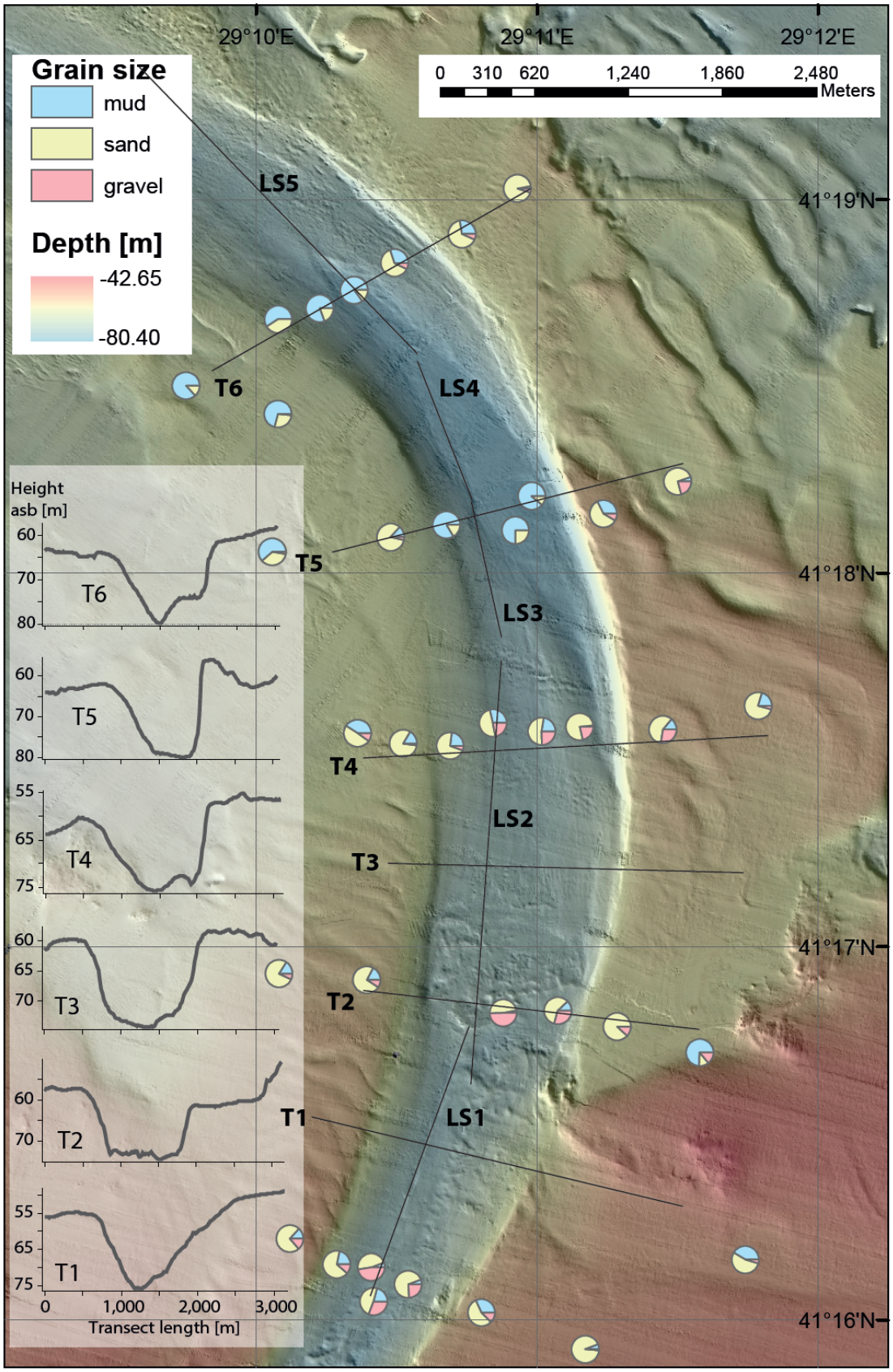

Figure 5.8. Grain size distribution and cross-sections of the channel. Gravel fractions (in pink) are found within the channel in all of the upstream transects (T2 and T4). Sands (in yellow) are present within the channel in all the bend transects; they are more abundant in upstream transects (T2 and T4). Muds (in

blue) dominate the composition of the samples collected within the channel in downstream transects (T5 and T6). Saline current flows from bottom to top of figure.

5.4 Discussion

5.4.1 Representations of flow behaviour in different frames of reference

We have shown that depending on the frame-of-reference chosen, then the helical flow can appear to rotate in different directions (Figure 5.4). In this section, we analyse the origin of these differences, and the accuracy of each frame of reference *('Cross-channel', 'Rosovskii'*, and *'zero net flow'*) as representations of the actual flow behaviour.

5.4.1.1 Origin of differences between 2D cross-stream flow velocities

Our results demonstrate that when frames of reference coincide they produce similar-looking flow structures. The greater the difference in angle between the frames of reference, then the greater the difference in the apparent structure of the flow's circulation pattern (Figures 5.4 and 5.6). This is important because it has not been accounted for in previous studies, and the choice of reference frame can define whether flow is observed as 'river-like' or 'river-reversed'. This has been a matter of great debate in literature over the past 15 years (Abad et al., 2011; Corney et al., 2006; 2008; Dorrell et al., 2013; Imran et al., 2008; Kassem and Imran, 2004).

T6 is an example of a transect where the three frames of reference are similar and, as a result, the cross-stream circulations nearly match (Figures 5.4 and 5.6). By contrast, the largest rotations among frames of references occur in transects T1-T4 (Figure 5.4A), and as a result, the apparent circulations are very different (Figures 5.4B and 5.6). Here both '*cross-channel'* velocities and downstream velocities, which are one order of magnitude higher than the '*cross-channel'* velocities, point towards the outer bend.

Figure 5.6 also highlights a second factor that controls apparent differences in circulation patterns. In any single cross section, the biggest difference in cross-

stream velocities between different frames of reference coincides with the location of highest downstream velocity (Figure 5.6). Therefore, it is the combination of both (1) angle between frames of reference; and (2) magnitude of the downstream velocity that results in large differences in the apparent circulation between frames of reference.

The discrepancy between 2D sections originates in the method of decomposition of the 3D helical flow into sets of 2D downstream and cross-stream components. The larger the difference in angle between frames of reference, the larger the discrepancies among 2D sections. Some sets of velocity components (i.e. downstream component and cross-stream component) viewed in different frames of reference can produce helical flows with apparently opposite sense of rotation (Figure 5.4B). This occurs for certain angles of rotation between frames of coordinates combined with certain magnitudes of those components. The magnitude of the downstream component of the velocity is always higher than the cross-stream component, and is orientated towards the outer bend (Figures 5.3 and 5.4). The decomposition of the downstream flow into the '*cross-channel*' frame of reference results in a large '*cross-channel*' component pointing towards the outer bend (Figure 5.9). This component dominates the 2D representation of the '*cross-channel*' circulation (Figure 5.4B).

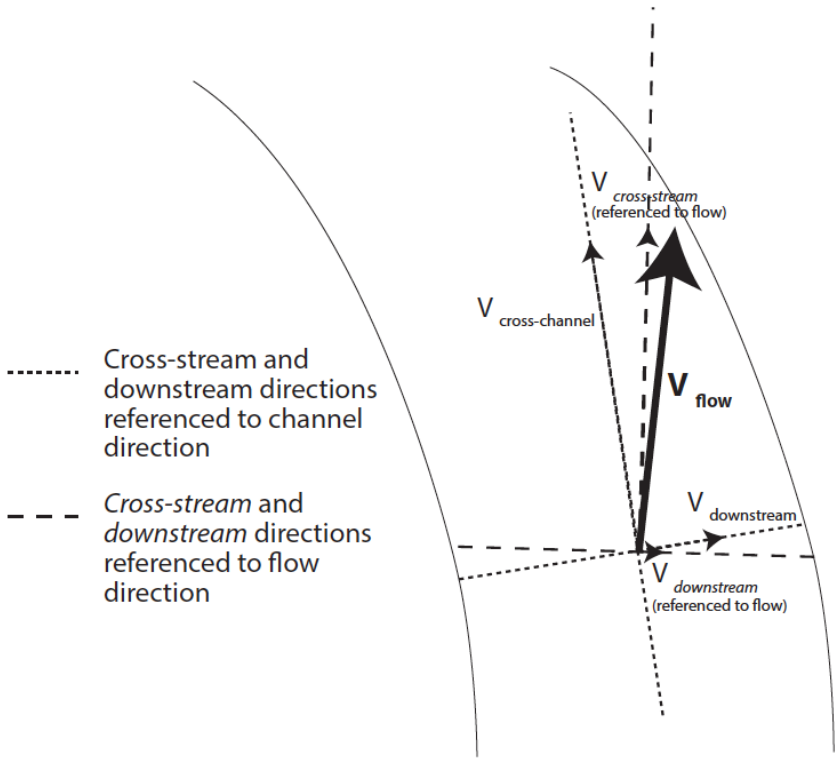

Figure 5.9. Schematic of 3D vector decomposition into the 'cross-channel' and 'Rozovskii/'zero net flow' frames of reference.

5.4.1.2 Appropriateness of different 2D frames of reference.

The decomposition of 3D flows into 2D components influences the apparent structure of the circulation, to the extent that flow cells can apparently show different senses of rotation. The full 3D helical flow through transects T1-T4 has a basal circulation towards the outer bend, whereas the '*zero net flow'* frame of reference shows a basal circulation towards the inner bend (Figure 5.4). We have identified the origin of the discrepancy between 2D representations of the 3D flow (above). This will help to enable reconciliation among apparently contradictory conclusions of previous studies thus leading to better interpretations.

The helical flow structure, and the different methods for viewing this structure in 2D, is much better studied for rivers, than for submarine gravity currents. Ashmore et al. (1992) concluded that the '*cross-channel'* frame of reference is not necessarily representative of the flow behaviour because rivers might not naturally flow parallel to the channel direction. River studies commonly use the '*Rozovskii*' frame of reference and, less commonly the '*zero net flow'* frame of reference (Dietrich and Smith, 1983; Parsons et al., 2007; Rozovskii, 1957). Both assume steadiness of flow, and the '*Rozovskii*' frame presumes no lateral fluxes (i.e. overspill) into or out of the channel (Parsons et al., 2007; Rozovskii, 1957). Similarly to rivers, the direction of submarine gravity currents can differ from the channel direction (Figure 5.4). Thus, the '*cross-channel'* frame of reference is not necessarily a good representation of the velocity structure across the flow. However, in contrast to rivers, submarine flows often overspill the channel (Peakall et al. 2000; Peakall and Sumner, 2015), thus violating an assumption of the '*Rozovskii*' method (Figure 5.10). The saline gravity current, in this study, is probably best represented using the '*zero net flow*' frame of reference (Figure 5.10).

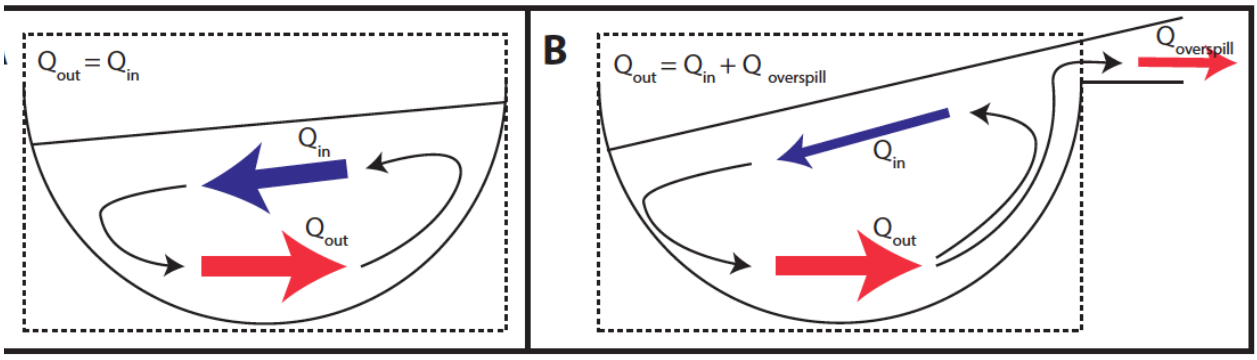

Figure 5.10. Schematic showing the influence of overspilling on the '*Rozovskii*' frame of reference. The dotted rectangle indicates the scope of the calculations on the '*Rozovskii*' frame of reference. The solid line rectangle indicates the scope of the calculations on the '*zero net flow*' frame of reference.

5.4.2 Comparison of our results with previous 3D models based on from field observations of geophysical flows

Previous 3D models of helical flows around bends proposed that the cross-stream flow structure is governed by two main pressure gradients. These forces develop from the centrifugally-driven superelevation of the flow and the density stratification of the flow and both forces act normal to the flow direction (Azpiroz-Zabala et al., 2017b; Nidzieko et al., 2009; Sumner et al., 2014). The pressure gradient due to the flow superelevation causes a river-like helical flow structure, such that the near-bed flow is directed towards the inner bend (Azpiroz-Zabala et al., 2017b; Nidzieko et al., 2009; Sumner et al., 2014). The magnitude of the centrifugally-driven pressure gradient is proportional to the centrifugal acceleration of the flow. This centrifugal acceleration reaches its maximum at the peak velocity in a flow depth profile, and at the bend apex in a plan view of the flow around the bend (Azpiroz-Zabala et al., 2017b; Sumner et al., 2014;). The centrifugally-driven pressure gradient causes accumulation of dense fluid at the inner bend. This accumulation of dense fluid generates lateral flow stratification across the channel width, which reaches its maximum at the bend apex. This density stratification causes a lateral pressure gradient that is opposed to the pressure gradient caused by superelevation. This lateral pressure gradient consequently pushes the basal flow back towards the outer bend (Azpiroz-Zabala et al., 2017b; Nidzieko et al., 2009; Sumner et al., 2014). The eventual cross-stream structure of the flow results from the combination of both pressure gradients. Thus, river-reverse basal circulations develop in sufficiently stratified flows, where the lateral pressure gradient due to stratification exceeds

the pressure gradient due to flow superelevation (Azpiroz-Zabala et al., 2017b; Nidzieko et al., 2009; Sumner et al., 2014).

In this study, we see that the densest fluid accumulates towards the inner bend in all cross-stream transects (Figure 5.7). The '*zero net flow*' circulation displays a basal river-like circulation through all transects. Isolated areas with river-reversed circulation also develop at higher heights above the seabed of intermediate transects T3-T5 (Figure 5.4B). The application of the general model for helical flows suggested by Azpiroz-Zabala et al. (2017b) predicts that the saline flow in this work is insufficiently stratified. Thus, the lateral pressure gradient developed due to stratification is unable to compensate the river-like pressure gradient due to the superelevation (Figures 5.4B and 5.6; Azpiroz-Zabala et al., 2017b). Consequently, the 3D circulation across the flow shows a river-like behaviour in all the cross-stream transects (T1-T6) in this study (Figure 5.11). This river-like basal cross-stream circulation has been previously observed in well-mixed or low-stratified saline flows in estuaries (Chant, 2002; Nidzieko et al., 2009).

The isolated areas that display outer-directed circulation coincide with areas of high downstream velocity (Figures 5.3 and 5.4). These areas represent the local outwards-directed centrifugal force that dominates the cross-stream circulation in this saline flow (Azpiroz-Zabala et al., 2017b; Sumner et al., 2014).

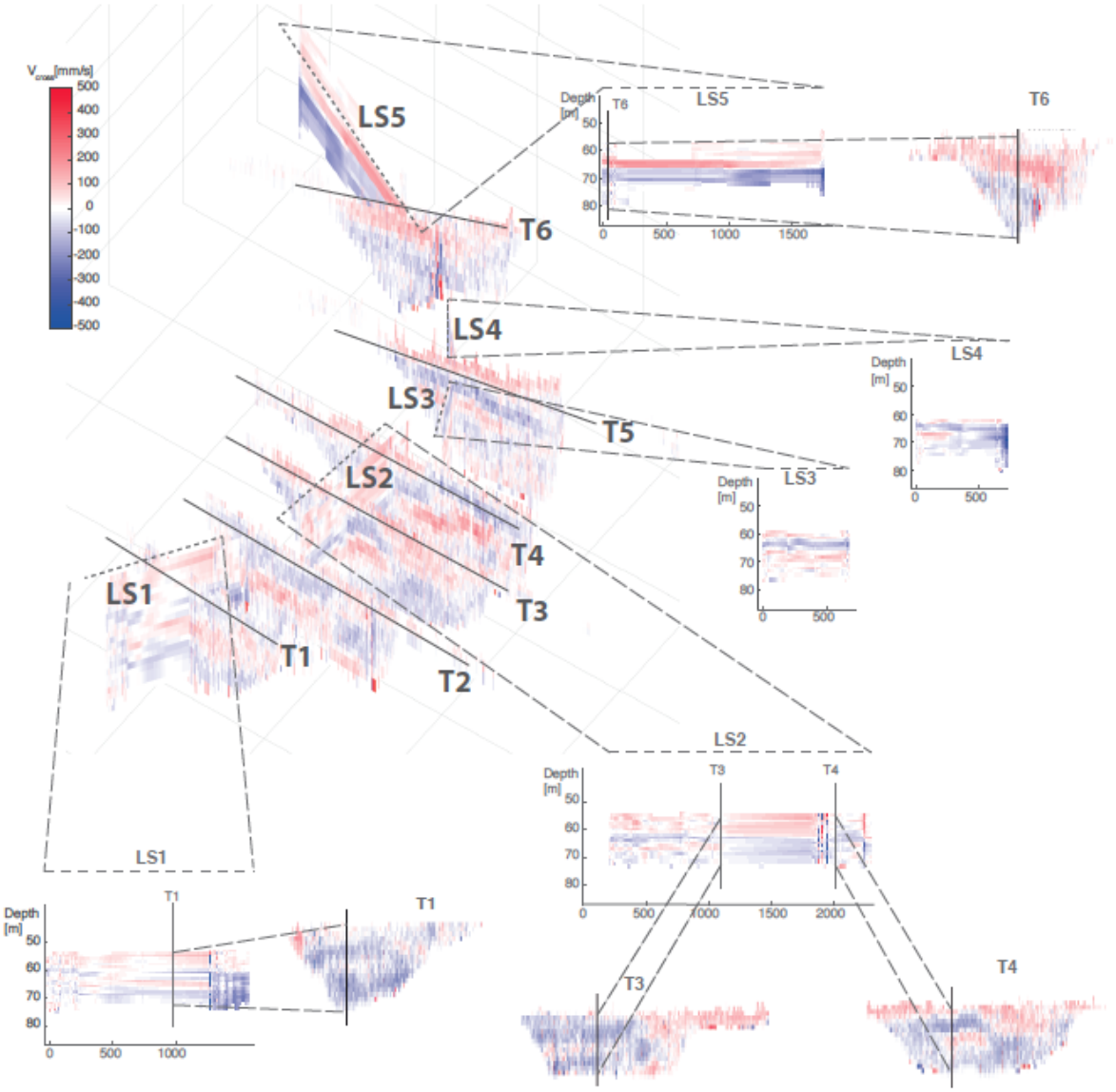

Figure 5.11. 3D view of circulation across the flow around the bend and 2D views of the circulation in downstream transects LS1-LS5 and cross-stream transects T1-T6. 3D compilation of '*zero net flow*' circulation (in transects T1-T6) and "*Rozovskii*" circulation (in transects LS1-LS5). Positive velocities (in red) indicate motion towards the outer bend. Negative velocities (in blue) indicate motion towards the inner bend. Saline current flows from bottom left to top left of the 3D figure.

5.4.3 Integration of flow dynamics and deposits characteristics

Merging the downstream flow view, with 2D cross-stream flow representations based on the flow direction or from field measurements, provides a 3D view of

the entire flow. The near-bed flow determines sediment transport and thus the location of deposition and erosion, however, such topography will in turn influence the flow.

The direction of the flow near the seafloor evolves around the bend in response to the forces acting on the flow but also in response to the local bathymetry of the seafloor. The maximum values of near-bed velocity occur in the centre of the channel in cross-stream transects T1-T3. The maximum values shift towards the outer bend in T4 and stay at the outer bend in T5 and T6 (Figure 5.12). The basal flow velocity decreases between cross-stream transect T4 and T5 and increases again between T5 and T6. The drop in basal velocity between transects T4 and T5 might be caused by a change in the channel bathymetry. The channel depth increases between cross-stream transects T4 and T5 (Figure 5.7), which might result in a deceleration of the basal flow or the development of recirculation cells in the basal flow. The reduction in the depth-averaged *downstream* velocity between transects T4 and T5 might be caused by a difference in channel area between transects T4 and T5 (Figure 5.12). The larger drop in the basal velocity between transects T4 and T5 than in the depth-averaged *downstream* velocity suggests at least some bathymetric influence, which might be the drop of the seafloor between transects T4 and T5 (Figure 5.8). The maximum velocities are located at ~65-70 m depth in all cross-stream transects T1-T6 (Figures 5.3 and 5.4B). However, the channel floor depth increases from T4 to T5 by 5 m (Figures 5.5 and 5.8). The sustained depth of the maximum velocities combined with the change in channel floor depth might result in the drop of the basal flow velocities that follow a local bathymetric change (Figures 5.8 and 5.12).

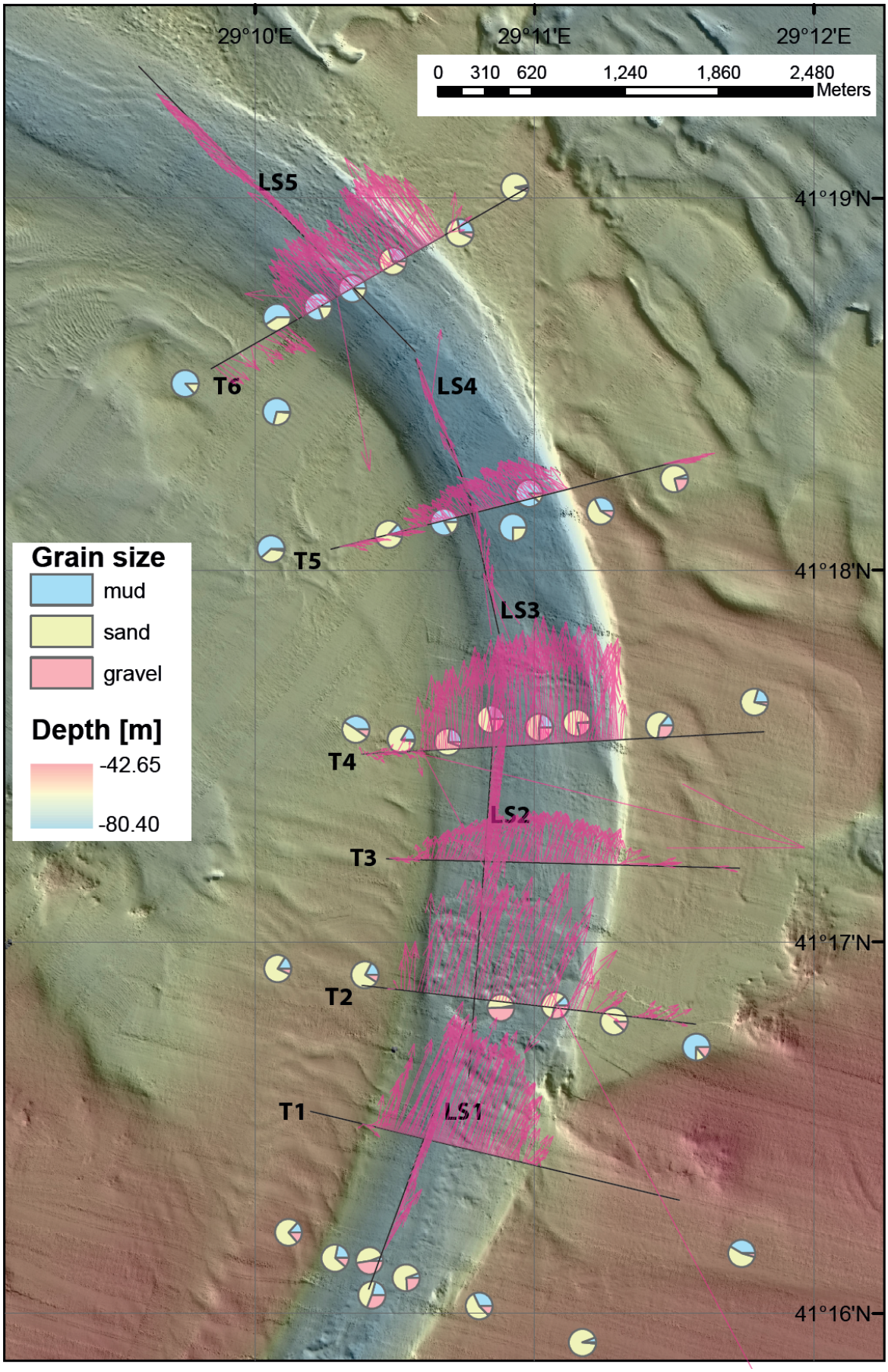
29°10'E
29°11'E
29°12'E
0 310 620 1,240 1,860 2,480
Meters
41°19'N
41°18'N
41°17'N
41°16'N
LS5
LS4
LS3
LS2
LS1
T6
T5
T4
T3
T2
T1
Grain size
mud
sand
gravel
Depth [m]
-42.65
-80.40

Figure 5.12. Basal flow velocities. Basal flow velocity and grain size distribution. Direction shown corresponds to the flow above the noisy velocity ADCP records (~1-2 m above seafloor). Saline current flows from bottom to top of figure.

The decrease in the basal flow velocities between T4 and T5 coincides with a fining of sediment size in the channel seafloor (Figure 5.12). The magnitude of the basal velocity and the size and composition of sediment is similar between cross-stream transects T2 and T4. In contrast, the drop in basal flow velocity between T4 and T5 coincides with an increase in mud content (Figure 5.12). The basal flow accelerates from transect T5 to T6. The outer bend bar in cross-stream transect T6 might reduce the area of the cross-section and accelerate the flow. This velocity increase is accompanied by a coarsening of the sediment in the outer bend of the channel seafloor. However, the mud/sand proportion of the sediment in the inner bend of transects T5 and T6 remains similar (Figure 5.12). The coexistence of different basal flow velocity and bathymetry, and similar sediment composition in transects T5 and T6 suggests that although the nature of the helical flow appears to mostly explain the variable nature of the sediment distribution within the channel there is more complexity than existing models would suggest (Keevil et al., 2006; 2007). Local changes in the bathymetry could generate circulation cells in the near-bed zone that might lower the basal flow velocity. The difference in time-scales between helical flow measurements (two days in this study) and sediment distribution (function of basal helical flows over a long time period) might also support the observation of similar sediment grain sizes in the inner T5 and T6 and different basal velocities.

5.5 Conclusions

The helical structure of submarine flows in meanders contributes to the downstream and cross-stream sediment transport along submarine channel systems. Thus, understanding the helical flow structure is key to understanding submarine channel evolution and sand accumulations. Early studies on helical flows in submarine flows have decomposed the 3D helical flow into 2D slices, which were referenced to either the channel direction or the flow direction. However, recent works show the importance of undertaking 3D analyses of

helical flows because the helical flow structure evolves around the bend. This work shows that the use of different frames of reference, which allow a 2D view of the 3D helical flow, might result in different 2D views of the helical flow. This novel study demonstrates that depending upon the frame of reference 2D flow patterns can appear very different from one another and even show opposite senses of rotation. We suggest that the internal flow structure should be analysed in a frame of reference defined by the flow direction instead of the channel direction. We also show that the nature of the helical flow is crucial for the sediment distribution in meanders, which in conjunction with the channel bathymetry forms a complex sedimentary system.

Chapter 6:

Conclusions

The overall aim of this study was to better understand the dynamics of submarine density flows, and their interaction with the seafloor, by analyzing new direct field measurements. This aim was achieved through: (1) detailed analysis of direct monitoring datasets of turbidity currents in the Congo Canyon, and of a saline underflow at the entrance of the Black Sea; (2) comparison of new observations from the Congo Canyon and the Black Sea with previously suggested models for the internal structure of turbidity currents and saline flows; and, (3) development of new models for turbidity current and saline flow behaviour, with a view to provide a broader understanding of density flows worldwide.

The three specific research questions that this thesis addressed were:

1. Can the sediment type within submarine sediment density flows control the duration of the flows?
2. How do density stratification and flow acceleration processes combine to influence suspend sediment transport in the meanders of long submarine canyon systems?
3. How accurately do different analysis frames of reference of the flow structure of submarine density flows reflect the sediment distribution observed in meandering submarine channel systems?

The following sections aim to answer each of these questions, and to link each thesis chapter to the research question on which the chapter focused.

6.1 Can the sediment type within submarine sediment density flows control the duration of the flows?

Identifying the governing factors of the duration of turbidity currents is crucial to quantify the sediment load that submarine density flows carry to the deep-sea. The main individual turbidity current analysed in chapter 3 lasted for nearly a week with a water discharge equivalent to the Mississippi River. In contrast, previous field measurements of turbidity currents recorded flows that lasted for only hours or minutes. The discharges of the turbidity currents in the Congo Canyon are thought to transport amounts of nutrients and fresh water to the deep-sea that might alter submarine channel ecosystems. Additionally, this thesis suggest that this single submarine channel system contributes ~2% to the global flux of terrestrial organic carbon transported each year into the deep-sea.

Analysis of new direct measurements revealed that turbidity currents in the Congo Canyon may differ from previously measured flows in two main ways:

1. The frontal part of turbidity currents in the Congo Canyon (the frontal cell) is shown to be the fastest and densest part of the flow, unlike almost all previous laboratory observations. This fast and dense frontal cell appears to drive the flows, and was capable of eroding seafloor sediment, thus fueling the flow. The eroded sediment passed to the slower body that followed the frontal cell, and was kept in suspension for almost a week at the measurement site, until it settled out at the tail of the flow.
2. The difference between the fastest part of the flow and the much slower body and tail, led to stretching of the flow along the extensive Congo Canyon submarine channel system. This stretching hypothesis was validated by analysis of flows recorded at two different mooring locations in the channel thalweg.

Thus, chapter 3 showed a novel turbidity current structure, which represents self-sustained turbidity currents that stretch over time. These differences from

previous observations might result from the variation in particle size of the sediment in submarine channel systems. The Congo Canyon is a mud-rich channel system that contrasts with the coarser channel systems where other observations have been collected. Coarser grains would be expected to settle faster than Congo Canyon muddy grains, which may lead to an earlier cessation of flow in coarser settings.

Turbidity currents in the Congo Canyon downstream of the study area of chapter 3 could be even longer than 1-week because of their self-sustaining and stretching nature. Long-duration turbidity currents imply a continuous stress and hazard for infrastructure laid on the seafloor in the path of these turbidity currents. The long duration of these submarine flows in the Congo Canyon are also thought to represent an important contribution of turbidity currents in the burial of terrestrial organic carbon.

6.2 How do density stratification and flow acceleration processes combine to influence suspend sediment transport in the meanders of long submarine canyon systems?

The largest submarine channel systems on Earth share a meandering planform. This coexistence suggests that meanders are important to keep sediment in suspension and thereby sustain long run-out flows within submarine channel systems. Several studies in the last 20 years aimed to understand the structure of submarine density flows at channel meanders, and the link between flow structure and suspended sediment. The conclusions from those studies agreed that submarine density flows have a helical form at meander bends; however, the direction of circulation of the helical flow at the seabed has been an area of much disagreement. It is important to understand whether circulation is towards the inner or outer bend, because this dictates how sediment is suspended and distributed across and down the channel.

The analysis and model presented in chapter 4 reconciled these competing inner- and outer-directed flow hypotheses by analyzing detailed measurements at a meander bend in the deep-water Congo Canyon. Chapter 4 explained that both circulations are possible, and that the direction could be predicted by the

combination of two main competing pressure gradients in the flow. The helical structure of the submarine density flows in meanders mainly depended on the combination of two pressure gradients with opposite directions:

1. Pressure gradient due to the superelevation of the flow in the meander: Flows experimented centrifugal acceleration in the meander. The centrifugal acceleration caused superelevation of the flow towards the outer bend that reaches its maximum at the apex, where the bend curvature is at its highest. The superelevation of the flow represented a disequilibrium that developed a pressure gradient to work towards the return of flow equilibrium. This pressure gradient due to flow superelevation pushed the dense basal flow towards the inner bend, with a direction opposite to the direction imposed by the flow superelevation.
2. Pressure gradient due to density stratification of the flow at the inner bend: The dense basal flow was pushed by the pressure gradient due to superelevation and gathered in the inner bend. This gathering of dense fluid at the inner bend then generated a lateral difference in density, which in turn, caused a lateral pressure gradient that worked to try to balance the flow density laterally. This lateral pressure gradient due to density stratification pushed the basal flow back towards the outer bend.

The ratio between the two pressure gradients resulted in a basal circulation towards either the inner bend or the outer bend. The former occurred when the pressure gradient due to flow superelevation dominated over the lateral pressure gradient due to density stratification. The latter occurred when the lateral pressure due to density stratification dominated over the pressure gradient due to flow superelevation. Both basal circulations (towards the inner and outer bend) could be observed depending on the values of both pressure gradients, i.e. curvature of the submarine channel system and the stratification of the flow. Additionally, chapter 4 highlighted that the superelevation and lateral density stratification of the flow evolved around the bend. This evolution implies that the basal circulation might reverse at the apex of the bend, instead of between bends as previously believed, which is key to predicting the evolution of the submarine channel systems.

6.3 What analysis of the flow structure of submarine density flows respond best to the sediment distribution in meandering submarine channel systems?

This research question follows on from the previous question. The research question in the previous section aimed to connect basal helical circulation in meanders and sediment mobilisation. Chapter 5 analysed the methods used in previous works to evaluate that connection between flow and suspended sediment. It also studied the link between basal helical circulation, sediment mobilisation and submarine channel evolution.

Earlier works in seafloor sediment mobilisation focused their analysis on the basal circulation exclusively in a cross-stream section. Different studies defined the cross-stream section on different frames of reference, mainly either normal to the channel direction or normal to the flow direction. However, chapter 4 highlighted the varying nature around the bend of the pressure gradients that governed the basal circulation of submarine density flows. Consequently, a cross-stream section analysis of the basal flow might be incomplete because the variation of the downstream component around the bend could affect the result. Chapter 5 of this thesis compared the three frames of reference commonly used to study cross-stream basal circulation, and concluded:

1. The cross-stream view of the basal circulation represented a 2-dimensional slice of a 3-dimensional basal helical circulation. This meant that the basal helical circulation that was shown by a cross-stream view was highly sensitive to even a small rotation between frames of reference. Thus, the 3-dimensional basal circulation, which is the same for all frames of references, could have different 2-dimensional representations on different frames of references.
2. Seafloor sediment mobilisation should be analysed through both the cross-stream and downstream study of the helical flow. The cross-stream analysis of the basal circulation (relative to the flow direction) provided information about the flow cross-stream behaviour. However, downstream basal circulation also mobilized the seafloor sediment and needed to be incorporated in the analysis.

3. The basal helical circulation was key to mobilising seafloor sediment, and should be studied to predict submarine channel evolution. However, the local bathymetry of the submarine channel system influenced the basal helical circulation, and as a result, controlled indirectly the seafloor sediment mobilisation and the channel morphology.

The study of submarine channel evolution should involve the study of the 3-dimensional basal flow and the local bathymetry variations. That suggested a further complexity of the system than what current basal circulation models showed.

6.4 Future work

Most of the work in this thesis relied on ADCP measurements. ADCPs have successfully recorded submarine density flows in the field in recent years. Measurements from ADCPs have also allowed estimations of sediment concentrations and velocities in the near-bed zone, under considerations of grain size uniformity and velocity profile shape. The estimation of sediment concentration assumes that the sediment size is constant within the flow. While we know that these are unrealistic assumptions, the methodology chapter defines Kt, a parameter to evaluate the reliability of the sediment grain size assumption. This parameter shows that apart from at the front of the flow, the estimates appear reasonable. However, the acoustic inversion method could be improved by combining ADCP measurements and sediment sampling within the flow.

ADCPs are typically incapable of measuring reliable data in the near-bed zone, whose size is proportional to the elevation of the ADCP over the seafloor. Important flow processes occur in this area, however, which means we may miss the existence of dense near-bed layers, peak velocities or zones of high turbulence from our existing observations. The deployment of specific instrumentation to collect local velocities at fixed heights in the near-bed area could start to fill in these certainty gaps. This would result in the calculation of more accurate velocities than the velocities estimated through extrapolation, which is the current method to obtain velocities in the near-bed area (see chapter 2).

Obtaining accurate velocity measurements in the near-bed area of submarine density flows would also improve the helical flow model presented in chapter 4. The model in this chapter predicts the behaviour of the flow in the near-bed area based on velocity extrapolations over the side lobe interference area. However, the availability of accurate velocity measurements in this area would confirm whether the model holds in this near-bed area. The model proposed in chapter 4 could also be further tested if measurements of velocities and density of turbidity currents could be collected simultaneously in several transects around a submarine channel bend and at several distances from the origin of each transect. The analysis of those velocity and density measurements would confirm the differences in the helical flow behaviour between turbidity currents of different levels of stratification and at different cross-stream section around the bend.

A potential improvement in predicting the helical flow behaviour in the near-bed area of submarine density flows would reduce the uncertainty on the mobilisation of seafloor sediment. Despite that the basal circulation of the helical flow appears to highly influence the direction of mobilisation of the seafloor sediment, local bathymetric variations might also contribute to the mobilisation. Assessing the changes in velocity and density of submarine density flows through inferring local changes in the bathymetry of the submarine channel systems would support the hypothesis of an at least three-way link between flow dynamics, bathymetry and submarine channel evolution.

Bibliography

Abad, J.D., Sequeiros, O.E., Spinewise, B., Pirmez, C., Garcia, M.H. and Parker, G. (2011). Secondary current of saline underflow in a highly meandering channel: experiments and theory. Journal of Sedimentary Research. 81, 787-813.

Allen, J.R.L. (1985). Principles of physical sedimentology. Ed. George Allen & Unwin, London, 272 pp.

Ashmore, P.E., Ferguson, R.I., Prestegaard, K.L., Ashworth, P.J. and Paola, C. (1992). Secondary flow in anabranch confluences of a braided, gravel-bed stream. Earth Surface Processes and Landforms 17, 299-311.

Azpiroz-Zabala, M., Cartigny, M.J.B., Talling, P.J., Parsons, D.R., Sumner, E.J., Clare, M.A., Simmons, S.M., Cooper, C. and Pope, E. (2017a). Newly recognized turbidity current structure can explain prolonged flushing of submarine canyons, Science Advances 3: e1700200.

Azpiroz-Zabala, M., Cartigny, M.J.B., Sumner, E.J., Clare, M.A., Talling, P.J., Parsons, D.R. and Cooper, C. (2017b). A general model for the helical structure of geophysical flows in channel bends. Geophysical Research Letters, 44, 11,932–11,941. https://doi.org/10.1002/2017GL075721.

Babonneau, N. (2002). “Mode de fonctionnement d’un chenal turbiditique méandriforme: Cas du système turbiditique actuel de Zaïre,” thesis, L’universite Bordeaux I. 328 pp.

Bagnold, R.A. (1962). Auto-suspension of transported sediment; turbidity currents. Proceedings of the Royal Society of London A: Mathematical, Physical and Engineering Sciences. 265, 315–319.

Bagnold, R.A. (1977). Bed load transport by natural rivers. Water Resources Research 13 (2), 303-312.

Baas, J.H. and McCaffrey, W.D. (2005). Coupling between suspended sediment distribution and turbulence structure in a laboratory turbidity current. Journal of Geophysical Research 110, C11015, doi:10.1029/2004JC002668.

van den Berg, J.H., van Gelder, A., Mastbergen, D.R. (2002). The importance of breaching as a mechanism of subaqueous slope failure in fine sand. Sedimentology 49, 81–95.

Bolla Pittaluga, M. and Imran, J. (2014). A simple model for vertical profiles of velocity and suspended sediment concentration in straight and curved submarine channels. Journal of Geophysical Research: Earth Surface 119, 483-503, doi: 10.1002/2013JF002812.

Bouma, A.H. (1962). Sedimentology of some flysch deposits. Elsevier, Amsterdam. 168 pp.

Bouma, A.H., Normark, W.R. and Barnes, N.E. (2012). Submarine Fans and Related Turbidite Systems. Springer-Verlag. 351 pp.

Canals, M., Puig, P., de Madron, X.D., Heussner, S., Palanques, A. and Fabres, J. (2006). Flushing submarine canyons. Nature 444, 354–357.

Cantero, M.I., Shringarpure, M. and Balachandar, S. (2012). Towards a universal criteria for turbulence suppression in dilute turbidity currents with non-cohesive sediments. Geophysical Research Letters 39, L14603, doi:10.1029/2012GL052514.

Carter, L., Gavey, R., Talling, P.J. and Liu, J.T. (2014). Insights into submarine geohazards from breaks in subsea telecommunication cables. Oceanography 27, 58–67.

Cartigny, M.J.B., Eggenhuisen, J.T., Hansen, E.W.M. and Postma, G. (2013). Concentration-dependent flow stratification in experimental high-density turbidity currents and their relevance to turbidite facies models. Journal of Sedimentary Research 83, 1046–1064.

Chant, R.J. (2002). Secondary circulation in a region of flow curvature: Relationship with tidal forcing and river discharge. Journal of Geophysical Research 107, C9, 3131, doi:10.1029/2001JC001082.

Clare, M.A., Hughes Clarke, J.E., Talling, P.J., Cartigny, M.J.B. and Pratomo, D.G. (2016). Preconditioning and triggering of offshore slope failures and turbidity currents revealed by most detailed monitoring yet at a fjord-head delta. Earth and Planetary Science Letters 450, 208–220.

Clare, M.A., Vardy, M.E., Cartigny, M.J.B., Talling, P.J., Himsworth, M.D., Dix, J.K., Harris, J.M., Whitehouse, R.J.S. and Belal, M. (2017). Direct monitoring of active geohazards: emerging geophysical tools for deep-water assessments. Near Surface Geophysics, 2017, 15, 427-444

Chikita, K. (1989). A field study on turbidity currents initiated from spring runoffs. Water Resources Research 25 (2), 257-271.

ComCat; https://earthquake.usgs.gov/earthquakes/search/.

Congolobe group, Rabouille, C., Olu, K., Baudin, F., Khripounoff, A., Dennielou, B., Arnaud-Haond, S., Babonneau, N., Bayle, C., Beckler, J., Bessette, S., Bombled, B., Bourgeois, S., Brandily, C., Caprais, J.C., Cathalot, C., Charlier, K., Corvaisier, R., Croguennec, C., Cruaud, P., Decker, C., Droz, L., Gayet, N., Godfroy, A., Hourdez, S., LeBruchec, J., Le Saout, J., Lesaout, M., Lesongeur, F., Martinez, P., Mejanelle, L., Michalopoulos, P., Mouchel, O., Noel, P., Pastor, L., Picot, M., Pignet, P., Pozzato, L., Pruski, A.M., Rabiller, M., Raimonet, M., Ragueneau, O., Reyss, J.L., Rodier, P., Ruesch, B., Ruffine, L., Savignac, F., Senyarich, C., Schnyder, J., Sen, A., Stetten, E., Yi Sun, M., Taillefert, M., Teixeira, S., Tisnerat-Laborde, N., Toffin, L., Tourolle, J., Toussaint, F., Vétion, G., Jouanneau, J.M. and Bez, M. (2017). The Congolobe project, a multidisciplinary study of Congo deep-sea fan lobe complex: Overview of methods, strategies, observations and sampling. Deep Sea Res. II 142, 7–24.

Cooper, C., Wood, J., and Andrieux, O. (2013). Turbidity current measurements in the Congo Canyon. OTC 23992. Offshore Technology Conference, 6-9 May, Houston, Texas. 12 pp.

Cooper, C., Wood, J., Imran, J., Islam, A., Wright, P., Faria, R., Tati, A. and Casey, Z. (2016) Designing for turbidity currents in the Congo Canyon. OTC 26919, Offshore Technology Conference, 2-5 May. 16 pp.

Corney, R.K.T., Peakall, J., Parsons, D.R., Elliot, L., Amos, K.J., Best, J.L., Keevil, G.M. and Ingham, D.B. (2006). The orientation of helical flow in curved channels, Sedimentology 53, 249-257.

Corney, R.K.T., Peakall, J., Parsons, D.R., Elliot, L., Best, J.L , Thomas, R.E., Keevil, G.M., Ingham, D.B. and Amos, K.J. (2008). Reply to Discussion of Imran et al. on ''The orientation of helical flow in curved channels'' by Corney et al., Sedimentology, 53, 249–257. Sedimentology 55, 241-247.

Cossu, R. and Wells, M.G. (2010). Coriolis forces influence the secondary circulation of gravity currents flowing in large-scale sinuous submarine channel systems. Geophysical Research Letters, 37, L17603, doi:10.1029/2010GL044296.

Darby, S.E. and Peakall, J. (2012). Modelling the equilibrium bed topography of submarine meanders that exhibit reversed secondary flows. Geomorphology 163-164, 99-109.

Dee, D.P., Uppala, S.M., Simmons, A.J., Berrisford, P., Poli, P., Kobayashi, S., Andrae, U., Balmaseda, M.A., Balsamo, G., Bauer, P., Bechtold, P., Beljaars, A.C.M., van de Berg, L., Bidlot, J., Bormann, N., Delsol, C., Dragani, R., Fuentes, M., Geer, A.J., Haimberger, L., Healy, S.B., Hersbach, H., Hólm, E.V., Isaksen, L., Kållberg, P., Köhler, M., Matricardi, M., McNally, A.P., Monge-Sanz, B.M., Morcrette, J.J., Park, B.K., Peubey, C., de Rosnay, P., Tavolato, C., Thépaut, J.N. and Vitart, F. (2011). The ERA-Interim reanalysis: Configuration and performance of the data assimilation system. Quarterly Journal of the Royal Meteorological Society 137, 553–597.

Dennielou, B., Droz, L., Babonneau, N., Jacq, C., Bonnel, C., Picot, M., Le Saout, M., Saout, Y., Bez, M., Savoye, B., Olu, K. and Rabouille, C. (2017). Morphology, structure, composition and build-up processes of the active channel-mouth lobe complex of the Congo deep-sea fan with inputs from remotely operated underwater vehicle (ROV) multibeam and video surveys. Deep Sea Research II 142, 25–49.

Dietrich, W.E. and Smith, J.D. (1983). Influence of the Point Bar on Flow Through Curved Channels, Water Resources Research 19 (5), 1173-1192.

Dorrell, R.M., Darby, S.E., Peakall, J., Sumner, E.J., Parsons, D.R. and Wynn, R.B. (2013). Superelevation and overspill control secondary flow dynamics in submarine channels, Journal of Geophysical Research 118, 3895-3915, doi:10.1002/jgrc.20277.

Dorrell, R.M., Peakall, J., Sumner, E.J., Parsons, D.R., Darby, S.E., Wynn, R.B., Özsoy, E. and Tezcan, D. (2016). Flow dynamics and mixing processes in hydraulic jump arrays: Implications for channel-lobe transition zones. Marine Geology 381, 181–193.

Downing, A., Thorne, P.D. and Vincent, C.E. (1995). Backscattering from a suspension in the near field of a piston transducer. Journal of Acoustical Society of America. 97, 1614–1620.

Eggenhuisen, J.T. and Mc Caffrey, W.D. (2012a). Dynamic deviation of fluid pressure from hydrostatic pressure in turbidity currents: Geology 40, 295–298, doi: 10.1130/G32627.1.

Eggenhuisen, J.T. and Mc Caffrey, W.D. (2012b). The vertical turbulence structure of experimental turbidity currents encountering basal obstructions: implications for vertical suspended sediment distribution in non-equilibrium currents. Sedimentology 59, 1101-1120.

Ellison, T.H. and Turner, J.S. (1959). Turbulent entrainment in stratified flows. Journal of Fluid Mechanics 6(3), 423-448. doi: 10.1017/S0022112059000738.

Ezz, H. and Imran, J. (2014). Curvature-induced secondary flow in submarine channels, Environ. Fluid Mech. 14, 343-370.

Flood, R.D., Hiscott, R.N. and Aksu, A.E. (2009). Morphology and evolution of an anastomosed channel network where saline underflow enters the Black Sea. Sedimentology 56, 807–839.

Francois, R.E. and Garrison, G.R. (1982a). Sound absorption based on ocean measurements. Part I: Pure water and magnesium sulphate contributions. Journal of Acoustical Society of America 72, 896–907.

Francois, R.E. and Garrison, G.R. (1982b). Sound absorption based on ocean measurements. Part II: Boric acid contribution and equation for total absorption. Journal of Acoustical Society of America. 72, 1879–1890.

Galy, V., France-Lanord, C., Beyssac, O., Faure, P., Kudrass, H. and Palhol, F. (2007). Efficient organic carbon burial in the Bengal fan sustained by the Himalayan erosional system. Nature 450, 407–410.

Giorgio Serchi, F., Peakall, J., Ingham, D.B. and Burns, A.D. (2011). A unifying computational fluid dynamics investigation on the river-like to river-reversed secondary circulation in submarine channel bends. Journal of Geophysical Research., 116, C06012, doi:10.1029/2010JC006361, 2011.

Heezen, B.C., Menzies, R.J., Schneider, E.D., Ewing, W.M., Granelli, N.C.L. (1964). Congo Submarine Canyon. American Association of Petroleum Geologists Bulletin. 48 (7), 1126-1149.

Huang, H., Imran, J. and Pirmez, C. (2012). The depositional characteristics of turbidity currents in submarine sinuous channels. Marine Geology 329–331, 93–102.

Hughes Clarke, J.E. (2016). First wide-angle view of channelized turbidity currents links migrating cyclic steps to flow characteristics. Nature Communications 7, 11896.

Imran, J., Islam, M.A., Huang, H., Kassem, A., Dickerson, J., Pirmez, C. and Parker, G. (2007). Helical flow couplets in submarine gravity underflows. Geology 35 (7), 659-662.

Imran, J., Islam, M.A., Kassem, A. (2008). ‘‘The orientation of helical flow in curved channels’’ by Corney et al., Sedimentology, Vol. 53, pp. 249–257 – discussion. Sedimentology 55, 235-239.

Inman, D.L., Nordstrom, C.E. and Flick, R.E. (1976). Currents in submarine canyons: an air-sea-land interaction. Annual Review of Fluid Mechanics 8, 275-310.

Islam, M.A. and Imran, J. (2008). Experimental modeling of gravity underflow in a sinuous submerged channel. Journal of Geophysical Research 113, C07041, doi:10.1029/2007JC004292.

Janocko, M., Cartigny, M.B.J., Nemec, W. and Hansen, E.W.M. (2013). Turbidity current hydraulics and sediment deposition in erodible sinuous channels: Laboratory experiments and numerical simulations. Marine and Petroleum Geology 41, 222-249.

Kao, S.J., Dai, M., Selvaraj, K., Zhai, W., Cai, P., Chen, S.N., Yang, J.Y.T., Liu, J.T., Liu, C.C., Syvitski and J.P.M.. (2010). Cyclone driven deep sea injection of freshwater and heat by hyperpycnal flow in the subtropics. Geophysical Research Letters 37, L21702.

Kassem, A. and Imran, J. (2004). Three-dimensional modeling of density current. II. Flow in sinuous confined and unconfined channels, Journal of Hydraulic Research 42 (6), 591-602.

Keevil, G.M., Peakall, J., Best, J.L. and Amos, K.J. (2006). Flow structure in sinuous submarine channels: velocity and turbulence structure of an experimental submarine channel, Marine Geology 229, 241-257.

Keevil, G.M., Peakall, J., Best and J.L (2007). The influence of scale, slope and channel geometry on the flow dynamics of submarine channels. Marine and Petroleum Geology 24, 487–503.

Khripounoff, A., Vangriesheim, A., Babonneau, N., Crassous, P., Dennielou, B. and Savoye, B. (2003) Direct observation of intense turbidity current activity in the Zaire submarine valley at 4000 m water depth. Marine Geology 194, 151-158.

Khripounoff, A., Vangriesheim, A., Crassous and P , Etoubleau, J. (2009). High frequency of sediment gravity flow events in the Var submarine canyon (Mediterranean Sea). Marine Geology 263, 1–6.

Khripounoff, A., Crassous, P., Lo Bue, N., Dennielou, B. and Silva Jacinto, R. (2012). Different types of sediment gravity flows detected in the Var submarine canyon (Mediterranean Sea). Progress in Oceanography 106, 138–153.

Kneller, B.C., Bennett, S.J. and McCaffrey, W.D. (1999). Velocity structure, turbulence and fluid stresses in experimental gravity currents. Journal of Geophysical Research Oceans 104, 5281-5291.

Kneller, B. and Buckee, C. (2000). The structure and fluid mechanics of turbidity currents: A review of some recent studies and their geological significance. Sedimentology 47 (suppl. 1), 62–94.

Komar, P.D. (1977). Computer simulation of turbidity current flow and the study of deep-sea channels and fan sedimentation, in The Sea: Ideas and Observations on Progress in the Study of the Seas, E. D. Goldberg, Ed. (Wiley, 1977), vol. 6, 603–621.

Kuenen, P.H. (1937). Experiments in connection with Daly's hypothesis on the formation of submarine canyons. Leidse Geol. Mededel., 8, 327-335.

Kuenen, P.H. and Migliorini, C.I. (1950). Turbidity Currents as a Cause of Graded Bedding, The Journal of Geology 58, 2, 91-127. doi.org/10.1086/625710

Kuenen, P.H. (1952). Estimated size of the Grand Banks turbidity current. American Journal of Science 250, 874-884.

Lane S.N., Bradbrook, K.F., Richards, K.S., Biron, P.M. and Roy, A.G. (2000) Secondary circulation cells in river channel confluences: measurement artefacts or coherent flow structures? Hydrological Processes 14, 2047-2071.

Lavery, A.C. and Ross, T. (2007). Acoustic scattering from double-diffusive microstructure. Journal of Acoustical Society of America 122 _3_, 1449-1462, 0001-4966/2007/122_3_/1449/14.

Lee, T.H. and Hanes, D.M. (1996). Comparison of field observations of the vertical distribution of suspended sand and its prediction by models. Journal of Geophysical Research Oceans 101, 3561–3572.

de Leeuw, J., Eggenhuisen, J.T. and Cartigny, M.J.B. (2016). Morphodynamics of submarine channel inception revealed by new experimental approach. Nature Communications 7, 10886.

Liu, J.T., Wang, Y.H., Yang, R.J., Hsu, R.T., Kao, S.J., Lin, H.L. and Kuo, F.H. (2012). Cyclone-induced hyperpycnal turbidity currents in a submarine canyon. Journal Geophysical Research. 117, C04033.

Mastbergen, D.R. and van den Berg, J.H. (2003). Breaching in fine sand and the generation of sustained turbidity currents in submarine canyons. Sedimentology 50, 625–637.

McCaffrey, W.D., Choux, C.M., Baas, J.H. and Haughton, P.D.W. (2003). Spatio-temporal evolution of velocity structure, concentration and grain size stratification within experimental particulate gravity currents. Marine Petroleum Geology 20, 851–860.

Meiburg, E. and Kneller, B. (2010). Turbidity currents and their deposits. Annual Review of Fluid Mechanics. 2010. 42:135–56. doi: 10.1146/annurev-fluid-121108-145618.

Middleton, G.V. (1966). Experiments on density and turbidity currents II: Uniform flow of density currents. Canadian Journal of Earth Sciences. 3, 627-637.

Middleton, G.V. (1993). Sediment deposition from turbidity currents. Annual Review of Earth and Planetary Science. 21, 89–114.

Milliman, J.D. and Syvitski, J.P.M. (1992). Geomorphic/tectonic control of sediment discharge to the ocean: The importance of small mountainous rivers. Journal of Geology 100, 525–544.

Moate, B.D. and Thorne, P.D. (2012). Interpreting acoustic backscatter from suspended sediments of different and mixed mineralogical composition. Continental Shelf Research 46, 67–82.

Mulder, T. and Syvitski, J.P.M. (1995). Turbidity currents generated at river mouths during exceptional discharges to the world oceans. . Journal of Geology 103, 285–299.

Mulder, T., Syvitski, J.P.M., Migeon, S., Faugéres, J.C. and Savoye, B. (2003). Marine hyperpycnal flows: Initiation, behaviour, and related deposits. A review. Marine Petroleum Geology 20, 861–882.

Nidzieko, N. J., Hench, J.L. and Monismith, S.G. (2009). Lateral circulation in well-mixed and stratified estuarine flows with curvature, Journal of Physical Oceanography, 39, 831–851, doi:10.1175/2008JPO4017.1.

Nilsen, T.H., Shew, R.D., Steffens, G.S. and Studlick, J.R.J. (2008). Atlas of Deep-Water Outcrops (AAPG and Shell Exploration & Production.

Normark, W.R. (1970). Growth patterns of deep-sea fans. American Association of Petroleum. Geologists Bulletin 54 (11), 2170-2195.

Normark, W.R. and Carlson, P.R. (2003). Giant submarine canyons: Is size any clue to their importance in the rock record? in Chan, M.A., and Archer, A.W., eds., Extreme depositional environments: Mega end members in geologic time: Boulder, Colorado, Geological Society of America Special Paper 370.

Oberg, K. and Mueller, D.S. (2007). Validation of streamflow measurements made with acoustic Doppler current profilers. Journal of Hydraulic Engineering 133, 1421–1432.

Parker, G. (1982). Conditions for the ignition of catastrophically erosive turbidity currents. Marine Geology, 46, 307—327.

Parker, G., Fukushima, Y. and Pantin, H.M. (1986). Self-accelerating turbidity currents. Journal of Fluid Mechanics 171, 145–181.

Parsons, J.D., Bush, J.W.M. and Syvitski, J.P.M. (2001). Hyperpycnal plume formation from riverine outflows with small sediment concentrations. Sedimentology 48, 465–478.

Parsons, D.R., Best,J.L., Lane, S.N., Orfeo, O., Hardy, R.J. and Kostaschuk, R. (2007). Form roughness and the absence of secondary flow in a large confluence–diffluence, Rio Paraná, Argentina. Earth and Surface Processes Landforms 32, 155–162.

Parsons, D.R., Peakall, J., Aksu, A.E., Flood, R.D., Hiscott, R.N., Besiktepe, S. and Mouland, D. (2010). Gravity-driven flow in a submarine channel bend: direct field evidence of helical flow reversal, Geology 38, 1063-1066.

Parsons, D.R., Jackson, P.R., Czuba, J.A., Engel, F.L., Rhoads, B.L., Oberg, K.A., Best, J.L., Mueller, D.S., Johnson, K.K. and Riley, J.D. (2013). Velocity Mapping Toolbox (VMT): a processing and visualization suite for moving-vessel ADCP measurements. Earth Surf. Process. Landforms 38, 1244–1260. doi: 10.1002/esp.3367.

Patterson, M.M. (1974). Oceanographic data from hurricane Camille. Offshore Technology Conference, Houston, TX, 6 to 8 May 1974.

Paull, C.K., Ussler III, W., Greene, H.G., Keaten, R., Mitts, P. and Barry, J. (2002). Caught in the act: The 20 December 2001 gravity flow event in Monterey Canyon. Geo-Marine Letters 22, 227–232.

Paull, C.K., Ussler III, W., Caress, D.W., Lundsten, E., Covault, J.A., Maier, K.L., Xu, J. and Augenstein, S. (2010). Origins of large crescent-shaped bedforms within the axial channel of Monterey Canyon, offshore California. Geosphere 6, 755–774.

Peakall, J., Ashworth, P. and Best, J. (1996). Physical modeling in fluvial geomorphology: principles, applications and unresolved issues. The scientific nature of geomorphology: Proceedings of the 27th Binghamton symposium in geomorphology. Ed. B.L.Rhoads and C.E. Thorn. 34 pp.

Peakall, J., McCaffrey, B. and Kneller, B. (2000). A process model for the evolution, morphology, and architecture of sinuous submarine channels. Journal of Sedimentary Research, 70 (3), 434–448.

Peakall, J. and Sumner, E.J. (2015). Submarine channel flow processes and deposits: A process-product perspective. Geomorphology 244, 95-120.

Pirmez, C. and Imran, J. (2003). Reconstruction of turbidity currents in Amazon Channel, Marine and Petroleum Geology 20, 823-849.

Pope, E.L., Talling, P.J., Carter, L., Clare, M.A. and Hunt, J.E. (2017). Damaging sediment density flows triggered by tropical cyclones. Earth and Planetary Science Letters 458, 161–169.

Rozovskii, I.L., 1957. Flow of Water in Bends of Open Channels. Kiev, Academy of Sciences of the Ukrainian SSR, 233 pp.

Savoye, B., Babonneau, N., Dennielou, B. and Bez, M. (2009). Geological overview of the Angola-Congo margin, the Congo deep-sea fan and its submarine valleys, Deep-Sea Research II 56, 2169-2182.

Schlünz, B. and Schneider, R.R. (2000). Transport of terrestrial organic carbon to the oceans by rivers: Re-estimating flux- and burial rates. International Journal of Earth Sciences 88, 599–606 .

Sequeiros, O.E., Naruse, H., Endo, N., Garcia, M.H. and Parker, G. (2009). Experimental study on self-accelerating turbidity currents. Journal of Geophysical Research 114, C05025.

Shepard, F.P. (1933) Submarine valleys. American Geographical Society 23 (1), 77-89.

Simpson, J.E. (1997). Gravity currents in the environment and the laboratory. Cambridge University Press, 244 pp.

Smith, C.E. (2013). “Chevron advance Cabinda-ALNG pipeline,” Oil and Gas Journal, 15 January 2013; http://ogj.com/articles/2013/01/chevron-advances-cabinda-alng-pipeline.html.

Stacey, M.W. and Bowen, A.J. (1988). The vertical structure of density and turbidity currents' theory and observations. Journal of Geophysical Research 93 (C4), 3528-3542.

Stetten, E., Baudin, F., Reyss, J.H., Martinez, P., Charlier, K., Schnyder, J., Rabouille, C., Dennielou, B., Coston-Guarini, J. and Pruski, A.M. (2015). Organic matter characterization and distribution in sediments of the terminal lobes of the Congo deep-sea fan: Evidence for the direct influence of the Congo River. Marine Geology 369, 182–195.

Straub, K.M., Mohrig, D., McElroy, B. and Buttles, J. (2008). Interactions between turbidity currents and topography in aggrading sinous submarine channles: A laboratory study, Geological Society of America Bulletin 120, 3/4, 368-385. doi: 10.1130/B25983.1.

Sumner, E.J., Talling, P.J., Lawrence A., Wynn, R.B., Stevenson, C.J. and Frenz, M. (2012). Facies architecture of individual basin-plain turbidites: Comparison with existing models and implications for flow processes. Sedimentology, 59 (6), 1850-1887. doi:10.1111/j.1365-3091.2012.01329.x

Sumner, E.J., Peakall, j., Parsons, D.R., Wynn, R.B., Darby, S.E., Dorrell, R.M., McPhail, S.D., Perrett, J., Webb, A. and White, D. (2013). First direct measurements of hydraulic jumps in an active submarine density current. Geophysical Research Letters, 5904–5908, doi:10.1002/2013GL057862.

Sumner, E.J. and Paull, C.K. (2014). Swept away by a turbidity current in Mendocino submarine canyon, California. Geophysical Research Letters, 41, doi:10.1002/2014GL061863.

Sumner, E.J., Peakall, J., Dorrell, R.M., Parsons, D.R., Darby, S.E., Wynn, R.B., McPhail, S.D., Perrett, J., Webb, A. and White, D. (2014). Driven around the bend: Spatial evolution and controls on the orientation of helical bend flow in a natural submarine gravity current, Journal of Geophysical Research Oceans 119, 898-913, doi:10.1002/2013JC009008.

Szupiany, R.N., Amsler, M.L., Best, J.L. and Parsons, D.R. (2007). Comparison of Fixed- and Moving-Vessel Flow Measurements with an aDp in a Large River. Journal of Hydraulical Engineering, 133(12): 1299-1309. doi: 10.1061/_ASCE_0733-9429_2007_133:12_1299_

Teledyne (2010). ADCP coordinate transformation. P/N 951- -6079-00, 36 pp.

Teledyne (2011). Acoustic Doppler Current Profiler. Principles of Operation: A Practical Primer. P/N 951-6069-00, 62 pp.

Talling, P.J., Wynn, R.B., Masson, D.G., Frenz, M., Cronin, B.T., Schiebel, R., Akhmetzhanov, A.M., Dallmeier-Tiessen, S., Benetti, S., Weaver, P.P.E., Georgiopoulou, A., Zühlsdorff, C. and Amy, L.A. (2007). Onset of submarine debris flow deposition far from original giant landslide. Nature 450, 541-544.

Talling, P.J., Masson, D.G., Sumner, E.J, and Malgesini, G. (2012). Subaqueous sediment density flows: Depositional processes and deposit types. Sedimentology 59, 1937–2003.

Talling, P.J., Paull, C.K., Piper, D.J.W. (2013). How subaqueous sediment density flows triggered, what is their internal structure and how does it evolve? Direct observations from monitoring of active flows. Earth-Science Review 125, 244–287.

Talling, P.J., Allin, J., Armitage, D.A., Arnott,R.W.C., Cartigny, M.J.B., Clare, M.A., Felletti, F., Covault, J.A., Girardclos, S., Hansen, E., Hill, P.R., Hiscott, R.N., Hogg, A.J., Hughes Clarke, J., Jobe, Z.R., Malgesini, G.E., Mozzato, A., Naruse, H., Parkinson, S., Peel, F.J., Piper, D.J.W., Pope, E., Postma, G., Rowley, P., Sguzzini, A., Stevenson, C.J., Sumner, E.J., Sylvester, Z., Watts, C. and Xu, J. (2015). Key future directions for research on turbidity currents and their deposits. Journal of Sedimentary Research 85, 153–169. doi: http://dx.doi.org/10.2110/jsr.2015.03.

Thorne, C.R., Zevenbergen, L.W., Pitlick, J.C., Rais, S., Bradley, J.B. and Julien, P.Y. (1985). Direct measurement of secondary currents in a meandering sand-bed river. Nature, 316, 746–747.

Thorne, P.D., Holdaway, G.P. and Hardcastle, P.J. (1995). Constraining acoustic backscatter estimates of suspended sediment concentration profiles using the bed echo. Journal of Acoustical Society of America 98, 2280–2288.

Thorne, D.P. and Hanes, D.M. (2002). A review of acoustic measurement of small-scale sediment processes. Continental Shelf Research 22, 603–632.

Thorne, P.D. and Hurther, D. (2014). An overview on the use of backscattered sound for measuring suspended particle size and concentration profiles in non-cohesive inorganic sediment transport studies. Continental Shelf Research 73, 97–118.

Transportation Research Board (2004). Methodology for predicting channel migration. Submitted by Lagasse, P.F., Zevenbergen, L.W., Spitz, W.J., Thorne, C.R. Ayres Associates, Inc., Fort Collins, Colorado, 215 pp.

Umlauf, L. and Arneborg, L. (2009). Dynamics of Rotating Shallow Gravity Currents Passing through a Channel. Part I: Observation of Transverse Structure. Journal of Physical Oceanography 39, 2385-2401.

UNESCO (1983), Algorithms for computation of fundamental properties of seawater, UNESCO Technical Paper in Marine Science 44,, UNESCO Division Marine Science, Paris, 53 pp.

Urick, R.J. (1948). The absorption of sound in suspensions of irregular particles. Journal of Acoustical Society of America 20, 283–289.

Vangriesheim, A., Khripounoff, A. and Crassous, P. (2009). Turbidity events observed in situ along the Congo submarine channel. Deep-Sea Research II 56, 2208–2222.

Wei, T., Peakall, J., Parsons, D.R., Chen, Z. Zhao, B. and Best, J. (2013). Three-dimensional gravity-current flow within a subaqueous bend: Spatial evolution and force balance variations. Sedimentology 60, 1668–1680.

Xu, J.P., Noble, M.A., Rosenfeld and L.K. (2004). In-situ measurements of velocity structure within turbidity currents. Geophysical Research Letters 31, L09311.

Xu, J.P., Swatzenski, P.W., Noble, M. and Li, A.C. (2010). Event-driven sediment flux in Hueneme and Mugu submarine canyons, southern California. Marine Geology 269, 74–88.

Xu, J.P., Barry, J.P. and Paull, C.K. (2013). Small-scale turbidity currents in a big submarine canyon. Geology 41 (2), 143–146.

Yu, G. and Tan, S.K. (2006). Errors in the bed shear stress as estimated from vertical velocity profile. Journal of Irrigation and Drainage Engineering 132, 490–497.